2016

Development of an Unmanned Aerial Vehicle for Atmospheric Turbulence Measurement

Brandon M. Witte
University of Kentucky, bmwitt2@gmail.com
Digital Object Identifier: https://doi.org/10.13023/ETD.2016.404

STUDENT AGREEMENT:

I represent that my thesis or dissertation and abstract are my original work. Proper attribution has been given to all outside sources. I understand that I am solely responsible for obtaining any needed copyright permissions. I have obtained needed written permission statement(s) from the owner(s) of each third-party copyrighted matter to be included in my work, allowing electronic distribution (if such use is not permitted by the fair use doctrine) which will be submitted to UKnowledge as Additional File.

I hereby grant to The University of Kentucky and its agents the irrevocable, non-exclusive, and royalty-free license to archive and make accessible my work in whole or in part in all forms of media, now or hereafter known. I agree that the document mentioned above may be made available immediately for worldwide access unless an embargo applies.

I retain all other ownership rights to the copyright of my work. I also retain the right to use in future works (such as articles or books) all or part of my work. I understand that I am free to register the copyright to my work.

REVIEW, APPROVAL AND ACCEPTANCE

The document mentioned above has been reviewed and accepted by the student's advisor, on behalf of the advisory committee, and by the Director of Graduate Studies (DGS), on behalf of the program; we verify that this is the final, approved version of the student's thesis including all changes required by the advisory committee. The undersigned agree to abide by the statements above.

Brandon M. Witte, Student

Dr. Sean C. C. Bailey, Major Professor

Dr. Haluk Karaca, Director of Graduate Studies

Development of an Unmanned Aerial Vehicle for Atmospheric Turbulence Measurement

---

THESIS

A thesis submitted in partial fulfillment of the requirements for the degree of Master of Science in Mechanical Engineering in the College of Engineering at the University of Kentucky

by

Brandon M. Witte

University of Kentucky

Director: Dr. Sean C. C. Bailey, Associate Professor of Mechanical Engineering

Lexington, Kentucky

2016

ABSTRACT OF THESIS

Development of an Unmanned Aerial Vehicle
for Atmospheric Turbulence Measurement

An unmanned aerial vehicle was developed to study turbulence in the atmospheric boundary layer. The development of the aircraft, BLUECAT5, and instrumentation package culminated in a series of flight experiments conducted in two different locations near Stillwater, Oklahoma, USA. The flight experiments employed the use of two of the unmanned aerial vehicles flying simultaneously, each containing a five-hole pressure probe as part of a turbulence-measuring instrumentation package. A total of 18 flights were completed with the objective to measure atmospheric properties at five altitudes between 20 and 120 meters. Multiple flights were flown over two days in which the effects of the diurnal cycle on the boundary layer were investigated. Profiles for mean wind velocity, temperature, and humidity all follow expected boundary layer behavior throughout the day. Evolution of the boundary layer can be seen with the early morning, stable boundary layer identified and its transition to the early mid-day convective mixed boundary layer observed. The corresponding increase in turbulence intensity was found to be significant. The success of the test campaign demonstrated the ability of the developed unmanned system to measure turbulence in the atmospheric boundary layer.

KEYWORDS: Atmospheric boundary layer, Turbulence, Unmanned Aerial Vehicle,
Five-hole probe, Hot-wire anemometry

Brandon M. Witte
October 20, 2016

Development of an Unmanned Aerial Vehicle for Atmospheric Turbulence Measurement

by

Brandon M. Witte

Dr. Sean C. C. Bailey

Director of Thesis

Dr. Haluk Karaca,

Director of Graduate Studies

October 20, 2016

Acknowledgments

I would like to thank my advisor, Dr. Bailey, for the continuous support and guidance he has given me over the past few years. He has provided me with countless opportunities and spent a tremendous amount of time and effort helping me become the student and researcher I am today. It has been a pleasure working with him.

I would also like to thank my parents, who have provided enormous support towards me and my dreams throughout my life. They have been a huge inspiration during this journey and I cannot thank them enough for everything they've done for me.

I am grateful for everyone I have worked with over the past 3 years. To everyone that is currently working in the UAV lab Ryan Nolin, Caleb Canter, Rob Singler, Jonathan Hamilton, and Colby Borchetta you all have been a tremendous help and it's been great working with you. In addition I'd like to specifically thank Cornelia Schlagenhauf for the tremendous amount of help in the five-hole probe development in instrumentation. Her work was essential to the progress of this work.

I would like to extend my gratitude to Mike Thamann for his guidance and willingness to teach me as I began my research as a grad student. His knowledge and expertise was vital to the development of my know-how and skills within the UAV lab.

Lastly, I would like to acknowledge the National Science Foundation who financially supported my work through grant #CBET-1351411 and award #1539070, Collaboration Leading Operational UAS Development for Meteorology and Atmospheric Physics (CLOUDMAP).

Table of Contents

List of Figures

List of Tables

Nomenclature

$[.]_A$	Denotes aerodynamic frame of reference
$[.]_B$	Denotes body fixed frame of reference
$[.]_I$	Denotes inertial frame of reference
α	Angle of attack
β	Angle of sideslip
η	Kolmogrov length scale
μ	Dynamic Viscosity
Ω_{UAV}	Angular velocity of UAV
$\overline{\zeta}$	Time averaged fluid property
ϕ	Angle of wind with respect to North
ρ	Density
τ_K	Kolmogrov time scale
τ_w	Shear stress
Θ	Potential temperature
ζ'	Time-varying fluctuations of fluid property
$\zeta(t)$	Arbitrary time-dependent fluid property

C_α Calibration coefficient for angle of attack

C_β Calibration coefficient for angle of sideslip

C_q Calibration coefficient for dynamic pressure

D Normalization factor for transformation

K Von Karmen Constant

k Turbulent kinetic energy

k^* Modified turbulent kinetic energy

$L_{i,j}$ Coordinate transformation matrix where i,j denote frame of reference

P Total pressure

p Local atmospheric pressure

p_0 Standard atmospheric pressure

P_{dyn} Dynamic pressure

r_{s-CG} Vector pointing from center of gravity to measurement volume on UAV

r_{UAV} Translational position of UAV

Re Reynolds Number

RH Relative humidity

T Temperature

t_i Time corresponding to each discrete sample of five-hole probe velocity

U Mean velocity

u x/East-West directional velocity $u = W_1$

u_τ	Shear velocity
u_i	ith component of the velocity vector
U_r	Relative velocity
U_S	Velocity of sensing volume
U_{UAV}	Velocity of UAV
v	y/North-South directional velocity $v = W_2$
V_i	Voltage corresponding to component u_i
v_K	Kolmogrov velocity scale
W	Wind velocity
w	z/up-down directional velocity $w = W_3$
x_i	ith component of the position vector
ABL	Atmospheric boundary layer
L	Length scale
TAS	True arispeed
UAV	Unmanned aerial vehicle

Chapter 1 Introduction

Boundary layers are among the most frequently studied phenomena in fluid dynamics partly due to the interesting and challenging physics which occur when viscous and inertial forces compete within a fluid moving over a solid body. Boundary layers are also observed in many practical scenarios such as the flow within pipes, oceanic currents, airflow over an aircraft's wings, etc. Thus the study of boundary layers has led to significant contributions to our understanding of fluid dynamics and continues to be an essential component in the investigation of the "mystery" that is turbulent flow. One of the most prevalent and increasingly important boundary layers existent on earth is the atmospheric boundary layer, which has risen in importance due to the growing challenges presented by global climate change and its role in global climate dynamics.

A key scaling parameter in fluid dynamics is the Reynolds number, which describes the ratio of inertial forces to viscous forces or, equivalently, the ratio of the largest scales of turbulence to the smallest scales. The atmospheric boundary layer experiences some of the largest Reynolds number flows encountered on earth. Stull defines the atmospheric boundary layer as "the boundary layer that is part of the troposphere that is directly influenced by the presence of the earth's surface, and responds to surface forcings with a timescale of about an hour or less" [2]. The atmospheric boundary layer is the lowest section of earth's troposphere ranging from the surface of the earth to anywhere between 100 m to 3,000 m high. It is responsible for weather formation, fog formation, heat transfer to the upper atmosphere, and pol-

lution trapping. The earth's surface, being the underlying boundary to the lower atmosphere, introduces many forces through friction drag, heat transfer, and evaporation, all which create instabilities in the flow. The result of these forces provides us with the highly turbulent atmospheric boundary layer acting as a momentum sink as well as a heat source and buffer between the earth's surface and the free atmosphere above. Turbulence is a crucial component of the atmospheric boundary layer due to its role in the transport of mass, momentum, and heat between the earth's surface and the atmosphere. Turbulence is also heavily dissipative in that it converts kinetic energy into internal energy through viscous shear and introduces a broad range of scales in length and time, chaotically contributing to the complexity of the flow [3]. It is the complexity found in the highly turbulent atmospheric boundary layer that limits our understanding of its transporting processes. "The complexity of turbulence is evidenced by the fact that after more than a century of concerted research effort, many of its seemingly simple questions remain unanswered" [4]. The complexity of the flow in the atmospheric boundary layer can be further expanded when obstacles such as terrain, houses or foliage introduce additional wakes within the boundary causing additional momentum losses.

Modern studies of turbulence typically take place in a laboratory and are conducted either experimentally or computationally through numerical simulations. Experimental evaluation of turbulence commonly utilizes wind or water tunnels to set boundary conditions within a controlled environment. Experimental investigation in a laboratory typically produces relatively small Reynolds number turbulence as a result of limitations in achievable size, fluid type, and velocity imposed by the facilities used. However, within these studies there are many ways to interrogate the flow in question such as fixed point sensors or optical techniques. Computational fluid dynamics has become increasingly popular for the study of turbulence as the computational power of computers increases. Direct numerical simulation is the most accurate, solving the

governing equations without modeling. However direct numerical simulation requires immense computational resources to simulate high Reynolds numbers as all length and time scales must be resolved within the simulation, and the Reynolds numbers contained within the atmospheric boundary layer are still out of reach. Thus, turbulence models are introduced to reduce the computational costs. These are typically employed in the form of closure models for the Reynolds-Averaged Navier-Stokes equations, or subgrid-scale models within large eddy simulation. Simulations have greatly contributed to the understanding of turbulence and the coherent structures within them, but models are beginning to be pushed to their respective limits.

As noted, the high Reynolds numbers that characterize the atmospheric boundary layer have proven problematic to replicate in a laboratory. In an attempt to mitigate this issue, researches have utilized several techniques to record turbulence data directly in the atmospheric boundary layer. These techniques include tower, balloon, and manned-aircraft mounted sensors. However, it is evident that these techniques have disadvantages including large time and monetary costs and limited modularity of these systems. The experimental challenges associated with measuring in the atmosphere are compounded by the unpredictability of the flow in both magnitude and direction, issues related to thermal stability of the flow, and the isolated measurements offered by of the tower and balloon approaches [5]. Since these fixed acquisition systems record data at a point over a long period of time, providing strictly temporal information, there is a necessity to assume that the flow structure does not evolve as it advects past the sensors.

Taylor's hypothesis suggested by G.I. Taylor in 1938, states that turbulence can be considered as "frozen" as it advects past a sensor. In other words, any arbitrary property of the turbulent fluid is independent of time as it transverses through space. This simplification should only be considered when an eddy's evolution time is less than the time it takes for the eddy to traverse past the acquisition probe [2]. For

small scales of turbulence this hypothesis has been proven to work fairly well but is subject to error when considered for larger scales. Thus, the usage of the Taylor's hypothesis in the highly turbulent atmospheric boundary layer is a cause for concern and the impact of its application needs to be further examined.

The work in this thesis is concerned with developing a new approach to study turbulence in the atmospheric boundary layer which has the potential to alleviate many of the shortcomings of existing measurement techniques. This approach will utilize unmanned aerial vehicles (UAVs) as they provide a platform that can acquire significant atmospheric data anywhere within the lower surface layer, overcoming restrictions created by tower-based point measurements and high flying, expensive manned aircraft. The idea of using unmanned aerial vehicles as a research platform in the atmospheric boundary layer is still in its infancy but has limitless potential, as commercially available systems for autonomous flight are becoming increasingly reliable. The development of this approach has been a continually evolving process, producing a fully operational system that was tested and flown during the 28th and 29th of June, 2016 in Stillwater Oklahoma as part of a large-scale measurement campaign.

Chapter 2 Background

2.1 Turbulence Theory

The study of turbulence can be traced back to the 1500's and Leonardo da Vinci, with the most commonly cited example, his sketches of turbulent eddies swirling within a pool of water. However, progress in the understanding of turbulent behavior was limited until the late 19^{th} century when Osborne Reynolds started his pipe flow experiments. It was in these experiments that Reynolds discovered that the flow within a pipe became irregular, or turbulent, when a dimensionless ratio created by the combination of diameter, average velocity within pipe, fluid density, and fluid viscosity exceeded a critical value [6]. This ratio is now known as the Reynolds number

$$Re = \frac{\rho U L}{\mu} \tag{2.1}$$

and can be generalized to different types of flow using the fluid's density and dynamic viscosity ρ and μ respectively, and appropriate selection of the flow's characteristic velocity and length scales U and L.

More importantly, realizing that turbulence is far too complicated to reach a detailed understanding of the phenomenon, Reynolds developed a statistical approach to study turbulence in which the flow variables were separated into mean and fluctuating components

$$\zeta(t) = \overline{\zeta} + \zeta'(t) \tag{2.2}$$

where $\zeta(t)$ represents an arbitrary time-dependent fluid property decomposed into

time-averaged, $\overline{\zeta}$ and fluctuation $\zeta'(t)$ components. In this thesis, the overline will be used to indicate a time-averaged quantity. This decomposition led to the derivation of the incompressible Reynolds-Averaged Navier-Stokes (RANS) equation

$$\rho\left[\frac{\partial\overline{u_i}}{\partial t}+\overline{u_j}\frac{\partial\overline{u_i}}{\partial x_j}\right]=-\frac{\partial\bar{p}}{\partial x_i}+\frac{\partial}{\partial x_j}\left[\mu\frac{\partial\overline{u_i}}{\partial x_j}-\rho\,\overline{u_i'u_j'}\right], \tag{2.3}$$

where tensor notation is used and u_i is the ith component of the velocity vector and x_i is the ith component of the position vector in an inertial frame of reference. This equation is essentially identical to the incompressible Navier-Stokes equation for fluid flow, except that the averaging process has introduced the Reynolds stress tensor, $\rho\,\overline{u_i'u_j'}$. The Reynolds stress is introduced by decomposition and averaging of the nonlinear acceleration terms, but is traditionally treated as a stress as it can be thought of as the component of the total stress tensor stemming from momentum transfer from the fluctuating velocity field to the mean velocity field [1]. As a result, the right side of equation 2.3 can be viewed as the sum of three stresses: the isotropic or pressure stress, the viscous stress, and the Reynolds stress [1].

Following Reynolds groundwork on the statistical approach to turbulence, it was Ludwig Prandtl who took the next steps in the verification and development of this method. Prandtl's most successful theory of turbulence was the mixing-length theory based on the concept of the mean free path in thermodynamics which states that before a fluid parcel mixes with the surrounding fluid, it's properties remain constant along a characteristic length. The model was an attempt to describe momentum transfer within turbulent flow of a boundary layer by the means of eddy viscosity. This allowed him to surmise that near the solid wall of a turbulent flow, the average velocity profile is logarithmic. This important discovery in turbulent behavior was expanded upon by Von Kármán in 1930 when he first published his new law of the wall, also known as the 'log law'. This law states that for constant property turbulent

flow at a certain point, the mean velocity U near a smooth, flat surface is proportional to the logarithm of the distance from the wall to that point [7]. This can be written for a coordinate system with it's origin on the surface, x_1 parallel to the surface and x_2 directed away from the surface as

$$\overline{u_1}^+ = \frac{1}{K} \ln x_2^+ + B, \tag{2.4}$$

$$x_2^+ = \frac{x_2 u_\tau}{\nu}, \tag{2.5}$$

$$\overline{u}_1^+ = \frac{\overline{u}_1}{u_\tau}, \tag{2.6}$$

$$u_\tau = \sqrt{\frac{\tau_w}{\rho}}. \tag{2.7}$$

Here B and K are constants, with K known as the von Kármán constant, and τ_w is the shear stress imposed by the fluid at the surface (i.e. skin friction). The log law, while very beneficial to modeling turbulent flow, is valid only in regions of the flow close to the wall and only at sufficiently high Reynolds number [7].

The next significant steps in turbulence analysis were taken by the British physicist G.I Taylor in the 1930's. Taylor introduced much of the formal statistical analysis approaches used today, such as the concept of the turbulence spectrum [8] and the concept of homogeneous and isotropic turbulence, which simplifies analytical approaches to turbulence. An illustration of how the turbulence spectrum changes with respect to various Reynolds numbers can be shown in figure 2.1.

Even though real turbulence is, in fact, generally not isotropic his mathematical techniques have proven valuable in the description of small scale turbulence where the flow is exceptionally close to isotropic conditions. Another contribution of Taylor's which has been used extensively in experiments was his 'frozen flow' hypothesis which is frequently applied to convert temporal information into spatial information. Taylor

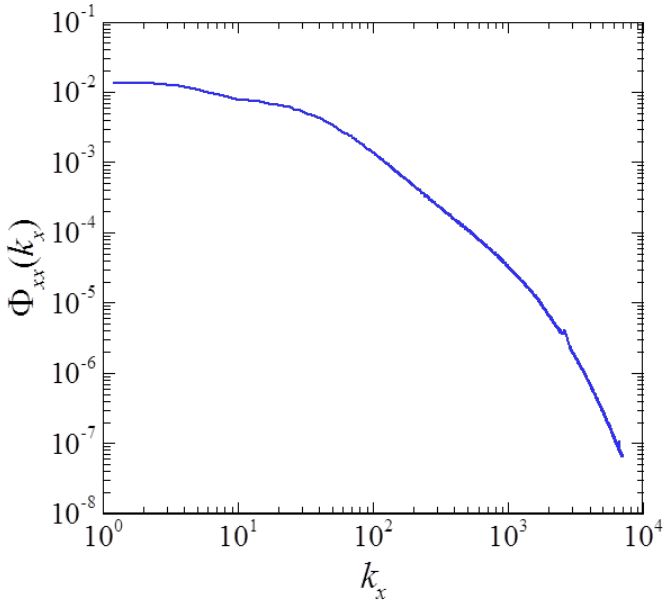

Figure 2.1: Illustration of two dimensional turbulence kinetic energy spectra at various Reynolds numbers, courtesy of Dr. Sean C. Bailey.

explained the simplification in his 1938 paper that "if the velocity of the air stream which carries the eddies is very much greater than the turbulence velocity, one may assume that the sequence of changes in u at a fixed point are simply due to the passage of an unchanging pattern of turbulent motion over the point" [8]. From this assumption, a time-dependent property of the flow can be converted into spatially-dependent property [9] following

$$\zeta(x_i) \approx \zeta(U_i^* t), \tag{2.8}$$

where U_i^* is a suitably selected advection velocity, typically $\overline{u}_i$. This hypothesis is particularly valuable, and often necessary, to relate experimental results (typically taken using a fixed sensor measuring a time-dependent property) to analytical descriptions (typically spatially dependent).

Lewis Richardson a British meteorologist, conducted research within the atmosphere with the overall goal of weather prediction. He was among the first to propose

that turbulence consisted of different sizes of eddies, where the sizes defined characteristic length scales of these eddies. He suggested that the turbulent kinetic energy, quantified as

$$k = \frac{1}{2}\overline{u_i' u_i'}, \tag{2.9}$$

is transferred from the large unstable eddies to the smaller eddies, which in turn break down into even smaller eddies until the remaining energy in the flow is dissipated into internal energy through viscous dissipation [6]. As the Reynolds number increases, the number of transformations between large to small eddies becomes sufficiently large and the movement of the smaller eddies cannot be ignored from the macroscopic structure of the flow [3]. This idea is referred to as the spectral energy cascade and can be identified in figure 2.1. The eddy size is inversely related to the wavenumber, $\kappa = 2\pi/\lambda$, where λ is the wavelength of the turbulent eddy. Therefore, typically as the eddy size decreases, or wavenumber increases, its kinetic energy decreases.

The energy cascade concept was later formalized in the 1940's by A. M. Kolmogorov, a Russian statistician very well respected in the 20^{th} century. His work yielded some of the most important results in turbulence theory. His first hypothesis states "At sufficiently large Reynolds numbers, the statistical properties of the relative velocity in a sufficiently small space-time region depend only on the turbulent kinetic energy dissipation rate per unit mass, ϵ, and the kinematic viscosity, ν [3]. This allowed him to derive on dimensional grounds the smallest scales that contain turbulent kinetic energy. These are the Kolmogorov length, velocity and time scales, respectively

$$\eta = \left(\frac{\nu^3}{\epsilon}\right)^{\frac{1}{4}}, \tag{2.10}$$

$$v_K = (\nu\epsilon)^{\frac{1}{4}}, \tag{2.11}$$

$$\tau_K = \left(\frac{\nu}{\epsilon}\right)^{\frac{1}{4}}. \tag{2.12}$$

His second hypothesis was that at scales much larger than η (which dissipate energy) and much smaller than the largest scales (at which kinetic energy is produced), the kinetic energy transfer between scales must be only dependent on ϵ. From this idea Kolmogorov and Obukhov derived that the turbulent kinetic energy within this subrange must be proportional to

$$k(\kappa) \propto \epsilon^{\frac{2}{3}} \kappa^{-\frac{5}{3}} \tag{2.13}$$

in what is known as the five-thirds law [6].

Numerous contributions to the study of turbulence from the 1940's through recent decades have provided much progress in the understanding and theory, as well as the analysis and calculations of this chaotic and random phenomenon. In recent years much attention has been directed toward computational methods of analyzing turbulent flow. With the ever growing power of digital computers, calculating the relevant properties of turbulent flows becomes more and more attainable. Some popular computational approaches include: modeling the Reynolds stress tensor to close the Reynolds-averaged Navier-Stokes (RANS) equations; direct numerical simulation (DNS) in which the Navier-Stokes equation is fully resolved in time and space; and large-eddy simulation (LES) in which the energy containing eddies are resolved, and the small-scale turbulence is modeled.

2.2 Boundary Layers

In 1904 Ludwig Prandtl introduced the revolutionary concept of the boundary layer within a fluid over a flat surface. His proposal hypothesized that friction caused fluid flow immediately adjacent to the wall to stick to the surface and that these frictional effects were only present in a small region near the wall which he described as the boundary layer [10]. This concept is still among the most important and frequently

experienced fluid dynamic properties and has been the root of considerable research throughout the past century.

Boundary layers can be described as either laminar or turbulent with the characterization generally driven by the Reynolds number of the flow, where the characteristic length and velocity scales in equation 2.1 are the distance downstream and the velocity just outside the boundary layer (the 'free-stream' velocity). As Re rises the inertial forces become more and more dominant, eventually transitioning the flow from a laminar to a turbulent boundary layer.

According to Smits and Marusic the transition to turbulence in a boundary layer can take place with a corresponding Reynolds number on the order of 10^4 depending on the surface roughness and amount of turbulence experienced upstream [4]. It is within this transition region that fluctuations and turbulent eddies begin to appear, causing time variances of the fluid's properties to become increasingly significant. These time dependencies arise from the complex, random, and irregular attributes present within turbulent flow, effectively mixing the fluid's properties in all directions. Although this region experiences considerable mixing of fluid particles, there is very little net transfer of mass across the top of the boundary layer [11]. It should be noted that an exact solution has been found for the velocity and pressure components of a 2-dimensional laminar boundary layer by solving the steady state Navier-Stokes equations in what is known as the Balsius boundary layer. However, this is not the case for turbulent boundary layers and, despite the success of the log-law (equation 2.4), the study of turbulent boundary layers is still an active area of research, particularly with respect to the effect of Reynolds number on the properties of turbulence. In no small part, the challenges of studying turbulent boundary layers are caused by the range of scales involved. Near the surface, the turbulence scales with u_τ and ν (inner scaling), whereas far from the surface the turbulence scales with the free-stream velocity and the thickness of the boundary layer (outer scaling). At low Reynolds numbers, there is

insufficient separation between these scales to separate inner- and outer-scaled effects.

However, the atmospheric boundary layer (ABL) can experience Reynolds numbers on the order of 10^8 and is consequently almost always turbulent with a very wide range of scales. "The [ABL] also differs from its laboratory counterpart in the significance of the Coriolis effect and in it variable and non-neutral bouyancy" [5]. The earth's rotation does not greatly affect the atmospheric surface layer, defined as the bottom 10% of the ABL where turbulent stresses vary by less than 10% of their magnitude [2]. However, the variable, non-neutral buoyancy produced by the heating and cooling of the earth's surface during the the diurnal cycle causes variances in the structure of the ABL as shown in figure 2.2.

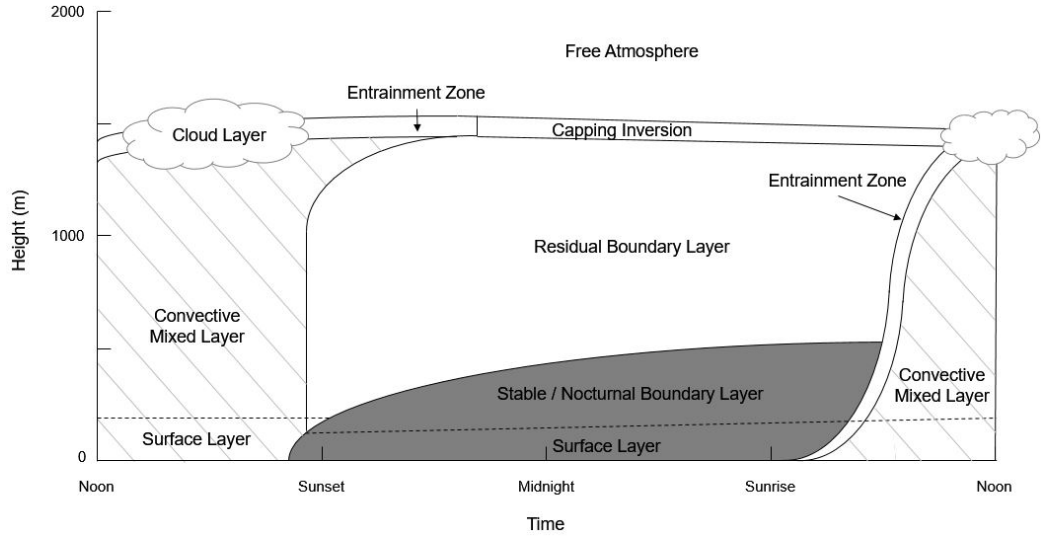

Figure 2.2: Atmospheric boundary layer structure evolution through the diurnal cycle.

During daytime hours the ABL is primarily composed of the turbulent mixed layer, also referred to as the convective mixed layer. The mixed layer is labeled as convective because the flow is mainly driven by buoyancy effects initiated by convective heat transfer between the surface and the atmosphere. This creates warm air near the surface of the earth which begins to rise, and when coupled with frictional shear forces the resultant turbulence tends to rapidly mix heat, momentum, and humidity. As the day transitions into the night-time hours the radiation heat transfer from the

sun to the ground eases, and the cooling of the surface diminishes the transfer of heat to the air eliminating nearly all forces due to buoyancy. With the buoyancy effects removed, the turbulence in the mixed layer begins to decay, forming two distinct layers known as the residual layer and the stable boundary layer which is illustrated in the middle section of figure 2.2. The residual layer does not come into contact with the earth's surface and is therefore not a boundary layer by definition. The resultant stable boundary layer, labeled as nocturnal due to its frequent presence during the night, experiences periods of short bursts of turbulence occurring within it [2]. When studying turbulence, researchers frequently focus on the period of transition from stable to convective conditions, when the surface temperature and atmosphere are at equilibrium. During this period, the buoyancy effects are typically negligible and the turbulence is predominantly produced only by shear produced between the wind and the surface.

The turbulence within the surface layer is of most interest and is the aim of study for this thesis. Due to the extremely large Reynolds numbers, the huge variability of eddy length scales, and the unpredictable boundary conditions it has proven computationally unfeasible to replicate using modern computer aided tools. Therefore, it is necessary to study the atmospheric boundary layer turbulence experimentally to gain a greater understanding of the turbulence and fluid transport properties within it.

2.3 Techniques to Measure Atmospheric Turbulence

Many techniques have been utilized to acquire turbulence data in the atmospheric boundary layer. Some of these methods include tower point measurements, balloon vertical profiling, sonic detection and ranging (SODAR), light radar (Lidar) sensors, and even aircraft. Tower and balloon point measurements typically take advantage of an array of sensors to gather relevant data and generally provide higher resolution when compared with SODAR and Lidar [12]. Common wind sensors applied on towers

include cup and vane anemometers, sonic anemometers, and hotwire anemometers. SODAR and Lidar are used to profile the velocity field by emitting and measuring the scatter of sound and light respectively. Lastly, aircraft are generally equipped with an instrumentation package to record both atmospheric properties and the platform's motions and can acquire much more data than the alternative stationary techniques as a result of the speeds at which they fly. However, excessive prices and high altitudes at which manned aircraft must fly generally make this technique less desirable, particularly for studying the atmospheric surface layer. The study of turbulence in the atmosphere is by no means restricted to the aforementioned techniques, however these methods are the most common for atmospheric turbulence research, and therefore are expanded upon here.

Towers are among the most widely used platforms for investigating atmospheric turbulence. They are relatively simple to set up and provide substantial versatility in the form of different types of atmospheric sensors aupported. Cup and sonic anemometers, wind vanes, pressure transducers, thermistors, thermocouples, and hotwire anemometers are extensively used on towers to study the exchange of properties in the ABL. In an investigation of the effects of Reynolds number on turbulent properties, Folz and Wallace equipped a tower with an array of 24 hotwire anemometers in parallel to measure turbulence data in the salt flats of Utah [5]. In order to mimic laboratory type conditions the experiments were conducted during early hours providing near-nuetral stablity and the salt flats allowed for a smooth and flat bounding surface. A Dopplar SODAR was utilized by Horiguchi et. al. in order to measure a vertical profile of winds to investigate coherent structures in the atmospheric boundary layer [13]. Again, the measurements were taken at specific times to approximate a near-neutral boundary layer. Both of these experiments, as well as many other tower-based experiments [14–16], require significant setup time, are fixed in space usually in an ideal "laboratory" like setting such as the salt flats of Utah, and are

reliant on the atmosphere convecting past the sensors.

Manned aircraft have been used in atmospheric research for decades in order to mitigate the restrictions imposed by tower-based measurement systems. With manned aircraft it is possible to measure data over a large span of area and altitudes, acquire information over various surfaces, and with the velocities of the aircraft, collect statistically significant data quicker than a tower-based systems. It is possible to equip many of the same sensors that towers employ for wind measurements. Hotwire anemometers are commonly used on manned aircraft as they provide a fast response capable of investigating all scales of turbulence experienced in the ABL. In order to investigate the small-scale turbulence in the atmosphere, Sheih et. al equipped a hotwire probe to a single engine Piper Cherokee and flew in straight line paths at multiple altitudes over a tower-based system [17]. Many similar experiments with manned aircraft have been conducted including measuring mean wind, temperature and humidity profiles [18–21], measuring atmospheric turbulence [17, 22], and even tracking pollutant concentrations [23]. While aircraft alleviate some of the shortcomings of tower based systems, they introduce other disadvantageous traits to atmospheric turbulence research, such as relatively high minimum altitude at which they can collect data, expensive operational costs, safety concerns for the pilot, etc.

Within the past decade, unmanned aerial vehicles (UAVs) have become increasingly useful in the study of the atmospheric boundary layer. They provide an ideal platform for bridging the gap between tower-based systems and manned aircraft. UAVs have recently been used for various research in the ABL including but not limited to agriculture research, gas distribution mapping [24], vertical profiling of wind, temperature, and humidity [25,26], investigation of weather development, and turbulence and wind estimation [27, 28]. The use of unmanned aerial vehicles to conduct measurements in the ABL represents new possibilities for obtaining a spatial description of the structure and organization of turbulence. The ability of a UAV to spatially sample the

flow field using a high temporal response sensor translates into a spatially sampled flow field with reduced reliance on Taylors flow hypothesis. In addition, within the 30 minute period of quasi-stationarity within the ABL a UAV, like manned aircraft, will be able to collect substantially more data than a fixed-point measurement which requires the turbulence to convect past the measurement point. A UAV also has an advantage over fixed towers in terms of portability and the potential to measure in locations where construction of a tower is prohibitive or unfeasible. Finally, UAVs offer distinct advantages over manned aircraft in their ability to safely perform measurements within meters of the surface, the ability to preform measurements in remote locations beyond the range of an airfield, and through greatly reduced operational costs [29].

The majority of the work that has been done in the study of turbulence in the ABL have utilized wind sensors that have a temporal response on the order of that of sonic anemometers. The M2AV UAV by Van den Kroonenberg et al. uses a five hole pitot probe which can resolve all three components of the wind vector to 40 Hz [30]. Mayer et al. developed a UAV that can estimate wind vector solely by comparing constant throttle thrust and the ground speed observed which is sampled at just 2 Hz [31]. The use of a five-hole pitot probe is frequently used to measure wind speed and is applied in the work of Thomas et al. to measure wind speed and direction, potential temperature, and water vapor flux [32]. It would therefore be highly beneficial to employ a sensor with a much greater temporal response, such as a hot-wire anemometer, to a UAV in order to resolve wavelengths in the atmosphere on the order of the Kolmogorov scale [2]. The work in this thesis demonstrates the feasibility of conducting atmospheric turbulence measurements with a hot-wire sensor, discussed further in in chapter 4, however the primary work focuses on the development of a highly robust and reliable unmanned system equipped with a five-hole pitot tube in order to acquire high quality atmospheric turbulence data. The development of

this system will open doors to further the capability of using unmanned systems to investigate that atmospheric boundary layer.

Chapter 3 Data Reduction

The use of aircraft as a research platform introduces an additional level of complexity and difficulty in measuring and analyzing atmospheric data due to the highly dynamic properties and ever-changing state of the airborne platform. Much work has been done over the past decades to develop a data reduction scheme for aircraft being used as atmospheric turbulence research platforms [33–35]. The objective of the measurements is to extract the wind velocity using a velocity signal measured by a multi-hole pressure probe or hot-wire sensor mounted on a vehicle which will be experiencing six degree-of-freedom rotation and translation. We assume the general configuration of the aircraft illustrated in Fig. 3.1 equipped with a velocity sensor aligned with the vehicle axis but mounted a distance from the center of gravity of the vehicle where $\boldsymbol{r}_{S-CG}$ denotes the vector that points from the center of gravity to the measurement volume of the respective wind sensor. We assume that the vehicle is equipped with a true air speed (TAS) sensor such as a Pitot-static tube. We also assume that the vehicle is equipped with an inertial navigation system or sensors, located at, or near, the center of gravity, which can determine the translational position and velocity, $\boldsymbol{r}_{UAV}$ and $\boldsymbol{U}_{UAV}$ respectively. In addition we assume that the rotational position, indicated through the Euler angles of pitch, roll and yaw (θ, ϕ and ψ respectively) and the angular velocity $\boldsymbol{\Omega}_{UAV}$ are provided by the autopilot. Thus, the time-varying position and orientation of the vehicle are known. It is noted that $[\cdot]_I$ denotes a vector in the earth-fixed inertial frame, and $[\cdot]_B$ is used to denote a vector in the vehicle-fixed body frame.

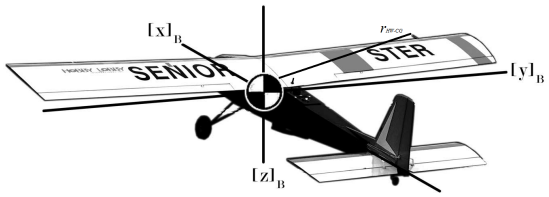

Figure 3.1: *Standard airplane body axes.*

To isolate the wind vector from the sensor measurements, we first note that the traveling probes will also sense the velocity of the plane relative to the velocity of the air in the atmosphere. Therefore, define the recorded relative velocity

$$[\boldsymbol{U}_r]_B = [\boldsymbol{U}_S]_B - [\boldsymbol{W}]_B \tag{3.1}$$

where $\boldsymbol{U}_S = [u_{s1}\ u_{s2}\ u_{s3}]^{\mathrm{T}}$ is the velocity of the sensing volume and $\boldsymbol{W}$ is the velocity of the atmosphere, i.e., the wind. The components of the inertial frame are taken as north, east and down. The components of the body frame are shown in Figure 3.1. Since the sensors face forward, it follows that $\boldsymbol{U}_r = [u_{r1}\ u_{r2}\ u_{r3}]^{\mathrm{T}}$ are the components of relative velocity normal, tangential, and bi-normal to the sensor axis, and are thus the components of velocity measured by the respective sensor.

We start first with the general case in which the applied sensor is capable of resolving these three components of velocity, such as with a multi-hole pressure probe or a three- or four-wire hot-wire probe in which a suitable data reduction scheme (i.e. such as provided by Wittmer et. al [36] or Döbbeling et. al [37]) has been used to convert the voltage measured by the anemometer into velocity magnitude and direction.

Let $[\boldsymbol{U}_{UAV}]_I$ denote the velocity of the vehicle given by the vehicle's inertial navigation system and assume that this measurement is taken at the center of gravity. The velocity of the sensor in the body frame is given by

$$[\boldsymbol{U}_S]_B = [u_{s1}\ u_{s2}\ u_{s3}]^T = [\boldsymbol{U}_{UAV}]_B + [\boldsymbol{\Omega} \times \boldsymbol{r}_{S-CG}]_B, \tag{3.2}$$

where $\boldsymbol{\Omega} = [P\ Q\ R]^T$.

Next, recall that a vector in the inertial frame is transformed into the body frame by $[\cdot]_B = \boldsymbol{L}_{BI}[\cdot]_I$, where

$$\boldsymbol{L}_{BI} = \begin{bmatrix} C_{11} & C_{12} & C_{13} \\ C_{21} & C_{22} & C_{23} \\ C_{31} & C_{32} & C_{33} \end{bmatrix}, \tag{3.3}$$

$$\begin{aligned} C_{11} &= \cos\theta\cos\psi, \\ C_{12} &= \cos\phi\sin\psi, \\ C_{13} &= -\sin\theta, \\ C_{21} &= \sin\phi\sin\theta\cos\psi - \cos\phi\sin\psi, \\ C_{22} &= \sin\phi\sin\theta\sin\psi + \cos\phi\cos\psi, \\ C_{23} &= \sin\phi\cos\theta, \\ C_{31} &= \cos\phi\sin\theta\cos\psi + \sin\phi\sin\psi, \\ C_{32} &= \cos\phi\sin\theta\sin\psi - \sin\phi\cos\psi, \\ C_{33} &= \cos\phi\cos\theta, \end{aligned}$$

and ϕ, θ, and ψ are the roll, pitch, and yaw angles, respectively [38]. Similarly, a vector in the body frame is transformed into the inertial frame by $[\cdot]_I = \boldsymbol{L}_{IB}[\cdot]_B$, where $\boldsymbol{L}_{IB} = \boldsymbol{L}_{BI}^{-1} = \boldsymbol{L}_{BI}^{\mathrm{T}}$.

The desired wind velocity is that in the inertial frame $[\boldsymbol{W}]_I = [u\ v\ w]^{\mathrm{T}}$, where u is the component of wind along the north axis and v is the component of wind along the east axis and w is the component of wind along the vertical axis. The wind velocity in the body frame is then

$$[\boldsymbol{W}]_B = \boldsymbol{L}_{BI}[\boldsymbol{W}]_I \tag{3.4}$$

$$= \begin{bmatrix} C_{11}w_n + C_{12}w_e + C_{13}w_d \\ C_{21}w_n + C_{22}w_e + C_{23}w_d \\ C_{31}w_n + C_{32}w_e + C_{33}w_d \end{bmatrix}.$$

Combining (3.2) and (3.4) with (3.1) leads to

$$[\boldsymbol{W}]_I = [\boldsymbol{U}_{UAV}]_I + [\boldsymbol{\Omega}]_I \times \boldsymbol{r}_{S-CG} - \boldsymbol{L}_{IB}[\boldsymbol{U}_r]_B. \tag{3.5}$$

Thus, the desired quantity $[\boldsymbol{W}]_I$ can be determined from the measured velocities $[\boldsymbol{U}_r]_B$, $[\boldsymbol{U}_{UAV}]_I$, $[\boldsymbol{\Omega}]_I$ and the known quantity $\boldsymbol{r}_{S-CG}$.

In the case where the applied sensor is a multi-hole pressure probe, an additional transformation step to the reduction scheme is necessary. Typical calibration procedures for these probes will result in the sensor reporting the true airspeed along with the aircraft's angle of attack, α, and sideslip angle, β allowing for the calculation of all three components of velocity. The angle of attack and sideslip angle are used to transform the recorded relative velocity, $\boldsymbol{U}_r$, into x, y, and z components using the transformation $\boldsymbol{L}_{BA}$ according to [34, 39, 40] defined as

$$\boldsymbol{L_{BA}} = D^{-1} \begin{bmatrix} 1 \\ \tan\beta \\ \tan\alpha \end{bmatrix}, \tag{3.6}$$

where D is the normalization factor defined as

$$D = \sqrt{(1 + \tan^2\alpha + \tan^2\beta)}. \tag{3.7}$$

The updated equation used to find the desired quantity $[\boldsymbol{W}]_I$ when using the multi-

hole pressure probe is thus

$$[\boldsymbol{W}]_I = [\boldsymbol{U}_{UAV}]_I + [\boldsymbol{\Omega}]_I \times \boldsymbol{r}_{s-CG} - \boldsymbol{L}_{IB}\boldsymbol{L}_{BA}[\boldsymbol{U}_r]_A. \tag{3.8}$$

where $[\cdot]_A$ denotes the additional aerodynamic coordinate system recorded by the multi-hole pressure probe.

Chapter 4 Early Aircraft Development

The development of a reliable unmanned system capable of recording high quality atmospheric boundary layer turbulence data is a continuous effort, with iterative improvements in airframe capabilities as well as on-board instrumentation. The "Boundary Layer Unmanned Experiments Categorizing Atmospheric Turbulence" (BLUECAT) project began with two fixed wing aircraft designed and constructed from scratch using carbon fiber composite materials. These two aircraft, BLUECAT1 and BLUECAT2 respectively, proved our capability to develop such custom aircraft in-house at the University of Kentucky but required significant investiment in both time and money. Consequently, the development of these two generations of BLUECAT airframes has been suspended in favor of lower-cost, simpler, systems in order to facilitate instrumentation development. BLUECAT3 and BLUECAT4 were chosen to alleviate the heavy costs experienced by the preceding UAVs and their preliminary development, tests and results are discussed in this section. BLUECAT3 and BLUECAT4 serve as proof-of-concept systems to test the feasibility and survivability of using hot-wire probes on UAVs to measure the small scales of turbulence in the ABL.

4.1 BLUECAT3

The BLUECAT3 airframe is based on the almost ready to fly (ARF) fixed wing Super Falcon 120 kit, featuring a wing span of 160 cm, a payload capacity of approximately 2.75 kg, and a maximum take-off weight of 8.25 kg. The fuselage of

the aircraft is 200 cm long and only 14 cm at the widest region providing limited space for the on-board systems. The aft of the fuselage is fitted with a DLE-20 20cc gasoline engine capable of outputting up to 1.85 kW at 9,000 rpm. This engine, coupled with 35×25 cm pusher configuration propeller, allows BLUECAT3 to reach cruise speeds of 35 m/s. It is desired to achieve these higher flight speeds with faster response probes because it enables us to obtain statistically significant measurements much faster than typical tower or ground based systems. The fuselage of the aircraft houses the 0.95 liter Dubro fuel tank, the Pixhawk autopilot, the turbulence instrumentation package, and the lithium polymer (LiPo) batteries used to power different systems on the aircraft.

Figure 4.1: BLUECAT3 airframe equipped with hot-wire instrumentation.

Several modifications to the fuselage were needed to accommodate all the systems due to it's limited space and access. These modifications include implementing an additional hatch rearword of the fuselage in order to install the gasoline tank as well as facilitate in the installation of the wings and tail at the flight facility, and adding an external payload bay under the fuselage and wings to provide further room for instrumentation. The hatch was molded using the fuselage of the airframe with fiberglass composite material and the instrumentation bay mold was a custom

design in order to provide ample space while simultaneously limiting disturbances of the airflow around the aircraft. Early flights with BLUECAT3 did not include this pouch and led to the heavier instrumentation shifting the center of gravity up, contributing to the aircraft becoming unstable at the lower flight speeds of takeoff and landing. With the addition of this payload bay underneath the fuselage, the heavier instrumentation, i.e. batteries and constant temperature anemometer, were able to be housed lowering the center of gravity and greatly increasing the stability of the airframe.

4.2 BLUECAT4

BLUECAT4 is a octo-rotorcraft that is commercially available from DJI as the Spreading Wings S1000+. The Spreading Wings octocopter is specificallly designed for high level professional aerial photography and, for that reason, it provides a highly stable and dependable system. The S1000+ has eight 4114 pro KV:400 500 W max power electric motors capable of outputting a total of 4000 W total. The motors, coupled with 38×13 cm, propellers are capable of producing a maximum gross take off weight of 11.3 kg. At 9 kg BLUECAT4 can hover for about 12 minutes while outputting 1500 W. The airframe is constructed from carbon fiber composite and has a diagonal wheelbase of 1.1 meters leading to an empty weight of 4.31 kg. The electric speed controller (ESC) requires a minimum of a 6S LiPo battery outputting greater than 40 Amps in order to meet these specifications. BLUECAT4 uses two 5000 mAH 6S batteries in parallel to satisfy this requirement.

Like BLUECAT3, some modifications were needed to aid in the mounting of the instrumentation package. A 30.5×30.5 cm fiberglass composite shelf was constructed and attached underneath the central hub of the octocopter. This shelf houses all of BLUECAT4's turbulence instrumentation, including the constant temperature anemometer, data acquisition unit, and batteries. Additionally, a long carbon fiber

Figure 4.2: BLUECAT4 multi-rotor equipped with hot-wire instrumentation.

boom was added to the airframe in order to extend the probes out away from the down-wash produced by the propulsion motors. Early flights with BLUECAT4 experienced rather short flight times of approximately ten minutes due to the excess weight brought about by the instrumentation system. It will be necessary to investigate the use lighter sensors and configurations in order to increase the flight time of this airframe which allows for a greater statistical significance of the data being measured.

4.3 Preliminary Experiments

The main focus of the data collection on BLUECAT3 and BLUECAT4 was to implement a hot-wire anemometer for measuring turbulence properties. Each airframe's instrumentation thus consisted of a hot-wire probe and anemometer, Pitot-static sensor, data acquisition unit, a Pixhawk autopilot, and batteries. The hot-wire probe and pitot-static sensor provided measurements of the mean wind speed and wind fluctuations; the data acquisition unit was used to record the output voltages from the hot-wire and pitot sensors; and the autopilot produced the six degree-of-freedom attitude and velocity measurements of the respective aircraft. In addition, the Pixhawk

provided stability improvements for BLUECAT3 and aided the autonomous flight of BLUECAT4 throughout the experiments.

Single-component hot-wire probes were constructed at the University of Kentucky by soldering Wollastan wire to TSI model 1201 hot-wire prongs. Using a 15% nitric acid/water solution, the wire was etched in order to expose the 2.5μm platinum core wire. The acidic solution was routed through a tiny needle creating a small bubble at its tip, into which the wire was maneuvered into using a micro-positioner. This method provides the ability to create hot-wire sensors with great control over the sensing length. For the flight tests with BLUECAT3 and BLUECAT4, wires with length of 500μm were used. This length was specifically chosen to maintain an aspect ratio of 200, which minimizes heat transfer to the prongs and corresponding high order errors in the probe's frequency response.

The output from the hot-wire sensor is routed to a small Model 1750 constant temperature anemometer (CTA). The 1750 CTA utilizes a 5:1 bridge ratio and frequency response reaches up to 100 KHz. A 15 volt supply is necessary to power the unit and an additional control resistor is required to complete the fourth leg of the Wheatstone bridge within the circuit. For the test flights with both airframes a 1.5 overheat ratio was used. Generally a slightly higher overheat ratio is desired when using hot-wire anemometers, however the probes that were made for these had a resistance of around 12 ohms leading the operating resistance of the CTA to increase above the upper limit of 20 ohms. After the hot-wire signal leaves the CTA, it is filtered by a 4th order low-pass LTC1563 anti-aliasing filter designed to meet a cutoff frequency of 10 KHz before data acquisition.

To measure the stream-wise component of velocity in the ABL, the single-component hot-wire was mounted along the roll axis in the nose of BLUECAT3 and extended 16.5 cm forward of the nose by using a stainless steel hot-wire probe holder. The stainless steel probe holder was mounted in the modified nose cone through two holes fitted

with vibration isolating rubber grommets. These vibration isolators were installed in order to improve the survivability of the hot-wire probes to vibrations introduced by the 20cc gasoline engine. Mounting the probe in this forward configuration helps to minimize any error caused by flow disturbances induced from the airframe itself.

In the case of BLUECAT4, a carbon fiber boom was used to extend the sensors past the rotors of the octocopter. A custom, 3D-printed mount was designed to secure the sensors at the tip of the cylindrical carbon fiber boom. The mount had two through holes that housed the Pitot-static sensor and hot-wire probe respectively in a level and fixed position facing radially from the center of the octocopter. The mount was fixed at the edge by inserting the custom mount into the end of the boom and using a cotter pin to anchor it in place. This was done to provide some modularity to the mount in the case of additional sensors being added to the instrumentation system in the future. The completed design was printed using a Makerbot Replicator 3D printer available in the University of Kentucky's wind tunnel laboratory. However, with minimal vibrations compared to that of BLUECAT3 hot-wire survivability was not a concern, although the data has shown to be subject to electric noise from the eight electric-magnetic motors used for propulsion.

In order to determine the distance in front of the nosecone that the probe was mounted on BLUECAT3, a quick study was developed and carried out in the University of Kentucky 2'×2' wind tunnel. The goal of this experiment was to analyze multiple probe locations in front of the airframe and determine a sufficient distance in which the sensor output showed minimum affects from the nosecone. As a result of the airframe of BLUECAT3 being too large to install into the wind tunnel, the nose was cut off of the aircraft and a custom mount was made in order to install it along with the hot-wire probe. The test investigated a total of six distances in front of the nose (3.5", 4.5",6.5",7.5" and 8.5") at the cruise speed of 35 m/s. The power spectrum was calculated after each run to demonstrate the effect of the nose on the

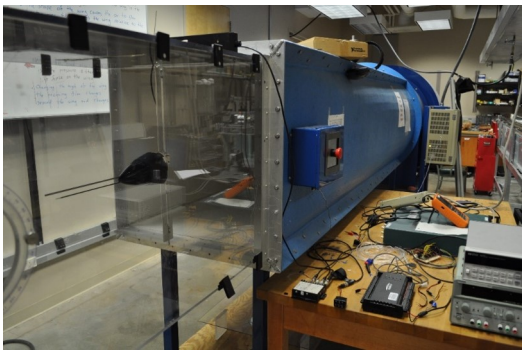

Figure 4.3: BLUECAT3 nose cone in wind tunnel during wind tunnel tests for BLUECAT3 instrumentation.

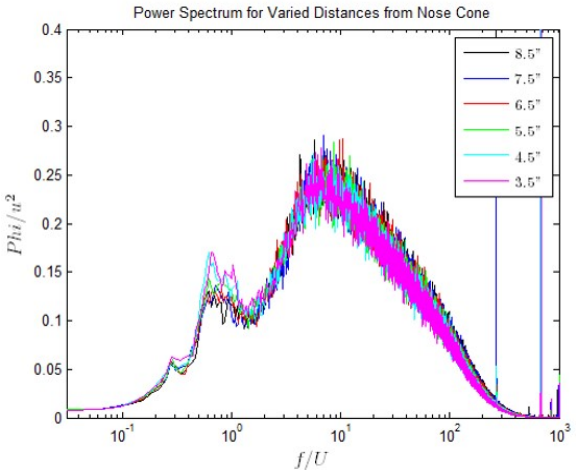

Figure 4.4: Pre-multiplied power spectrum at varied sensor location.

sensors and the setup and resulting plot is shown in figures 4.3 and 4.4. From this information, it was concluded that a measurement location 6.5" or 16.5 cm upstream of the aircraft nose was sufficient to minimize the effect of the nose on the sensor.

Like BLUECAT3, an investigation of probe mounting location was completed for BLUECAT4. In order to test the effective area of the motors on the surrounding air. In this case, a simple flow visualization was set up using theatrical stage fog. For this test, the octocopter was mounted on a 3 meter pole in order to alleviate any ground effects and a SAFE-X foggenerator was used above and below the rotor-craft in order to get a visual representation of the flow structure around the motors as shown in figure(4.5). This led to the designation of a measurement location 45 cm radially outward from the motors as being more than a sufficient distance to avoid downwash from the rotors.

4.4 Preliminary Measurements

A preliminary flight for each system was conducted in October of 2015 in order to test the feasibility of using a hot-wire probe to measure turbulence with an un-

Figure 4.5: BLUECAT4 flow visualization.

manned aerial vehicle. The flight experiments were conducted at the Lexington Model Airplane Club's (LMAC) flight facility located in Lexington Kentucky. The field is equipped with a 650 ft asphalt runway, and was required for the take off and landing of BLUECAT3. The flight path designated for BLUECAT3 followed a back and forth race track pattern into the wind using manual remote control and is displayed in figure. BLUECAT4's preliminary flight experiment consisted of hovering the octo-copter at 100 meters for ten minutes with the probes facing in the direction of the wind. The relatively short ten minute flights were conducted mid-day when the ABL was mixed and unstable in an attempt to pick up turbulent properties in the measurements.

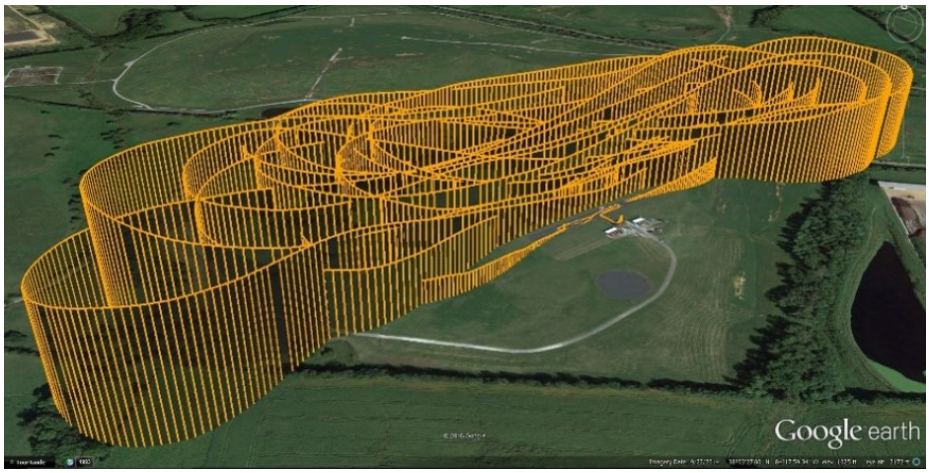

Figure 4.6: Flight path for BLUECAT3 preliminary measurements

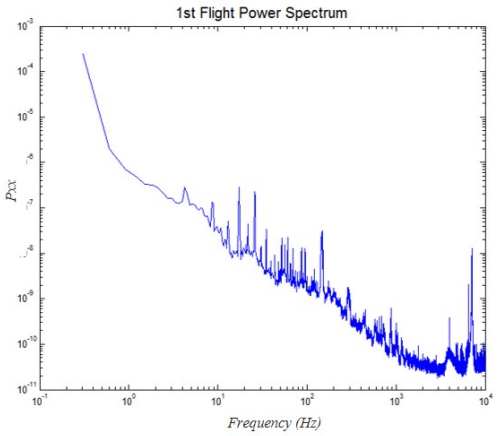

Figure 4.7: Power spectrum from BLUECAT3 preliminary test flight.

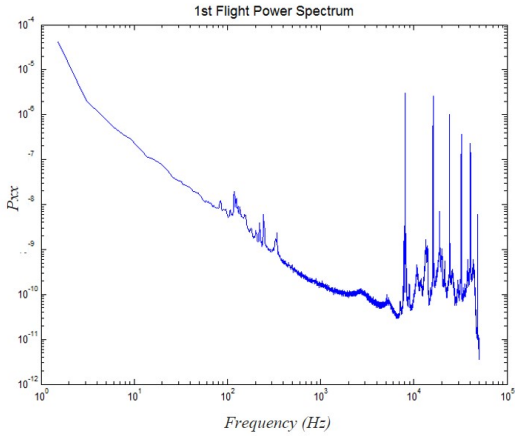

Figure 4.8: Power spectrum from BLUECAT4 preliminary test flight.

The flights demonstrated the survivability of the hot-wire sensors on UAVs despite significant acceleration and vibration being introduced during to takeoff and landing. The initial results in the form of power spectrum are shown in figures 4.7 and 4.8 for both BLUECAT3 and BLUECAT4 respectively. Both power spectra follow the Kolmogrov $-5/3$ slope down to frequencies on the order of 1 kHz (roughly corresponding to a spatial resolution of ≈ 3 cm at the BLUECAT3 flight speed of 35 m/s). There is however noise that frequents the signal which needs to be investigated and eliminated for each system. This preliminary information does allow the conclusion that the unmanned systems discussed above are fully capable of providing quality turbulence data, as seen by the $-5/3$ slope, down to the lowest scales of turbulent structures experienced in the atmospheric boundary layer.

Although promising, these initial experiments also revealed limitations in the systems. For example, the BLUECAT3 gasoline engine was prone to failure and required significant maintenance to ensure reliability. In addition, the aircraft required a paved runway for takeoff and landing and the skill level required of the pilot was high, due to its high flight speeds. The hot-wire probes were also found to be susceptable to breakage caused by engine vibration during takeoff, when the engine hit a low frequency resonant mode. The BLUECAT4 airframe had a very low endurance, limiting

the suitability of this system for investigation of long wavelength turbulence modes, and the stationary nature of the system meant that the Pitot-static tube was not sensitive enough for calibrating the hot-wire. Furthermore if these probes were not oriented directly into the wind, which would have to be done manually, significant errors would be introduced into the measurements.

Although all of these issues were solvable, the additional development effort required was deemed prohibitive for the time allowed and inhibited the broader project intended to obtain high quality turbulence statistics. It was therefore, decided that a more robust system was required to obtain turbulence data. The remainder of this thesis describes the efforts to deliver a reliable combination of airframe and instrumentation, implement the data reduction scheme discussed above, and obtain turbulent statistics which can be used for atmospheric science.

Chapter 5 Aircraft and Instrumentation Package Development

This chapter describes the unmanned aerial vehicle developed for this thesis designed for measurements of atmospheric turbulence, and the instrumentation packaged developed for the aircraft. The development of this unmanned aerial vehicle culminated in a series of flight experiments conducted as part of the first CLOUDMAP (Collaboration Leading Operational UAS Development for Meteorology and Atmospheric Physics) test campaign in Oklahoma, USA. These flights were conducted at two locations: (1) the Oklahoma State University's flight facility (OSU UAFS) located in Glencoe, and (2) the Marena Mesonet and Marena. The test campaign was conducted from Tuesday June 28th. 2016 to Thursday June 30th, 2016 although only measurements made on the 28th (OSU UAFS) and 29th (Marena Mesonet) are reported here. Flight data was acquired from as early as 6:15 AM CST and ended as late as 5:20 PM CST. At each location, multiple profile flights were performed consisting of loitering at altitudes from 20 or 40 meters up to 120 meters in order to investigate the development of the boundary layer throughout the day and straight line flight trajectories at a fixed altitude used to obtain more detailed statistics. Flights were limited to a maximum altitude of 120 meters in compliance with FAA rules and regulations, however a higher altitude may be ideal for future studies. Two aircraft, dubbed BLUECAT5, flying wing UAVs were used for these measurements and a third was built and flown for complimentary measurements of atmospheric chemistry. For the majority of turbulence measuring flights, the two UAVs, equipped identically, were flown simultaneously to both maximize the statistical information recovered from the

flight tests. A total of 18 flights were flown between the two aircraft, resulting in a successful measurement campaign. Details of the airframe, instrumentation and flight tests are provided below, with results from the experiments provided in the following chapter.

5.1 BLUECAT5 Airframe

The flying wing Skywalker X8 is the Almost-Ready-to-Fly (ARF) airframe was used as the foundation for BLUECAT5. This airframe was selected as the foundation as it features a wingspan of 2.1 meters and total payload of $\approx$ 2.5 kg without modifications leading to a total weight of 5 kg. The removable wings and carbon fiber wing spars allow for sufficient portability of the system and minimal setup time. The aircraft is designed to be hand-launched and belly landed, eliminating its reliance on prepared runways. The fuselage of the Skywalker X8 also provides ample room and access for the avionics and measurement instrumentation systems. Like BLUECAT3, BLUECAT5 is fitted with its propulsion system at the rear of the fuselage. However BLUECAT5 makes use of an electric motor coupled with a 33 cm x 20 cm carbon fiber folding propeller. The electric propulsion system provides greater simplicity when compared with the DLE-20 gasoline engined used by BLUECAT3, leading to higher reliability but resulting in reduced endurance. The Axi 4120/14 brushless electric motor used on BLUECAT5 requires a 4S 8000mAh battery utilizing a Phoenix edge lite 75 electric speed controller (ESC). This combination, combined with the relatively lightweight airframe and the large wing area of the aircraft, results in efficient power usage and flight times of close to 45 minutes at 17 m/s cruise speeds. Because the Skywalker X8's fuselage provided sufficient space for excess payload and the sufficient aerodynamic properties of the aircraft, no significant modifications to the airframe were necessary apart from changes required to mount the sensors in the nose and fix the avionics and instrumentation packages within the payload bay.

5.2 Autopilot and Inertial Navigation System

Pixhawk commercial autopilots running the open-source Ardupilot software were used to convert the airframes for autonomous flight. The Pixhawk is a high performance autopilot suitable for both fixed wing and multi rotor configurations. By measuring the six degree-of-freedom attitude and rate information, the Pixhawk is able to provide the necessary PWM outputs to the airframe control surfaces and propulsion motor(s) to allow autonomous flight. The hardware of the pixhawk is a combination of the popular PX4FMU (flight management unit) powered by a 168 MHz 32-bit STM32F427 Cortex M4 core with FPU and the PX4IO (airplane servo and I/O module) which provides a 24 Mhz Cortex-M3 failsafe processor. The FMU houses the necessary sensors for autonomous flight including a ST Micro L3GD20H 16 bit gyroscope, a ST Micro LSM303D 14 bit accelerometer / magnetometer, a Invensense MPU 6000 3-axis accelerometer/gyroscope, and a MEAS MS5611 barometer. The Pixhawk I/O supports 14 pulse width modulation (PWM) / servo outputs along with other abundant communication interfaces including 5× UART serial ports, 2 CAN inputs, FUTABA S.Bus compatible input and output, SPI, I2C interface, 3.3 and 6.6V ADC inputs, and an external micro-USB port extension. In addition, the Pixhawk autopilot provides a micro SD port for long-time high-rate on-board logging of the flight parameters. The power requirements for the autopilot are 4.8 to 5.4V through the supplied power module input as well as an additional 5V power supply to the servo rail.

The relatively small form factor of the Pixhawk at 50 mm × 81.5 mm × 15.5mm and 38 g allowed for expanded flexibility in the implementation of the system. The autopilot unit was mounted near the center of gravity and along the centerline of the BLUECAT5 airframe facing forward through the nose. The PWM control surface outputs were wired out the rear of the autopilot to the respective servo in the wings as

well as to the electric propulsion motor. A few supplementary sensors compatible with the Pixhawk were also required for autonomous flight which included a GPS/compass and an airspeed sensor. A 3DR uBlox GPS with compass provided the position and ground velocity information of the aircraft. This unit was mounted on top of the aircraft along the center line which provided a clear view of the sky for the GPS and distanced the sensor from the electric propulsion motor which caused interference to the magnetic compass. The airspeed sensor used to provide the pixhawk with an accurate true airspeed was a mpxv7002dp pressure transducer connected to a Pitot-static tube mounted in the nose of the aircraft. The airspeed sensor system is discussed further in the next section.

The autopilot is designed to fly in a pattern described using predetermined waypoints defined by altitude, latitude and longitude. These waypoints are designated within the ground station software (Mission Planner) installed on a laptop and used to monitor and control the aircraft flight. While in flight, the ground station is used to monitor the aircraft behavior and flight properties such as heading, attitude, velocity, altitude, etc.. In addition to observing the aircraft, the ground control station is used to alter flight paths, change flight modes, and adjust certain control parameters used for autonomous flight. The communications between the aircraft and ground control station is accomplished via a 900 MHz radio telemetry link between an on-board 3DR telemetry radio and an identical radio connected to the ground station computer. While the parameters and waypoints are adjusted via the ground station, the information is stored on-board the Pixhawk hardware in the aircraft. This means that if connection were lost between the ground station and the UAV, the UAV is able to maintain autonomous flight. Upon completion of the autonomous flight plan, the UAV will enter a failsafe mode if a connection has not yet been established in which the UAV will return to a home waypoint, determined by the position at which the Pixhawk was armed, and loiter until a connection is re-established. This link is

always connected prior to takeoff using the Mission Planner software.

Mission Planner is a full-featured ground control station software used for Ardupilot based autopilots such as the Pixhawk. It is a vital piece to the auto-pilot system in that it is used to install necessary firmware to autopilot; it is used to setup and tune the UAV to reach optimal performance; It allows for the planning, saving, and loading of autonomous mission plans via simple waypoint entry that utilizes Google maps; and finally it is used to download and analyze mission logs created by the Pixhawk which is necessary in the data reduction discussed in this thesis.

In addition to supporting autonomous flight the open source autopilot records the six degree-of-freedom position, velocity, and GPS information needed for the data reduction at 50 Hz, 10 Hz, and 5 Hz respectively. This information is both recorded by the ground control station via telemetry and recorded at the increased frequencies listed above to the micro SD card supported by the Pixhawk. This log file can then be recovered and transferred after landing by the SD card. Initially, the data reduction described in Chapter 3 was intended to be conducted using this information. However, numerous preliminary flight tests revealed that bias was introduced in the resolved wind vector by small inconsistencies in the reported vector. It was determined that the greatest source of this bias was the magnetometer, used to determine aircraft yaw in the inertial frame. Thus, a more accurate inertial navigation system (INS) was required which did not rely on magnetometer data.

The VN-300 from VectorNav was selected as it is an extremely small INS that utilizes dual GPS antennas to provide highly accurate heading measurements without the reliance on magnetic sensors that are typically used. With the aid of advanced Kalman filtering techniques the VN-300 provides a heading accuracy of 0.3° and pitch/roll accuracy of 0.1° with ground velocity accuracy of ± 0.05 ms^{-1}. The INS also provides an increased sample rate of up to 400 Hz for all variables, however a 200 Hz sample rate was used for the experiments. The VN-300 outputs a custom

binary file that is programmable within the software provided with the system. The outputs from the INS for this experiment were attitude angles yaw, pitch, and roll in degrees along with their uncertainties and rates (degrees/second), temperature, pressure, lattitude, longitude, altitude, and GPS velocities in the North, East, and Down directions. The provided software was required to run the VectorNav system and was installed on the on-board personal computer described in a later section.

5.3 Pitot-static tube

As mentioned previously, the UAV was equipped with a 30 cm long, 3.175 mm diameter brass rcats-120 Pitot-static tube produced by RCATS Systems to provide the autopilot with an accurate true airspeed (TAS) reading needed for autonomous flight. In addition, the Pitot-static tube was used to provide a static reference for the turbulence measurement system described below. The TAS information was also used in the data reduction as a reference velocity signal for cross-correlating the autopilot telemetry signal with the turbulence measurement system velocity signal. This Pitot tube was mounted 25 cm out front of the nose of the aircraft away from the fuselage, 3 cm below the five-hole probe. The transducer used with the Pitot-static tube and autopilot was acquired using a Freescale Semiconductor mpxv7002dp differential pressure transducer with a 2 kPa range. This pressure transducer was then connected to the Pixhawk autopilot via the 6.6V ADC pin and was set up and configured via the Mission Planner ground control station software.

5.4 Launcher

Although designed to be hand launched, due to increased weight of the airframe caused by the additional instrumentation, and to increase safety and reliability of takeoffs, a launching system was developed in order to propel BLUECAT5 into flight. Note that landing gear could also have been installed onto the airframe to allow for

runway takeoff and landings, but this would have increased total weight and possibly disrupt some of agreeable aerodynamic characteristics of the flying wing. In addition, a launching system supports more diverse experiment locations because a runway won't be necessary for takeoff or landing.

The designed launcher consisted of a bungee system to pull the aircraft along a pair of rails providing a required angle of attack and airspeed for liftoff. The launcher base was created from 1" PVC pipe to provide a low friction rail system for the aircraft. The launcher is 2 meters long set at a 13° angle ideal for takeoff. The bases and rails of the PVC pipe can be detached in order to make the launching system more portable. The 6 meter super-stretchable abrasion-resistant natural rubber rod (1775T25) bungee from McMaster-Carr was attached to a large ground stake and stretched to approximately 25 meters where it was attached to both a release mechanism and the aircraft itself in order to provide ample force to accelerate the aircraft for takeoff. The release mechanism used to initiate launch was a simple design that utilized a custom made wooden cradle attached to the ground with tent stakes. A steel pin was then slid horizontally through the cradle and one end of the bungee attachment and the launch was triggered by quickly removing the pin from the cradle using a long rope.

The optimal bungee extension of 25 meters was determined from a series of tests in which a test object of similar weight to BLUECAT5 was "launched" along the rails. Multiple launches took place with increasing bungee tensions until a sufficient velocity of 12 m/s was met at the time the board left the rail. In order to attach the bungee cord to the aircraft a plastic hook was added under the nose of the fuselage at an angle that allows the bungee to be discarded after takeoff. The release of the bungee from the UAV occurs as the aircraft flies over the ground stake and all tension is removed from the bungee. the Figure 5.1 displays the launcher system during a BLUECAT5 takeoff.

Figure 5.1: BLUECAT5 takeoff with launcher

5.5 Turbulence Measurement System

To measure turbulence in the atmospheric boundary layer each BLUECAT5 UAV was equipped with a five-hole pressure probe and supporting hardware. The on-board instrumentation included the five-hole probe, pressure transducers, a data acquisition unit (DAQ), and an on-board personal computer (PC). In overview, the geometry of the five-hole probe produced different pressure at each of five ports on its surface relative to the static pressure measured by the Pitot-static tube used by the autopilot. The pressure transducers converted these pressure readings to a voltage, with their high level inputs connected to the different ports of the five-hole probe, and the reference ports connected to the static line from the Pitot-static tube. The voltages from the pressure transducers were digitized by the data acquisition system, which was controlled by the on-board computer which also stored all the information produced by the INS and DAQ. These components are discussed in further detail below and the connectivity of this system is summarized in Figure 5.2. A supplementary image of the connectivity and locations of the major instrumentation components is provided in figure 5.3.

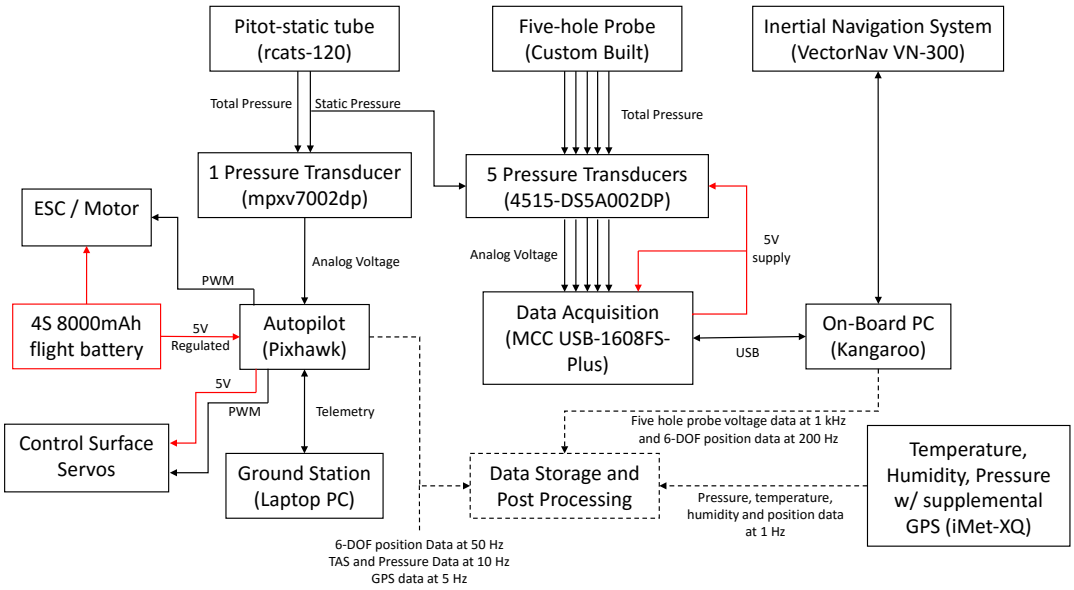

Figure 5.2: Diagram illustrating BLUECAT5 instrumentation connections

5.5.1 Five-hole Probe

Multi-hole probes are designed to determine the magnitude and direction of the local fluid velocity vector. Specifically, on aircraft, they provide the angle of attack and side-slip angles typically denoted by α and β respectively. The five-hole probe is made up of a cylindrical body with on hole along the centerline and four holes evenly spaced cylindrically around an angled tip. Therefore, if the flow of the fluid is not aligned with the center of the probe, each hole will read a different pressure which, through calibration, can be used to estimate α, β and the velocity magnitude.

Multiple versions of five-hole probes for use on UAVs have been developed at the University of Kentucky, with the most recent developed using a Form Labs Form1+ Desktop Stereolithography (SLA) 3D Printer. The five holes on the sensors are 1.2 mm in diameter and the tip of the probe supports a 30° tip angle. Each hole is connected to a differential pressure transducer through 1.75 mm diameter Tygon tubing protected by a 25 cm aluminum tube. The probe was mounted along the x-axis 25 cm in front of the fuselage and 60 cm away from the autopilot to minimize flow dis-

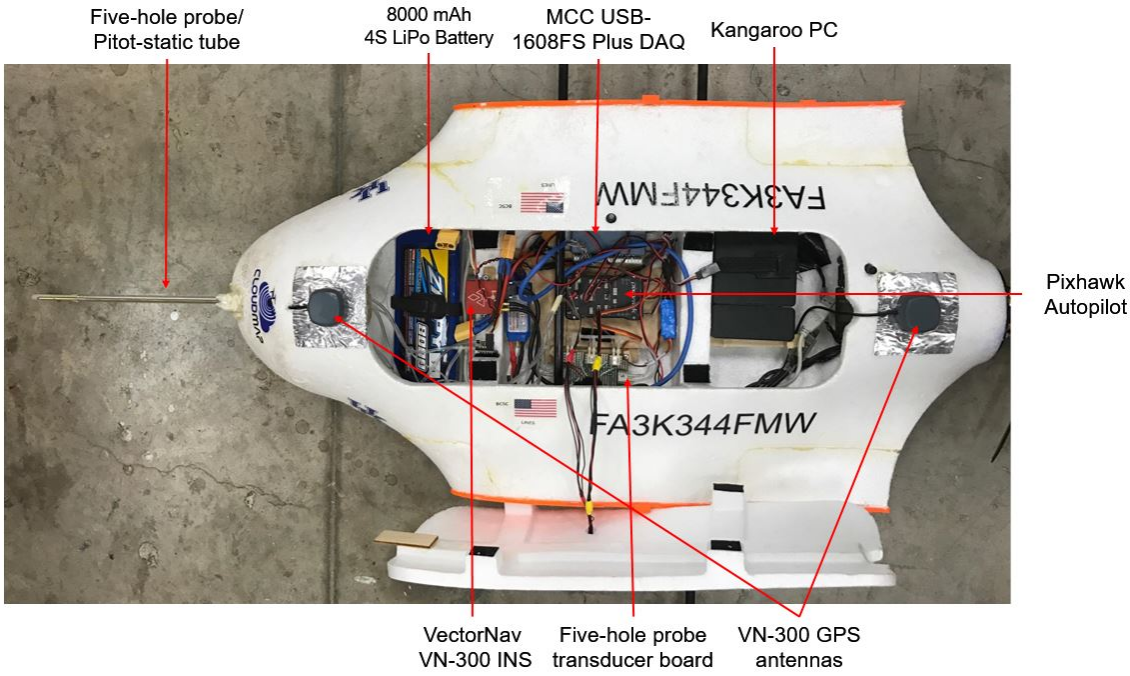

Figure 5.3: BLUECAT5 instrumentation

turbances caused by the airframe. The five-hole probe pressure measurements were acquired using TE Connected Measurements 4515-DS5A002DP differential pressure transducers with a 0.5 kPa range. A custom circuit board was designed and constructed providing a compact layout for all five transducers with optional inputs for 1st order RC low-pass filters. A 100 Hz anti-aliasing low-pass filter was designed and implemented prior to the signal being sent to the data acquisition system. These transducers were powered by the 5 V output from the data acquisition unit.

Before flight, each five-hole probe was calibrated using a $0.3m \times 0.3m$ wind tunnel located in the basement of the Ralph G. Anderson building at the University of Kentucky. In order to complete the calibration, a custom traverse using Vexta stepping motors was designed and mounted to the wind tunnel allowing the probe to both pitch and yaw in with a step accuracy of 0.36°. The calibration followed a standard calibration technique outlined by Treaster and Yocum [41] due to the Wildmann et al. [42] study which showed better results in comparison to the Bohn et al. method [43] which was described and utilized in Kroonenberg's experiment [30]. For

the calibration, the wind tunnel was set to a constant velocity, in this case 17 m/s as this was the cruise speed for the experiments, and the five-hole probe was stepped by 1° intervals between predetermined pitch and yaw angles of -15° and 15° for pitch and -18° and 18° for yaw. At each angle, the current pressure values at each hole P_1, P_2 through P_5 were measured and averaged over five seconds. Additionally a fixed Pitot-static tube was mounted into the wind tunnel to measure the dynamic pressure throughout the calibration as well as provide a static reference for the five-hole probe transducers. More details about the setup, design, and implementation of the calibration of the five-hole probe is provided in Appendix A.

After the data is acquired from the calibration, the coefficients $[a, b, q]$ are determined so that the wind direction and magnitude can accurately be calculated from the pressure at each of the five holes of the probe. Specifically, these coefficients help to determine α, β, and dynamic pressure $P_{dyn} = 1/2\rho u_i u_i$ from the pressure values P_1, P_2, through P_5, whose locations on the five-hole probe are shown in figure 5.4. It is noted that each of the pressures P_1, P_2, through P_5, are measured as differential pressures with a reference to static pressure from the Pitot-static tube.

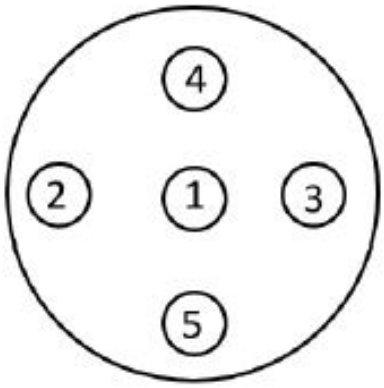

Figure 5.4: Five-hole probe pressure port locations, front view

In order to calculate the calibration coefficients $[a, b, q]$, the following dimensionless

pressure coefficients are calculated from the collected pressure values:

$$C_\alpha = \frac{P_4 - P_5}{P_1 - \Delta P}, \tag{5.1}$$

$$C_\beta = \frac{P_3 - P_2}{P_1 - \Delta P}, \tag{5.2}$$

$$C_q = \frac{P_1 - P_{dyn}}{P_1 - \Delta P}, \tag{5.3}$$

where,

$$\Delta P = \frac{P_2 + P_3 + P_4 + P_5}{4}. \tag{5.4}$$

The coefficients C_α, C_β and C_q are defined as the coefficients of angle of attack, sideslip angle, and dynamic pressure respectively. The role of C_q can be described as a correction value for the dynamic pressure at varying angles of attack and sideslip. These coefficients are used within a polynomial function determined using the known wind tunnel variables α, β, and P_{dyn}. Specifically, these variables can be expressed in terms of the described dimensionless coefficients,

$$\begin{aligned} \alpha &= f_\alpha(C_\alpha, C_\beta), \\ \beta &= f_\beta(C_\alpha, C_\beta), \\ C_q &= f_\alpha(C_\alpha, C_\beta). \end{aligned} \tag{5.5}$$

Here, the functions $f_x(C_\alpha, C_\beta)$ are expressed as an m order polynomial of the two variables

$$f_x(C_\alpha, C_\beta) = \sum_{i=0}^{m} (C_\alpha)^i \left[\sum_{j=0}^{m} X_{ij} (C_\beta)^j \right], \tag{5.6}$$

where X_{ij} are the coefficients $C_{\alpha,ij}, C_{\beta,ij}$, and $C_{q,ij}$ used for the estimation of α, β, and C_q respectively. The estimation is solved by a least squares method for each function

where the order was chosen to be six, thus $m = 5$, for these experiments. It must also be noted that the angles of the probe experimentally calculated within the wind tunnel during calibration, denoted here as α_e and β_e, are related to the analytical estimation of the airflow angles experienced while in flight given by Phillips [40] as

$$\begin{aligned} \alpha_a &= \alpha_e, \\ \beta_a &= \arctan\left(\frac{\tan\beta_e}{\cos\alpha_e}\right). \end{aligned} \tag{5.7}$$

Two aircraft were used for these experiments and consequently two different five-hole probes were utilized, each requiring separate calibration. The two five-hole probes are identified by the monikers Kirk and Spock and the results of their calibrations displayed in figures 5.5 through 5.7. It can be seen in figure 5.5 that the further away from angles (0,0) the probe gets, the more nonlinear the results become making a higher order polynomial necessary for the estimation. Figures 5.6 and 5.7 display the result of using the calibration data to estimate the angle of the flow along with the known angles designated by the stepper motors during calibration. For both α and β the root mean square error (RMSE) was under 0.15° and the RMSE for measured velocity U_r was well under 0.1 ms^{-1} as shown in table 5.1.

Table 5.1: Root Mean Square Error (RMSE) of Calibration Results

Coefficient	RMSE Kirk	RMSE Spock
α	0.0984°	0.1250°
β	0.0976°	0.1248°
C_q	0.0056	0.0099
$\lvert U_r \rvert$	0.05 ms^{-1}	0.09 ms^{-1}

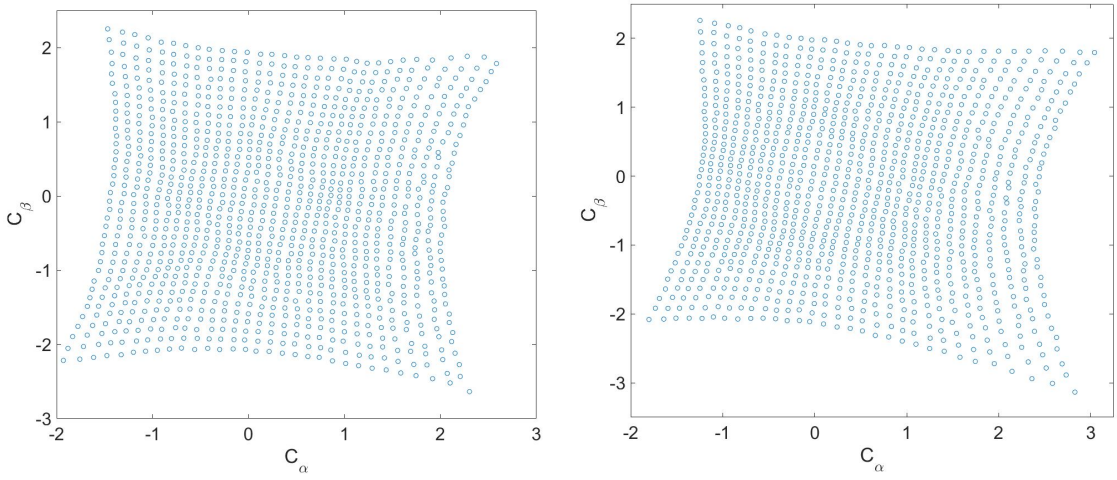

(a) C_α vs. C_β (Kirk) (b) C_α vs. C_β (Spock)

Figure 5.5: Dimensionless calibration coefficients C_α vs. C_β showing nonlinearities for larger airflow angles.

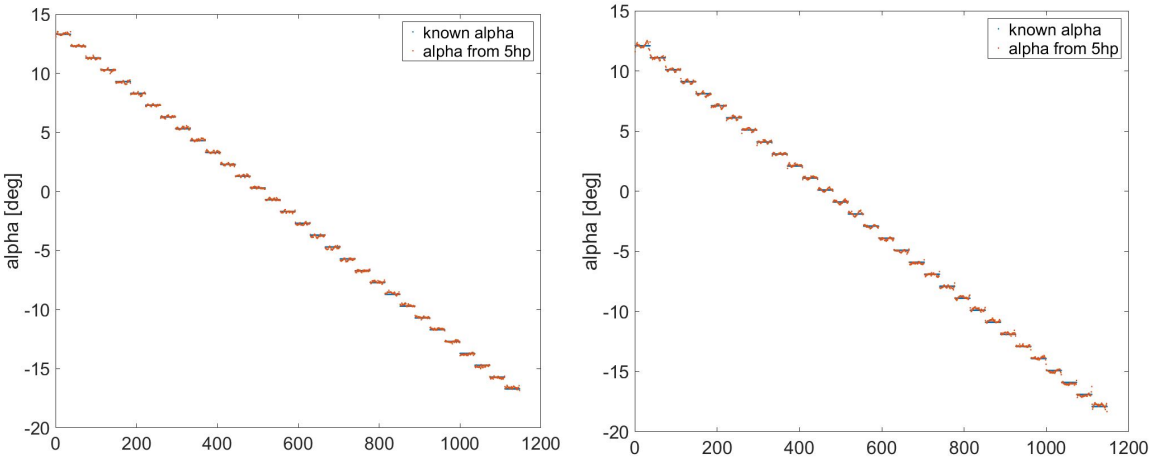

(a) Angle of attack calibration results (Kirk) (b) Angle of attack calibration results (Spock)

Figure 5.6: Calibration results for angle of attack. The figures show both the estimated and known values for α in the order of which the measurements were taken.

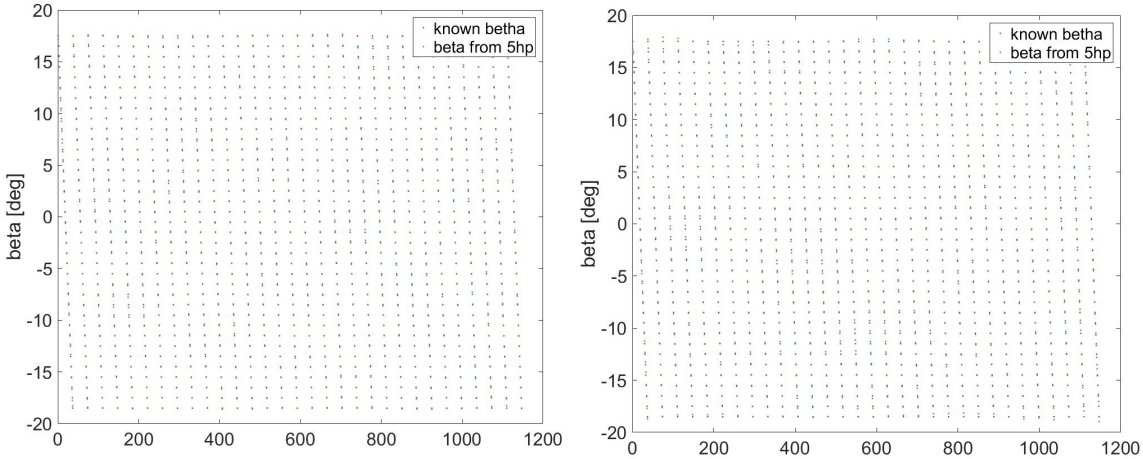

(a) Sideslip angle calibration results (Kirk) (b) Sideslip angle calibration results (Spock)

Figure 5.7: Calibration results for sideslip angle. The figures show both the estimated and known values for β in the order of which the measurements were taken.

5.5.2 Temperature and Humidity Measurements

To measure temperature and humidity during flight, an iMet-XQ UAV sensor was used, which provided a standalone solution for temperature and humidity measurements. The sensor includes a GPS receiver, pressure, temperature and humidity sensors all powered by a rechargeable battery. 16 Mb of data from the sensors can be stored on board and downloaded post flight for analysis via usb. The iMet humidity sensor supports a full 0 - 100% RH range at $\pm$ 5% RH accuracy with a resolution of 0.7% RH. The on-board temperature sensor provides a $\pm$ 0.3°C accuracy with a resolution of 0.01°C up to a maximum of 50°C. The response times of these sensors are on the order of 5 and 2 seconds respectively in still air with the iMet sampling these sensors at 1 Hz.

5.5.3 Data Acquisition

The data acquisition system (DAQ) used to digitize the voltage output from the five pressure transducers, as well as the voltage input to the transducers was an MCC USB-1608FS-Plus data acquisition unit. This particular unit is capable of recording

8 single-ended analog inputs simultaneously at 16 bit resolution at rates of up to 400 kS/s. During the experiments the DAQ recorded six channels at 1 kHz for each channel. The DAQ also provided a 5 V signal to power the pressure transducers.

The DAQ was connected via USB to a Kangaroo Mobile Desktop Computer KJ2B#001-NA having an Intel Atom X5-Z8500 (1.44 GHz) processor, 2 GB LPDDR3 RAM and 32 GB eMMC storage running the Windows 10 Home operating system. A custom Matlab script was written to control the acquisition, compiled as a standalone executable. This script allowed for the selection of which channels were to be recorded, the duration of acquisition, and the voltage range at which each channel was recorded. The Kangaroo PC was also used to simultaneously run the VN-300 INS system through using the manufacturer provided software. The on-board PC stored all recorded data on its 32 GB hard drive from both the data acquisition unit and the additional INS. Data from both systems were stored onboard the eMMC memory and then pulled post-flight via the USB connection for archiving and further analysis.

5.6 Sonic Anemometer

In order to provide a ground reference of wind velocity vector and temperature during flights a Young Model 81000 ultrasonic anemometer was mounted on a 7.5 m tower. The sonic anemometer is a 3-axis wind sensor that provides the three components of velocity in the inertial reference frame as well as a sonic temperature measurement. The 81000 can measure wind speeds up to 40 m/s at a resolution of 0.01 m/s with accuracy of $\pm$ 0.05 m/s. From the three components of velocity the direction of the wind can be provided 360° at a resolution of 0.1° with an accuracy of $\pm$ 2°. The temperature provided by the sonic anemometer is calculated based on the speed of sound leading to an temperature measurement accuracy of $\pm$ 2°C. For the data reported here, the anemometer was set to output four analog voltages, corresponding to u_1, u_2, u_3 and temperature. The velocity components were output

at their maximum sensitivity such that the voltage output could be converted to the velocity in m/s following

$$u_i = [(10 \times 2/5) \times V_i] - 10 \tag{5.8}$$

where V_i is the recorded voltage corresponding to component u_i. The temperature could be converted to deg C following

$$T = [(100/5) \times V_T] + 220 - 273.15 \tag{5.9}$$

where V_T is the recorded voltage corresponding to the temperature.

The sonic anemometer was mounted to on a 7.62 meter tower and the voltage data output from the anemometer recorded by a stand-alone high-speed Omega OM-LGR-5329 multifunction data logger logging at 100 Hz. Both the anemometer and logger were powered by a single 4S 3300 mAh lithium-polymer battery.

5.7 Measurement Procedures

The primary data sets acquired for this thesis were taken with two BLUECAT5 UAVs flying simultaneously with varying flight paths. Each UAV was equipped with identical five-hole probe sensor packages as described earlier in this chapter. The data was recorded on two sequential days in separate locations located near Stillwater, Oklahoma in which vertical profiles were completed to measure atmospheric properties such as mean wind speed, mean wind direction, temperature, humidity, and turbulence characteristics. Before each flight, the instrumentation was started manually through the on-board Kangaroo PC and the autopilot was connected to their respective ground stations. At the start of the data acquisition, zero reference voltages were taken by applying a cover to both the five-hole probe and Pitot-static tube in order to mitigate any wind velocity the sensors might be reading at ground level. The

aircraft were then launched sequentially via the use of the custom-made launcher under manual control. Once positive flight characteristics were confirmed through manual flight, the aircraft were switched to autonomous flight, at which point the autopilot began flying its flight path, defined using pre-determined waypoints. Following approximately 30 minutes of flight time, the aircraft were returned to manual mode and recovered via belly landing on a runway. Immediately after each flight, all relevant flight data including the five-hole probe voltage readings, autopilot logs, VectorNav information and iMet files were transfered to a laptop for validation checks and archiving on an external hard drive. The Kangaroo PCs and iMET sensors and flight batteries were then replaced with ones containing full charge making the aircraft ready for their next flight following an approximately 15 minute turnaround time. A more detailed checklist for the measurement procedure is provided in Appendix B.

Flight details for each day are outlined in this section. All flights were flown under the University of Kentucky's blanket FAA Blanket Area Public Agency certificate of authorization (COA) number 2016-ESA-32-COA.

5.7.1 Tuesday, June 28, 2016

The first set of data presented are from flight tests conducted throughout the day on June 28, 2016. The flights were executed between 6:15 AM and 5:20 PM CST at Oklahoma State's Unmanned Aircraft Flight Station(UAFS) in Glencoe, OK, USA. The UAFS is a dedicated UAV flight and test facility used by both hobbyists and researchers at Oklahoma State University located 12 miles East of Stillwater, Oklahoma. The flight station supports two runways (183 and 122 meters), an aircraft hangar and a state-of-the-art control room with monitoring capabilities. The flight area consists of a 1.61 by 1.61 km unpopulated land to use for research, education and outreach in UAS. A satellite image of the Unmanned Aircraft Flight Station flight area using Google Earth is shown in figure 5.8 as well as a top-down view of the flight

patterns for each UAV. The flight area elevation varied by ± 5 meters throughout the flight paths. The blue flight path represents BC5A's loiters, the red flight path depicts BC5B's straight line flights, the blue diamond represents the location of the sonic anemometer, and the green marker shows the location and direction of takeoff for each UAV.

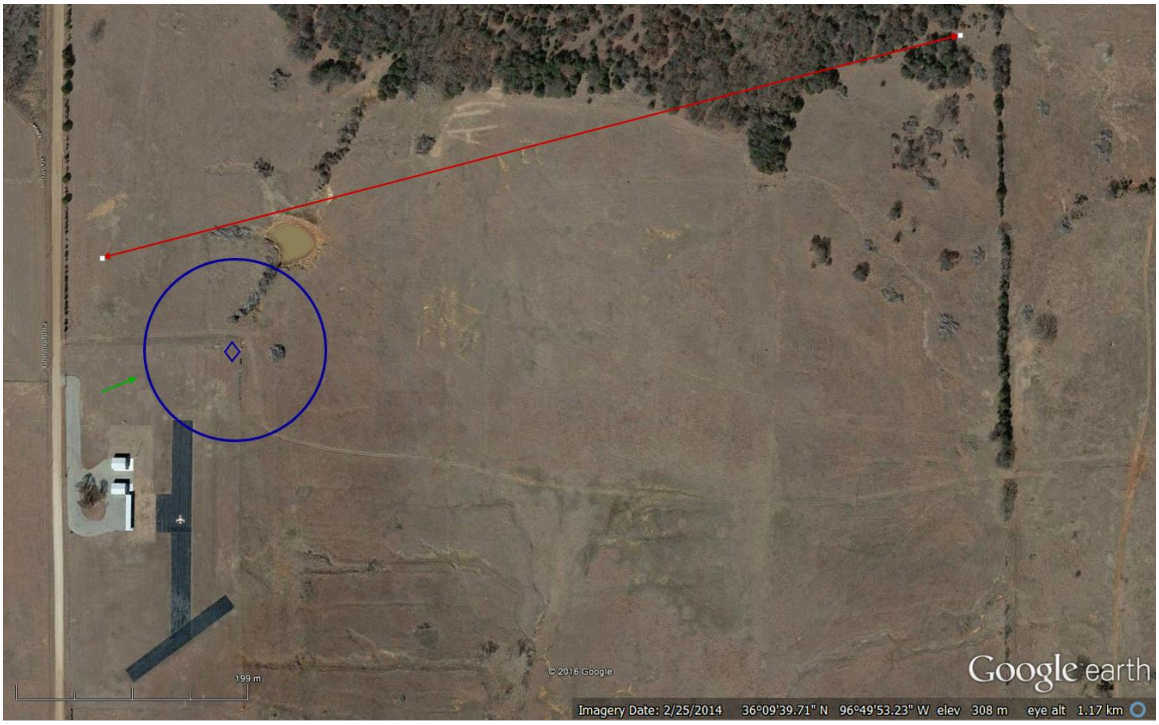

Figure 5.8: Oklahoma State's Unmanned Aircraft Flight Station with day one experiment's flight paths. Blue circle: BC5A flight path; Red Line: BC5B flight path; Blue diamond: Sonic anemometer; Green arrow: takeoff location and direction.

The UAVs used in these experiments will be referred to as BLUECAT5 A (BC5A) and BLUECAT5 B (BC5B) for simplicity. BC5A followed a loitering profile pattern for each flight throughout the day in which the aircraft held a predesignated altitude for 2.5 minutes while flying in a circle of radius 80 meters before climbing to the next altitude and repeating. A total of five distinct altitudes were executed for each profile ranging from a minimum of 20 meters above ground to a maximum altitude of 120 meters for each flight limited due to FAA COA limitations. A maximum of two profiles were flown per flight and a total of nine flights with BC5A were completed.

An overview of the flight details of BC5A are listed in table 5.2 below and a three dimensional depiction of the flight path is displayed in figure 5.9. Throughout the day the hourly weather data was reported by the NOAA near Stillwater Regional Airport and is summarized to the nearest flight in table 5.4 below.

Table 5.2: Tuesday, June 28, 2016 Flights Overview for BLUECAT5 A (Profile)

Flight #	Takeoff Time (CST)	Altitudes (m)	# of Profiles
1	6:18 AM	(40,60,80,100,120)	2
2	7:21 AM	(20,40,60,80,120)	2
3	8:10 AM	(20,40,60,80,120)	2
4	9:01 AM	(40,60,80,100,120)	1
5	10:00 AM	(40,60,80,100,120)	2
6	11:10 AM	(40,60,80,100,120)	2
7	1:21 PM	(40,60,80,100,120)	2
8	3:08 PM	(40,60,80,100,120)	2
9	5:20 PM	(40,60,80,100,120)	2

BC5B was flown at a constant altitude of 50 m following a straight line path approximately parallel to the direction of the wind wind for the duration of the flight. A total of six flights were completed with the BC5B airframe, however data was only successfully recovered from the latter four flights. An overview of the flight details of BC5B are shown in table 5.3 below.

Table 5.3: Tuesday, June 28, 2016 Flights Overview for BLUECAT5 B (Line)

Flight # (BC5A #)	Takeoff Time (CST)	Altitudes (m)	Flight Direction
1 (3)	8:07 AM	50	NE
2 (5)	9:57 AM	50	ENE
3 (6)	11:06 AM	50	NE
4 (8)	3:06 PM	50	NE

In addition to the simultaneous flights of BC5A and BC5B, the sonic anemometer was used throughout the day. The objective of the sonic anemometer is to provide a reference with respect to wind speed and direction as well as provide an additional measurement point at 7.5 m. The tower was fixed in the northeast corner of the

Table 5.4: NOAA Observed Weather Data on 6/28/2016 near Stillwater, OK

Hour	Condition	Temperature	Humidity	Wind (from)
6:00 AM	Fair	21.7° C	96% RF	Northwest at 1.5 m/s
7:00 AM	Fair	22.8° C	94% RF	Northeast at 2.1 m/s
8:00 AM	Fair	26.1° C	82% RF	North at 1.5 m/s
9:00 AM	Fair	28.9° C	67% RF	North at 1.5 m/s
10:00 AM	Fair	31.1° C	57% RF	Variable at 2.6 m/s
11:00 AM	Fair	31.7° C	55% RF	Variable at 2.1 m/s
1:00 PM	A few clouds	32.8° C	49% RF	Northeast at 3.1 m/s
3:00 PM	Fair	34.4° C	44% RF	Northeast at 5.1 m/s
5:00 PM	A few clouds	33.3° C	44% RF	East at 4.6 m/s

UAFS underneath the flightpath of BC5A in order to continue the vertical profile of the UAV. The sonic anemometer was started at the beginning of the day and was set to acquire data until stopped manually.

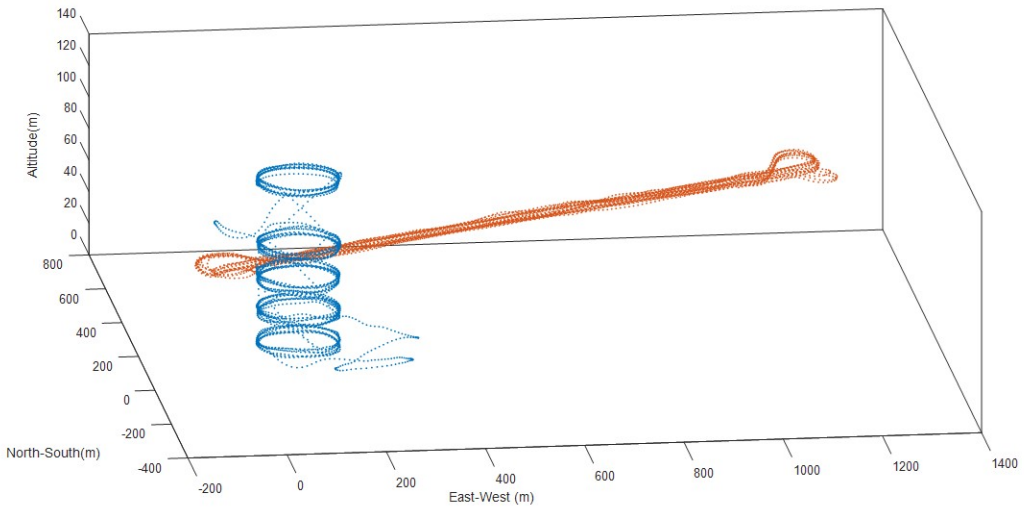

Figure 5.9: Flight paths for 6/28/2016 experiments at OSU UAFS

5.7.2 Wednesday, June 29, 2016

The second set of data presented in this thesis are from flight experiments on June 29, 2016. Flights began at 7:41 AM and concluded at 1:05 PM CST at the Marena Mesonet in Marena, OK, USA. The Mesonet is described as a world-class environ-

mental monitoring stations and Oklahoma contains a total of 121 stations spread across the state. The Mesonet consists of a 10-meter-tall tower containing multiple instruments to measure the environment every five minutes. The measurements provide parameters such as barometric pressure, relative humidity, air temperature, wind speed, and wind direction between 0.75 m and 10 m. Because the Marena Mesonet site was not a designated flight facility like UAFS, a grass runway was mowed near the instrument to provide a section for landing. The flight area was similar to that provided at UAFS but no definitive boundary was defined. A satellite image of the Marena flight area using Google Earth is shown in figure 5.10 as well as a top-down view of the flight patterns for each UAV. The flight area elevation varied by $\pm$ 2 meters throughout the flight paths. The blue flight path represents BC5A's loiters, the red flight path depicts BC5B's loiter flight path, the blue diamond represents the location of the sonic anemometer, and the green marker shows the location and direction of takeoff for each UAV.

Fewer flights were flown in comparison to the Tuesday flight campaign as a result of rougher landing conditions at the Marena site increasing risk of airframe and instrumentation damage during landings. Again, both BLUECAT5 A and BLUECAT5 B were flown simultaneously with BC5B introducing a different flight path for this experiment. BC5B was flown in a concentric loiter around BC5A's loiter at a radius of 100 meters. Each UAV began their respective flight path at opposite end point altitudes (i.e. BC5A started at 40 m and BC5C started at 120 m) and ascended or descended through five distinct altitudes before reversing the process and descended or ascended to their respective starting altitude. The sonic anemometer tower was again used to provide a reference wind measurement as well as additional data at 7.5 m. Table 5.5 provides information for the flights at the Marena site for both BLUECAT5 A and BLUECAT5 B and the flight path is illustrated in figure 5.11. The weather data again was reported by the NOAA near Stillwater Regional Airport

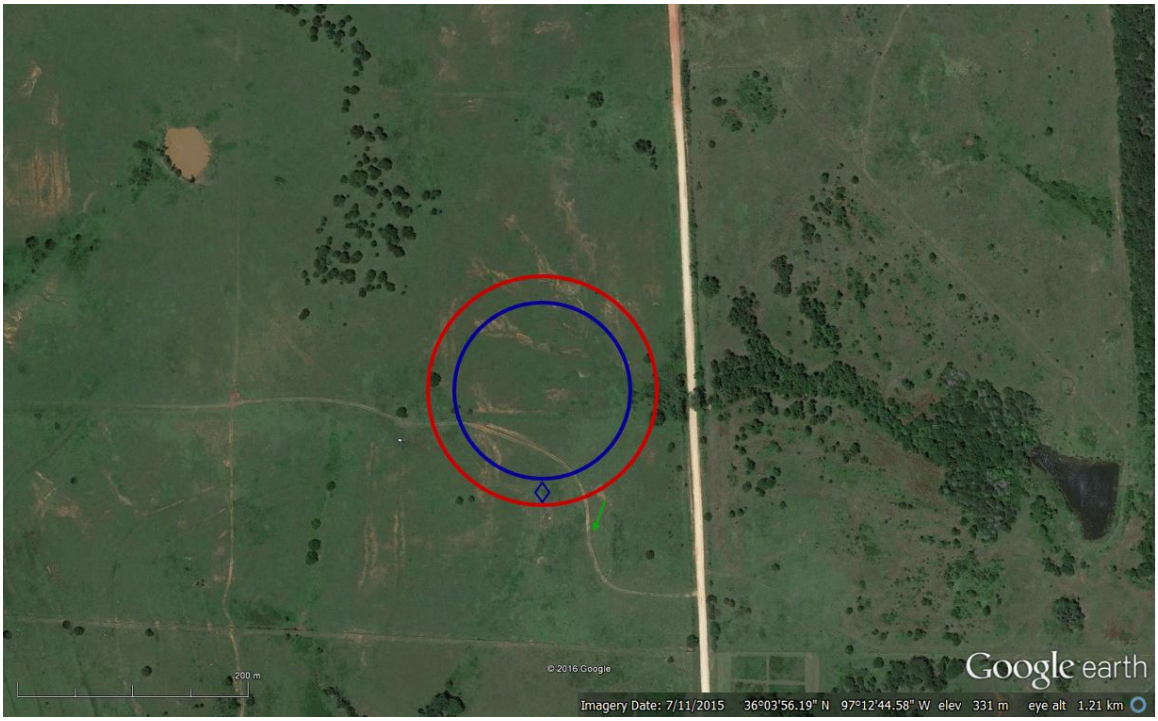

Figure 5.10: Marena Mesonet location with day two experiment's flight paths.Blue circle: BC5A flight path; Red circle: BC5B flight path; Blue diamond: Sonic anemometer; Green arrow: takeoff location and direction.

and is summarized in table 5.6 below.

Table 5.5: Wednesday, June 29, 2016 Flights Overview

Flight #	BC5A Takeoff	BC5B Takeoff	Radius (m) A/B	Altitudes
1	7:41 AM	N/A	80 / 100	(40,60,80,100,120)
2	9:57 AM	9:58 AM	80 / 100	(40,60,80,100,120)
3	1:09 PM	1:05 PM	80 / 100	(40,60,80,100,120)

5.8 Implementation of Data Reduction

In order to implement the data reduction scheme described in Chapter 2, the inertial data from the VectorNav INS consisting of the UAV's velocity, Euler angles, and Euler angle rates were needed in conjunction with the airspeed and direction given by the five-hole probe. The five-hole probe data were sampled by the on-board data acquisition system at 1 kHz where as the VN-300 INS sampled the inertial data at

Table 5.6: NOAA Observed Weather Data on 6/29/2016 near Stillwater, OK

Hour	Condition	Temperature	Humidity	Wind (from)
8:00 AM	Fair	22.2° C	79% RF	Southwest at 3.1 m/s
10:00 AM	Fair	26.7° C	64% RF	South at 3.1 m/s
1:00 PM	Fair	31.1° C	48% RF	South at 4.6 m/s

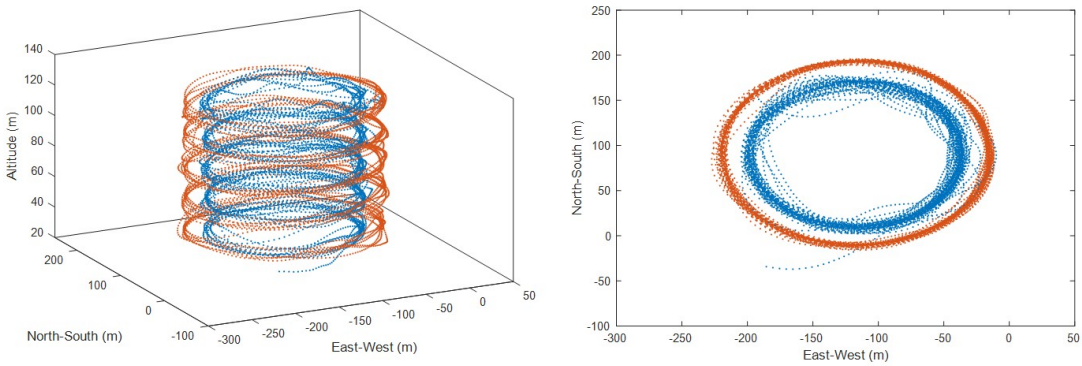

Figure 5.11: Flight paths for 6/29/2016 experiments at Marena Mesonet. Left: Isometric view of flight path. Right: Top-down view of flight path

200 Hz. In fact, between the four separate data systems that were described earlier in this section, including the five-hole probe data acquisition system, the Pixhawk autopilot, the VectorNav VN-300 INS, and the iMet temperature and humidity sensor, each system was established with varying acquisition rates and start times during the experiments. The acquisition rates for each system can be found in table 5.7 . Because of this, the first step to the data reduction is to align the respective data systems time series and re-sample the data at a consistent rate.

Table 5.7: Acquisition Rates for On-board Instrumentation Systems

System (Component)	Acquisition Rate
Pixhawk (6-DoF attitude)	50 Hz
Pixhawk (Airspeed and barometric pressure)	10 Hz
Pixhawk (GPS data)	5 Hz
iMet-XQ	1 Hz
USB-1608FS-Plus data acquisition unit	1000 Hz
VectorNav VN-300 INS	200 Hz

To complete the alignment between the VN-300 INS and the five-hole probe data,

the Pixhawk autopilot was used as a reference signal to which the other data systems were aligned to. The Pixhawk's GPS velocity, measured at 5 Hz, is used to align the VN-300 INS and the Pixhawk's air velocity data, measured at 10 Hz, is used to align the five-hole probe measurements. This is done firstly by assuming the UAV position and orientation smoothly transitions between sample points in the data log, allowing for interpolation of the relevant Pixhawk data to 200 Hz using a cubic interpolation scheme. Similarly the five-hole probe data is re-sampled from 1 kHz to 200 Hz as the filter used for the pressure transducers was set to a 100 Hz cut-off frequency. With the data set to identical sample rates, the relative time difference between the start of each set of time-series data was then determined by cross-correlating the Pixhawk data with the respective data from the sensors recorded by the DAQ and VN-300 INS. Before correlation between the five-hole probe data and the Pixhawk's airspeed data, the voltage output from the central hole on the five-hole probe was converted to velocity so that the information being correlated represented the same measurement. Identification of the location of maximum in the cross-correlation allowed determination of the relative shift between the initiation of sampling between the INS and five-hole probe and Pixhawk data, consequently aligning the two INS and five-hole probe data streams. As a result $[r_{UAV}(t_i)]_I, [U_{UAV}(t_i)]_I, [\Omega(t_i)]_I$ and the transformations $L_{IB}(t_i)$ and $L_{BA}(t_i)$ became known, where t_i is the time corresponding to each discrete sample of the five-hole probe velocity, $[U_r(t_i)]_B$, and direction, $\alpha(t_i)$ and $\beta(t_i)$. From this information the wind vector $[W]_I$ was calculated from equation 3.8.

Chapter 6 Results

This chapter presents results from the profile measurements taken during the Oklahoma test campaign. The results are organized by the day the measurements were recorded. Section 6.1 presents the results from the flight experiments on Tuesday, June 28, 2016 and section 6.2 contains the results from the flight tests conducted on Wednesday, June 29, 2016. For each flight, the altitude dependence of the mean wind velocity, potential temperature, humidity, and turbulence statistics was investigated.

6.1 Tuesday, June 28, 2016

The flights at Oklahoma State University UAFS occurred on Tuesday, June 28 2016. A total of nine flights were conducted, four of which were conducted simultaneously with a second UAV flying a linear flight track, with the profile measuring flights between 20 and 120 meters altitude. An overview of the flights are provided in tables 5.2 and 5.3. For each flight, two profiles were flown with each profile consisting of the aircraft loitering in circular orbits at five different altitudes for approximately 2.5 minutes at each altitude. Each atmospheric parameter investigated was then averaged using the data acquired during the loiter at the specific altitude. In addition to the profile data, the same atmospheric parameters measured by the second UAV flying straight line paths at a constant 50 meter altitude were also calculated. Finally a tower-based sonic anemometer located at the center of the orbit provided the low altitude data shown in this section. The symbols used to identify the data source are provided in table 6.1. The mean wind velocity are presented in section 6.1.1.

Sections 6.1.2 and 6.1.3 contain the profiles of potential temperature and humidity. The turbulence properties of the atmospheric boundary layer are discussed in section 6.1.4.

Table 6.1: Symbols for 6/28/2016 flight experiments

Symbol	Platform	Flight Pattern
○	BC5A	Profile 1
◇	Sonic Anemometer	Profile 1
○	BC5A	Profile 2
◇	Sonic Anemometer	Profile 2
□	BC5B	Lines (50 meter alt)

6.1.1 Mean Wind Velocity

The three components of wind, $\boldsymbol{W}(t) = u(t)\vec{e}_1 + v(t)\vec{e}_2 + w(t)\vec{e}_3$, determined using the data reduction scheme previously described in Chapter 3. The wind velocity profiles were measured from early morning to late afternoon in order to investigate the development of the boundary layer throughout the day. The mean wind velocity magnitude from each UAV is plotted for each flight in figure 6.1 and the direction is displayed in figure 6.2. In addition to the data from the UAVs, the tower equipped sonic anemometer is also shown, providing the lowest altitude data point for each profile.

During the initial flight at 6:18 AM a clear boundary layer was observed in the wind velocity magnitude with the wind velocity increasing in magnitude as altitude is gained, consistent with the expected boundary layer behavior. The readings from the sonic anemometer are also consistent with the data acquired by the UAVs, particularly early in the morning. As the day progresses, a larger shear can be seen between the tower measurement and the lowest data acquired from the aircraft as the bound-

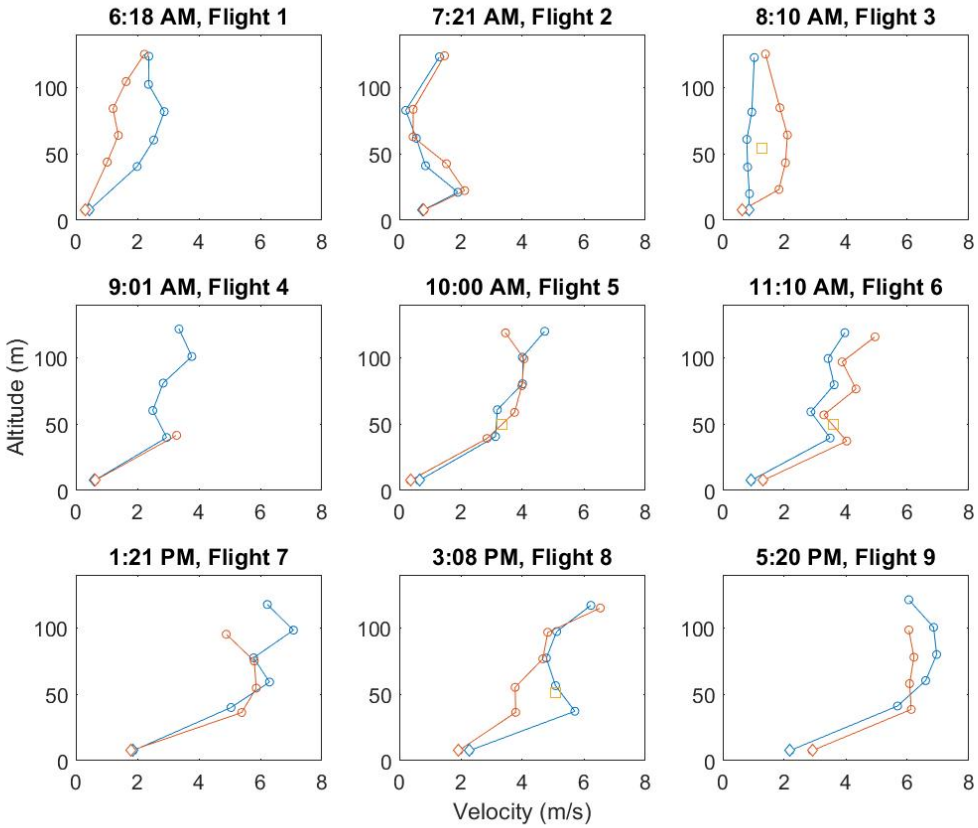

Figure 6.1: Mean wind velocity profiles for June 28, 2016 flights. Symbols as in table 6.1

ary layer transitions from stable conditions to those of a convective boundary layer. As shown later, this results in stronger turbulent flow, which results in enhanced transport of momentum between the surface and the atmosphere with a corresponding increase in shear near the surface. This transition is due to the heating of the earth from the rising sun which inverts the temperature gradient in the atmosphere, producing additional turbulence due to buoyancy-driven convection. In addition to a larger shear between the two lowest altitudes, the mean wind velocity demonstrates larger magnitudes as the day progresses and was even found to increase between the two profiles flown by BC5A during the same flight. For example as observed in flights 1, 3, and 6. In addition, the BC5B aircraft flying results taken at 50 meters agrees with the data measured by BC5A.

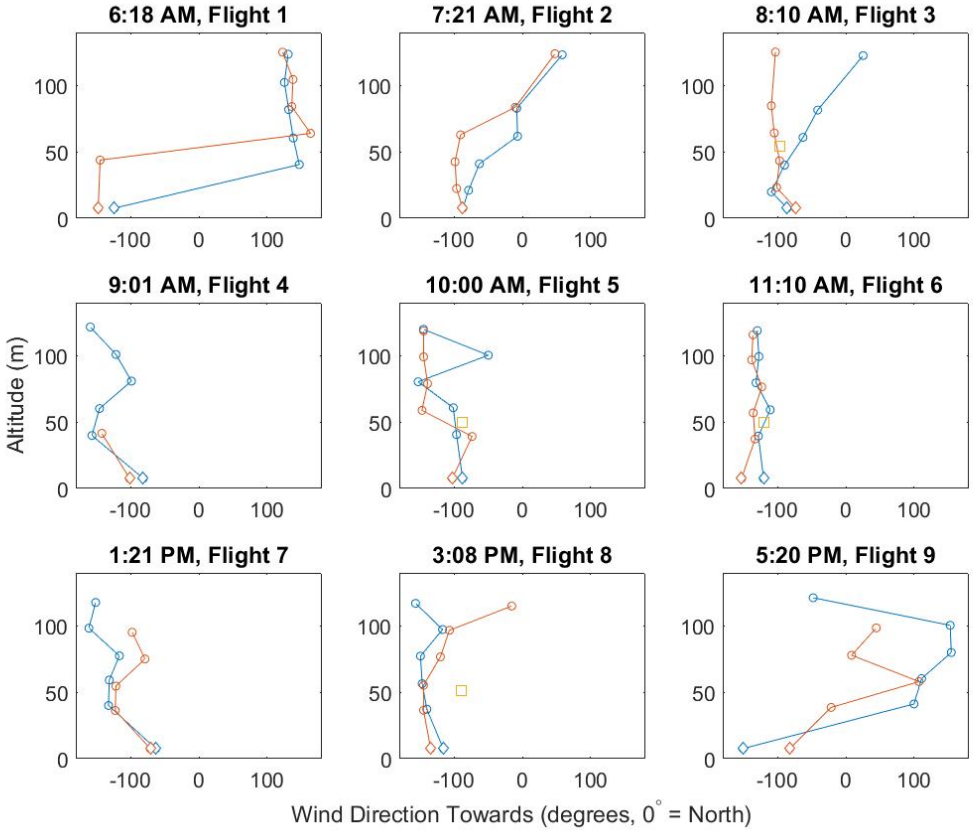

Figure 6.2: Mean wind direction profiles for June 28, 2016 flights. Symbols as in table 6.1

The wind direction, ϕ, was calculated based off of the 2-D wind vector (i.e. East-North) using simple trigonometry by, $\phi = tan^{-1}\frac{v}{u}$. The wind directional vector is thus defined as 0° being towards north and thus 180° is equal to -180°. The direction of the wind changed frequently throughout the day and even multiple times per flight. During flight 1, the wind was essentially from the north (180°) for both profiles. During flight 2, the winds aloft shifted to such that the the direction became highly altitude dependent, varying between -100° at low altitude and 100° at 120 m, eventually settling to being from the east (approximately -100°) during flight 3, which is where it stayed until the last flight of the day. During this last flight, the wind direction varied significantly with altitude, with a direction shift of over 180° evident. Throughout the day, the UAV acquired data was consistent with those

measured by the tower-based sonic anemometer. Also, when both BC5A and BC5B were simultaneously taking data the wind direction was consistent between the two aircraft.

6.1.2 Potential Temperature

Potential temperature is defined as the temperature that a fluid particle would have at standard conditions, after correcting for pressure or compressibility effects. More precisely, it is the temperature that a fluid particle would have if its pressure were adiabatically brought to 1.0 bar. By using this definition, the temperature at each measured altitude in the flight experiments is only a measure of heat content and not correlated to pressure differences brought about by altitude changes. In this way potential temperature is a useful tool to evaluate the stability conditions imposed by the atmospheric boundary layer during flight.

To calculate potential temperature, a relationship is established between both the temperature and pressure recorded by the UAVs allowing an approximation of potential temperature, Θ, to be found from

$$\Theta = T\left(\frac{p_0}{p}\right)^{R/C_p}, \tag{6.1}$$

where T is the absolute temperature measured by the aircraft's iMet sensor, p_0 is the standard atmospheric pressure ($p_0 = 1atm = 1bar = 101,325Pa$), p is the local atmospheric pressure in Pascals recorded by the aircraft's INS, and R/C_p is the ratio of the gas constant to specific heat at constant pressure, which is equal to 0.286 for air. The sonic anemometer's potential temperature relied on the UAV measurements of atmospheric pressure at an altitude of about 7.5 meters. The stability of the ABL can inferred from the potential temperature profiles such that:

- A potential temperature decrease, i.e. $d\Theta/dz < 0$, is taken to be unstable;

- A uniform potential temperature, $d\Theta/dz = 0$ is labeled as neutral;
- And a potential temperature increase $d\Theta/dz > 0$ shows a stable atmosphere .

where z represents altitude. The estimated potential temperature and potential temperature variance are shown in figures 6.3 and 6.4 below.

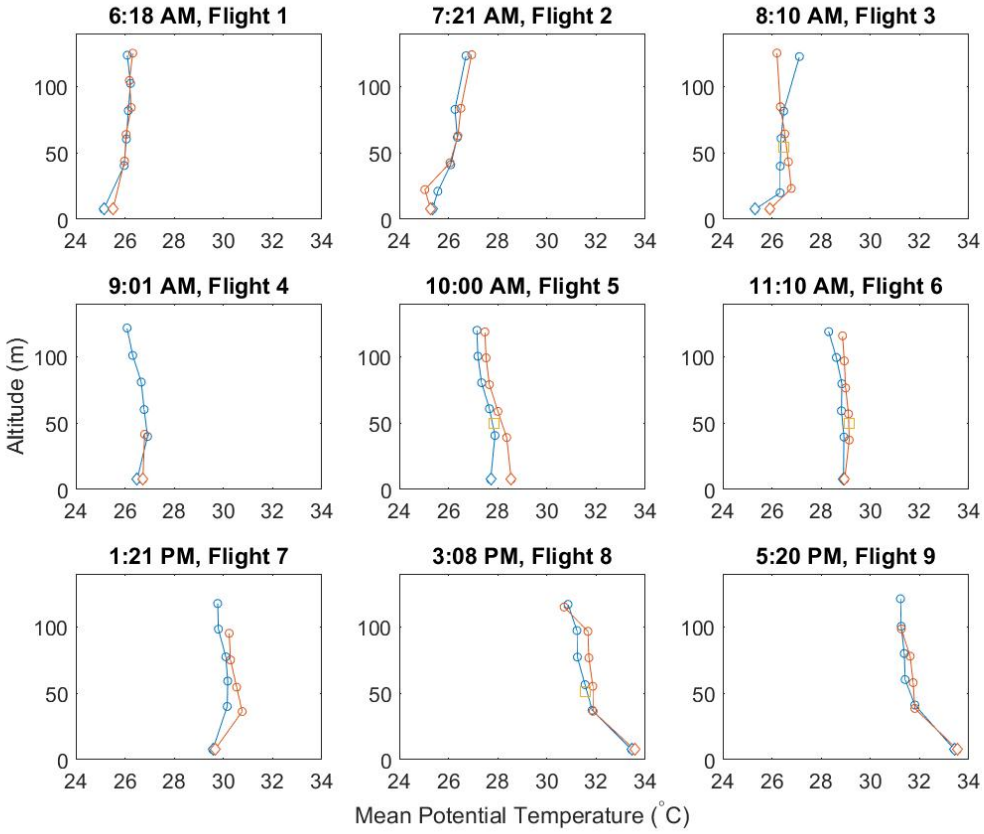

Figure 6.3: Mean potential temperature profiles for June 28, 2016 flights. Symbols as in table 6.1

Based on the guidelines of atmospheric stability according to potential temperature discussed above, a stable boundary layer can be observed throughout the first two flights of the day where the potential temperature increases with altitude. This phenomenon is commonly referred to as a temperature inversion. The inversion shift between a stable boundary layer to neutrally stable boundary layer seems to occur during flight three which started at 8:10 AM. Flights four through nine follow a typical

temperature profile for a convective surface layer, although for flight 6 it appears that there might have been a brief period of near-neutral stability. The measurements from the BC5B aircraft agree extremely well with the potential temperature measurements provided by BC5A reinforcing confidence in the measurements made by the UAVs. Although the temperature from the sonic anemometer agreed with the general trend of the aircraft-based measurements, there are some flights where the anemometer is $\pm 2^{\circ}$ C from the value which would be extrapolated from the aircraft trend. Note that this is the stated accuracy of the sonic anemometer's temperature measurements.

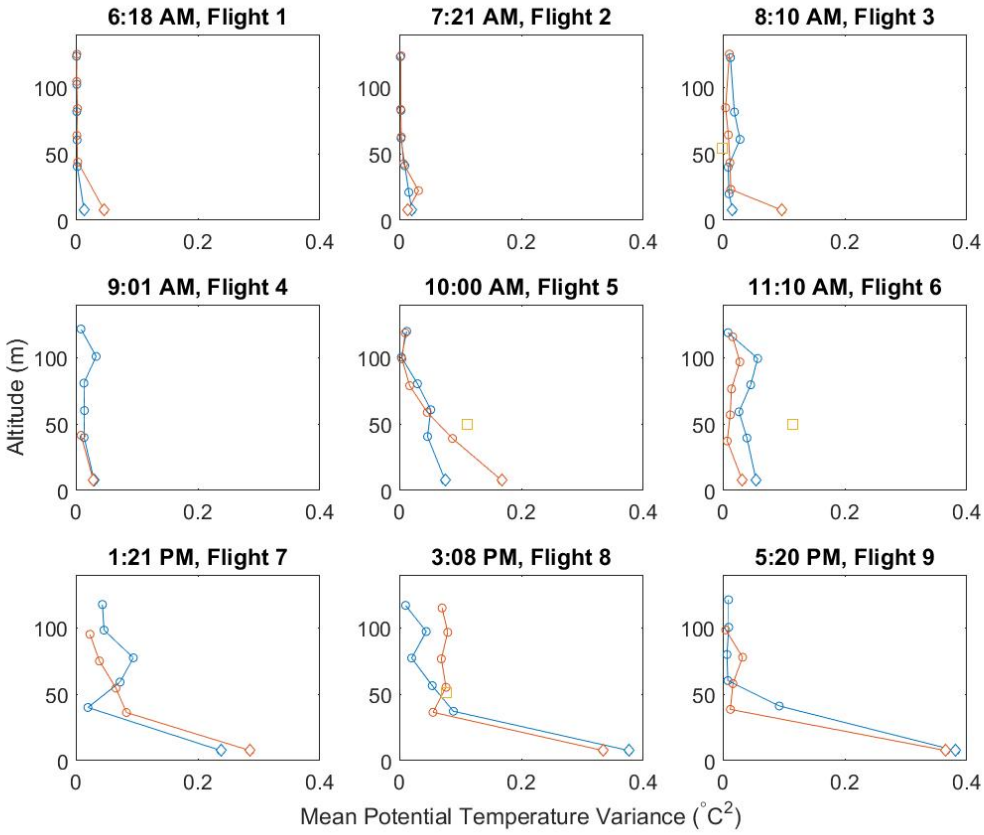

Figure 6.4: Mean potential temperature variance profiles for June 28, 2016 flights. Symbols as in table 6.1

The mean potential temperature variance is given by $\overline{\Theta'\Theta'}$ where $\Theta'(t) = \Theta(t) - \overline{\Theta}$ and the overline indicates a time average. The potential temperature variance profiles shown in figure 6.4 show a gradual increase in magnitude, once the stability conditions

transition to convective conditions, with higher magnitudes near the surface. The largest temperature variances appear to be measured by the sonic anemometer, this could be due to the value provided by the sonic anemometer being calculated for the entire flight duration, whereas the values at each flight level are from only a 2.5 minute sample. Temperature fluctuations with time scales longer than 2.5 minutes would not be captured by BC5A. In addition, the time response of the sensors on the aircraft and that provided by the sonic anemometer were different, resulting in different frequency content being included in the provided variances.

6.1.3 Humidity

Another parameter measured during these experiments by the UAVs was humidity, which describes the moisture content in the air. In this case relative humidity is being presented, defined as the percentage of water vapor in the air compared to the amount that the air could hold when saturated. A change in relative humidity throughout the diurnal cycle is expected as water evaporates from the surface during the daytime adding moisture to the air, and the changing temperature of the air changes its maximum moisture content. The results from the June 28 flights are displayed in the relative humidity profile shown in figure 6.5. The sonic anemometer was not equipped with a humidity sensor thus, the 7.6 meter altitude data point is not provided.

The important characteristic to observe in the humidity plots throughout the day are the slopes of the profiles more so than the magnitudes themselves. The magnitudes of the relative humidity are affected by temperature, which is changing throughout the day, leading to the lower magnitude % RH later in the afternoon. However, it can be seen that when the atmosphere was still stable (i.e. flights 1 and 2) the relative humidity decreased with height. As the day progressed, and water content from the surface began to evaporate and add moisture to the air, the relative humidity gradient

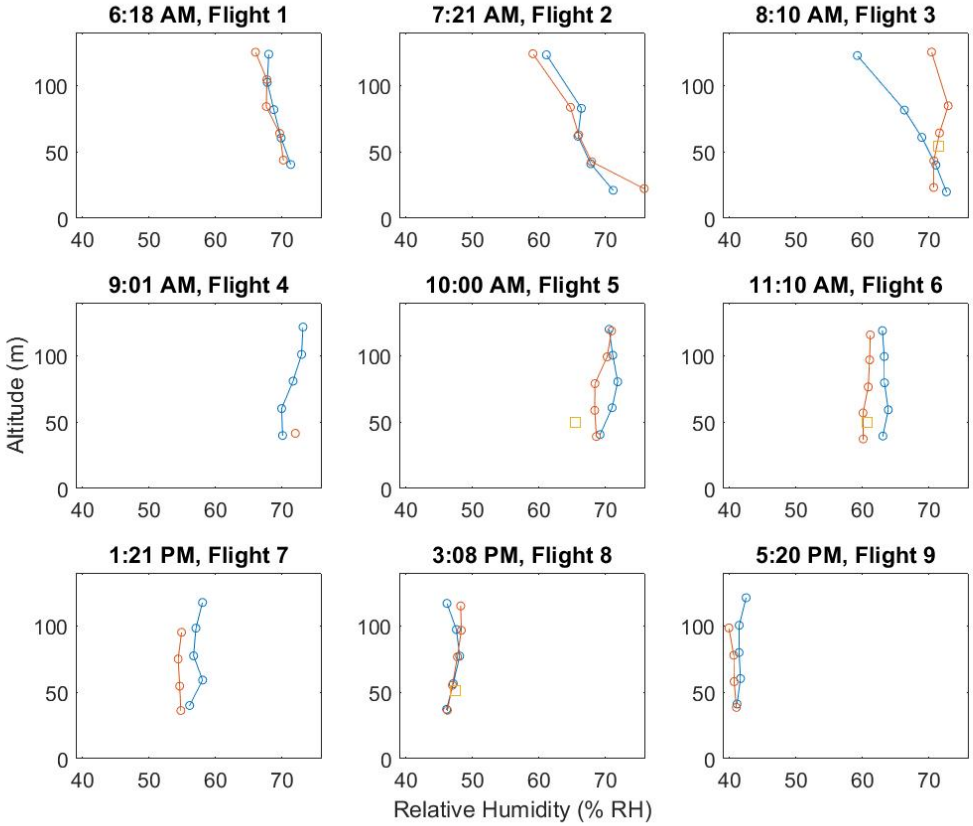

Figure 6.5: Mean relative humidity profiles for June 28, 2016 flights. Symbols as in table 6.1

evolved to become almost uniform as the boundary layer transitioned to the mixed convective state. Like the temperature measurements presented in Section 6.1.2, this change between ABL states seems to occur between the two profiles of flight 3, as reflected in changes in the gradient of the humidity profile.

6.1.4 Turbulence Properties

While five-hole probes are unable to measure the smallest scales of turbulence experienced in the atmospheric boundary layer, they are still able to capture most of the energy containing wavelengths. One quantity which characterizes the forcing the turbulence exerts on the flow field is the Reynold's stress tensor $\rho\overline{u_i' u_j'}$, often simplified to $\overline{u_i' u_j'}$ and i, j represent coordinates x, y, or z (East-West, North-South,

Up-Down). Here, u_i' represents the ith component wind velocity fluctuation. Because the time scales of the turbulence are longer than the 2.5 min time the UAV spends at a specific altitude, the Reynolds stress is not guaranteed to capture all of turbulence content. To accommodate the change in wind direction over the course of the flight, the turbulent kinetic energy per unit mass, k, is used here to quantify the turbulence intensity as a function of altitude. Note that the vertical wind component and its turbulence is a major product of the buoyancy force brought about by warming from the surface. Here, we present a slightly modified turbulent kinetic energy

$$k^* = \frac{1}{2}(\overline{u'^2} + \overline{v'^2}). \tag{6.2}$$

in order to investigate the properties of the z component of velocity, w, separately. The profiles of k^* are shown in figure 6.6 and the profiles of normal Reynolds stress in the z direction $\overline{w'^2}$ are shown in figure 6.7. The x-z component of the tensor $\overline{u'w'}$ is presented in 6.8 as it is connected to the turbulence production. The remaining components of the Reynolds stress tensor are provided in Appendix C.

Although it is unlikely that all energy content is captured by the statistics, it is apparent from these figures that the turbulent fluctuations in the atmosphere follow the trend of the diurnal cycle; they are approximately zero throughout the early morning periods of stability, and increase in magnitude once the convective conditions initiate. In the profiles of k^*, it can be seen that as the ABL transitions to a convective mixed boundary layer the ABL begins to show increasing turbulence content with increasing altitude. In the neutrally stable boundary layer, the turbulence production is driven by shear, resulting in the greatest turbulence content near the surface. During the late afternoon, early evening flights the mixed boundary layer has likely grown significantly large in respect to the maximum altitude at which the UAVs were acquiring data. Therefore the step changes in altitude above 50 meters may not

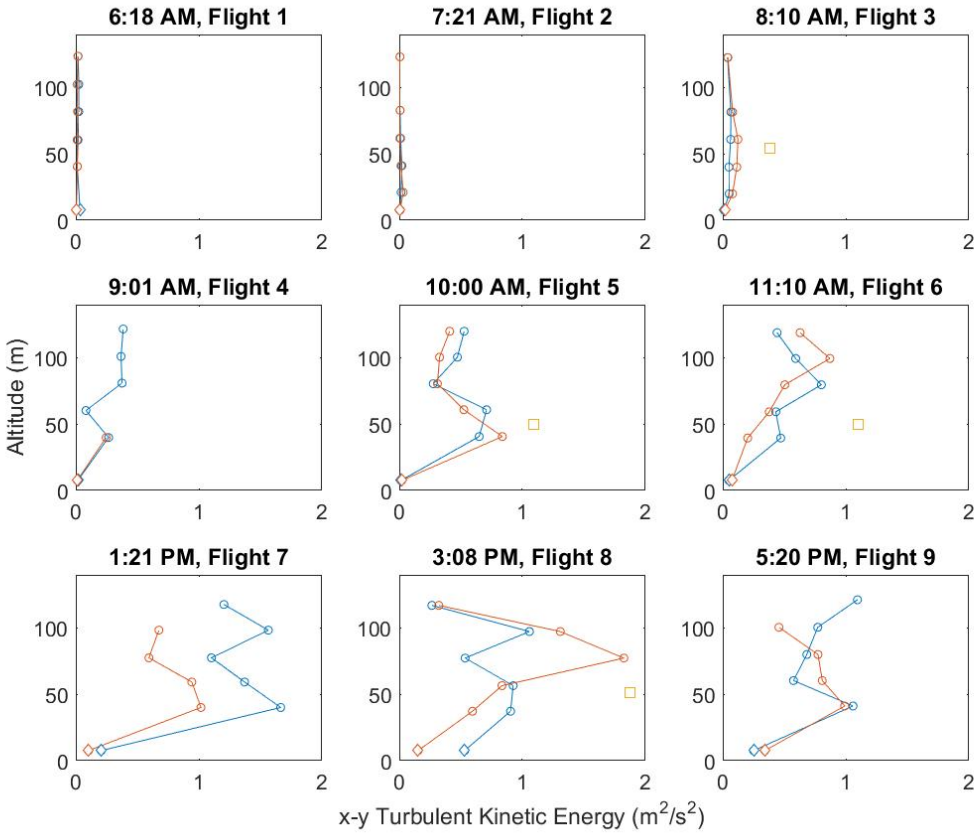

Figure 6.6: Profiles of k^* for June 28, 2016 flights. Symbols as in table 6.1

provide a significant enough altitude change to analyze the effects of altitude on the turbulent kinetic energy. ‘

Like the turbulent kinetic energy the $\overline{w'^2}$ and $\overline{u'w'}$ components of the Reynolds stress are shown to increase with altitude when the atmospheric boundary layer is in its mixed state.

Due to its ability to capture longer time scales, the straight line path BC5B turbulent data does not agree with the BC5A profile data and could be due in large part to BC5B covering much more area and over more diverse topographical features in comparison to BC5A. Interestingly, the calculations for the z component of Reynolds stress from BC5B seem to agree well with the profile data. Note that due to the proximity of the sonic anemometer to the surface, which constrains the velocity fluc-

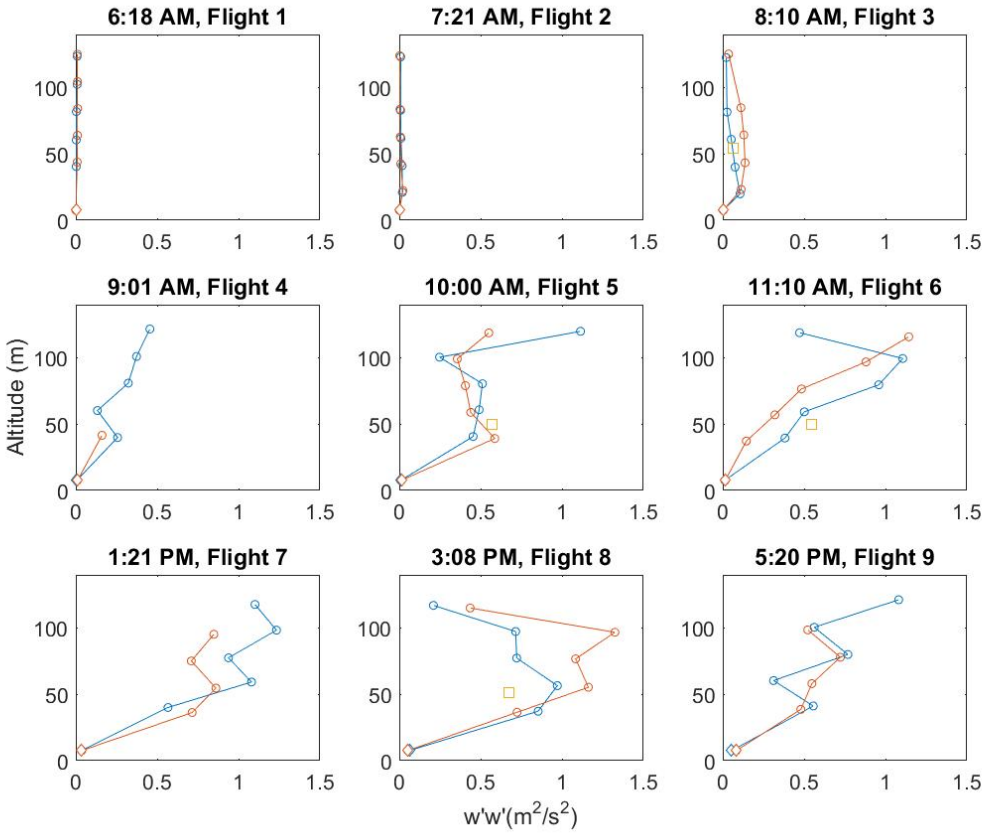

Figure 6.7: Profiles of $\overline{w'^2}$ component of Reynold stress tensor for June 28 flights. Symbols as in table 6.1

tuations, for all data displayed in this section the sonic anemometer data provides a consistent low altitude reference point for the turbulence fluctuations.

6.2 Wednesday, June 29, 2016

The objective of the test flights at the Marena Mesonet were focused on the use of two UAVs simultaneously flying concentric loiters at different radii. This technique allowed for the measurement of atmospheric properties at two altitudes within the same profile at the same time. With two altitudes being measured simultaneously, the impact of time evolution on the measured atmospheric properties can be further investigated.

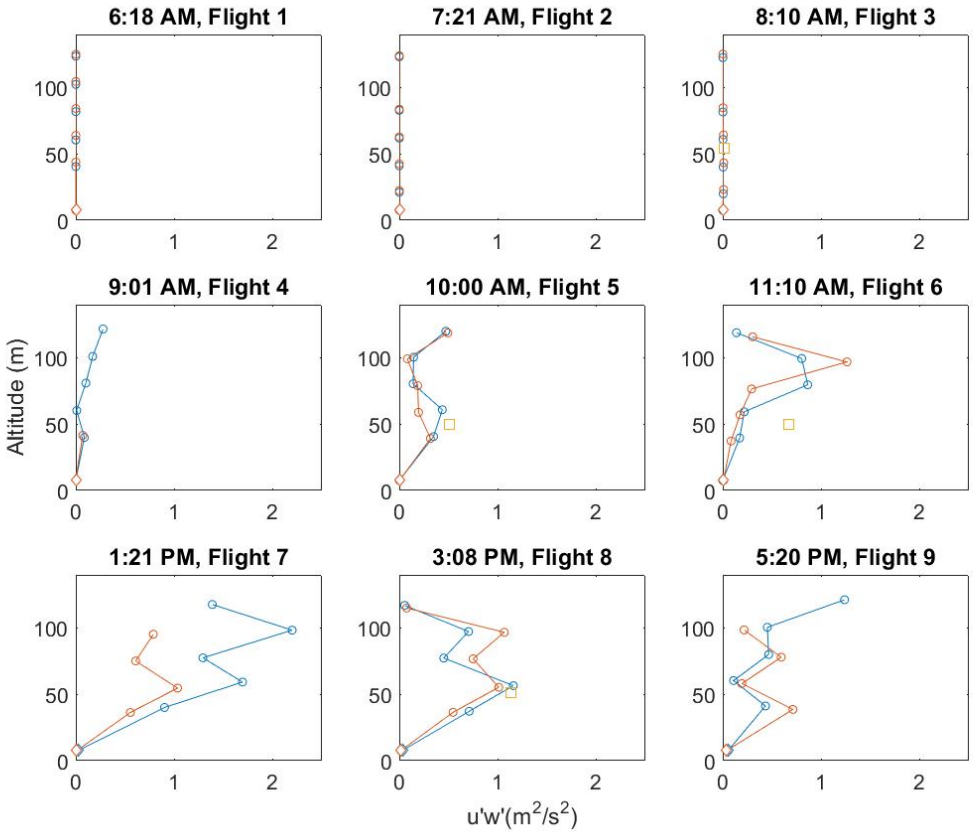

Figure 6.8: Profiles of $\overline{u'w'}$ component of Reynold stress tensor for June 28 flights. Symbols as in table 6.1

A total of three flights were conducted between 40 and 120 meters altitude, two of which were multi-UAV flights, as outlined in table 5.5. The flights took place from early morning to early afternoon with less emphasis on investigating the development of the atmospheric boundary layer and more emphasis on simultaneous profile measurements. The BC5A airframe began its 80 meter radius loiter flight trajectory at 40 meter altitude and increased altitudes at 20 meter steps until it reached 120 meters before stepping back down to its starting altitude. BC5B mirrored BC5A's profile pattern at a 100 meter loiter radius, beginning at 120 meters altitude and descending to 20 meters before ascending again up to 120 meters. For each profile the aircraft would loiter at 80 meter altitude simultaneously providing an excellent opportunity to compare data points at that position. The same atmospheric quantities presented

in the previous section were investigated for the Marena flight experiment. The symbols used to identify the acquisition platform used to provide the atmospheric data are outlined in table 6.2.

Table 6.2: Symbols for 6/29/2016 flight experiments

Symbol	Platform	Flight Pattern
○	BC5A	80 m radius Profile ↑↓
◇	Sonic Anemometer	7.6 meter altitude
○	BC5B	100 m radius Profile ↓↑

6.2.1 Mean Wind Speed and Direction

The three components of wind speed, $W(t)$ were measured for each flight at the Marena site. The profiles of mean wind velocity magnitude for both BC5A and BC5B are shown in figure 6.9 with the wind direction shown in figure 6.10. A boundary layer having increasing velocity with altitude can clearly be observed in the profiles throughout the day, most predominately shown in the first flight of the day at 7:41 AM which also provides the largest average velocity value measured during the experiments. The wind directions from the Marena site were much more consistent throughout the day when compared to the measurements from June 28, in which the wind direction significantly shifted over the course of the day. The latter two flights were made with two UAVs flying simultaneously. The agreement of the measurements of both wind speed and direction between the two appears to be reasonable, particularly when the UAVs were simultaneously at similar altitudes (i.e. 60m, 80m, and 100m). The maximum and minimum altitudes in which the data from the UAVs differ the most experience a larger time gap between the measurements and thus wind velocity deviations over time can be seen. The trend-lines from the sonic anemometer agree extremely well for all flights for both mean wind speed and wind direction.

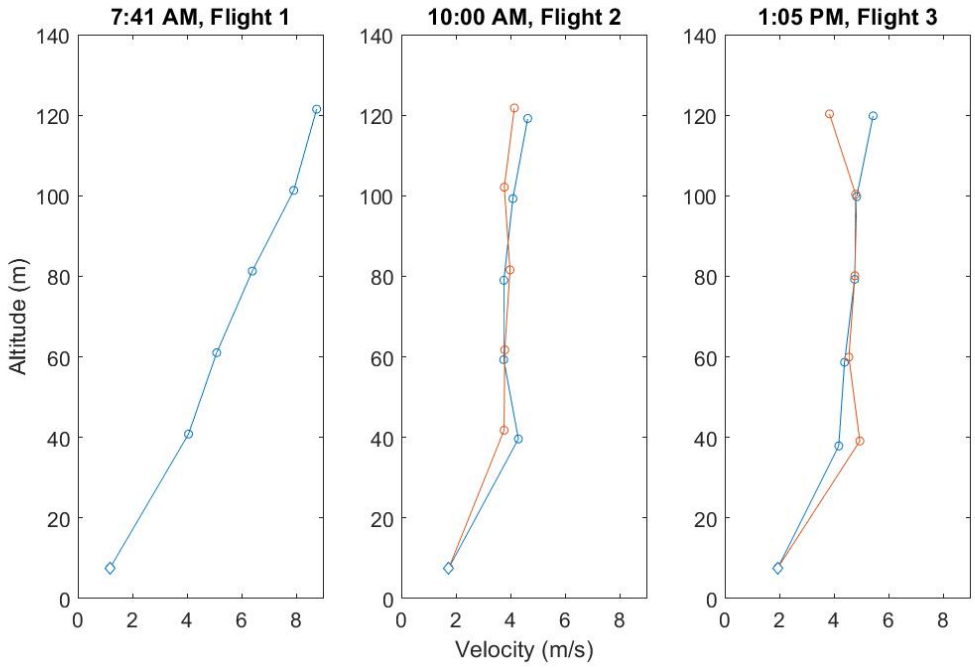

Figure 6.9: Mean wind velocity magnitude profiles measured on June 29, 2016. Symbols as in table 6.2

6.2.2 Potential Temperature and Humidity

The profiles of mean and variance of potential temperature measured by BC5A and BC5B are shown in figures 6.11 and 6.12 respectively. The potential temperature progression follows a pattern similar to the June 28 flight experiments in that the early morning flight shows increasing potential temperature with altitude indicating a stable boundary layer and flights two and three show decreasing potential temperature with altitude demonstrating that the ABL is no longer stable and has shifted to a convective mixed boundary layer. The potential temperature variance from all flights follows expected trends, increasing in magnitude with decreasing stability. The disagreement in potential temperature variance between the two UAVs is likely caused by the relatively slow response time of the iMet temperature sensor. This in addition to the short loiter time of 2.5 minutes per altitude of the aircrafts introduces error in the variance readings. The relative humidity profile measurements are displayed

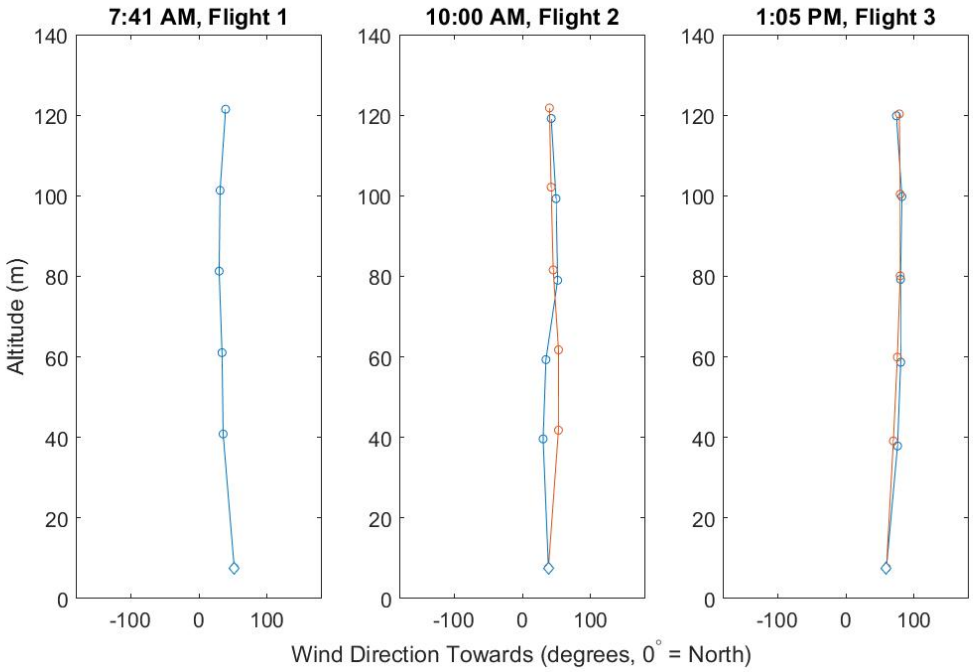

Figure 6.10: Mean wind direction profiles measured on June 29, 2016. Symbols as in table 6.2

in figure 6.13. Again the data follows similar trends experienced at the UAFS. The relative humidity initially decreases with altitude in the early morning and becomes more uniform as the day progresses indicating that water vapor is being transported from the ground to the atmosphere. The potential temperature and humidity data measured between each UAV agree exceptionally well with one another at all altitudes for each flight. The agreements between the two systems for wind speed, direction, potential temperature, and humidity help to validate the instrumentation system and data reduction scheme that has been developed.

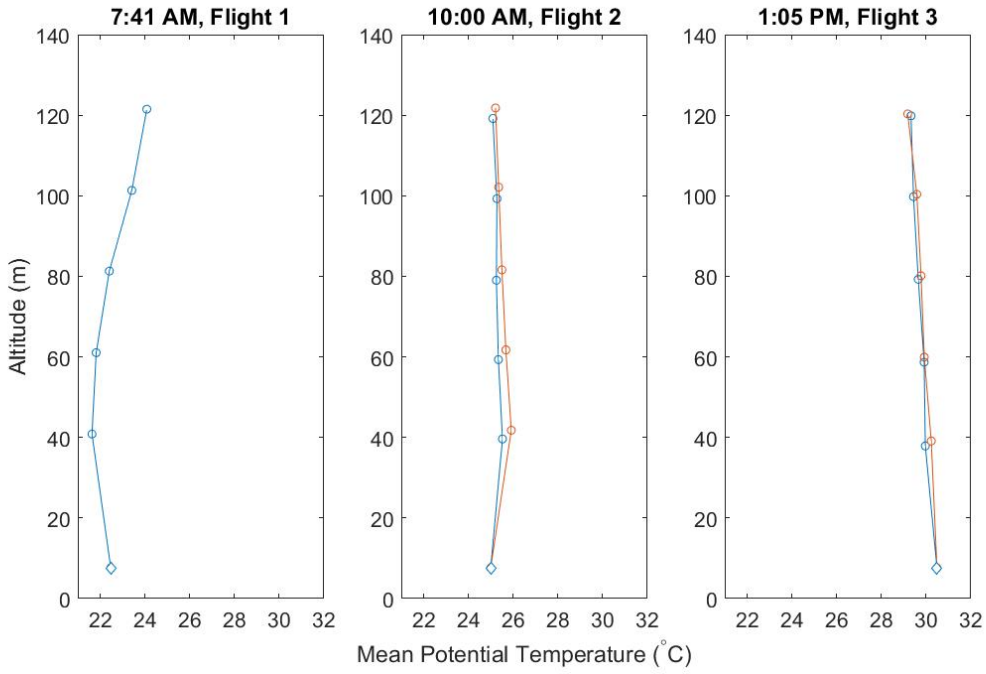

Figure 6.11: Mean potential temperature profiles measured on June 29, 2016. Symbols as in table 6.2

6.2.3 Turbulence Properties

The profiles of k^* and select components of the Reynolds stress tensor are provided in figures 6.14-6.16. The k^* results follow expected trends as the magnitude of the turbulent energy increased with altitude as well as increasing throughout the day. The same can be observed of the components of the Reynolds stress tensor. As can be seen in figure 6.14, flight 2 shows excellent agreement between each UAV while flight 3 demonstrates great agreement when the UAVs are simultaneously loitering at the same or similar altitudes. However, while BC5A (blue) is at its maximum altitude of 120 meters, BC5B (red) is at the minimum altitude of the profile at 20 meters. At these points each UAV measures the maximum turbulent kinetic energy experienced during the test flight. It would appear that a large gust came through at the halfway point of the experiment causing these maximums to be recorded and thus altering the profile from a consistent trend.

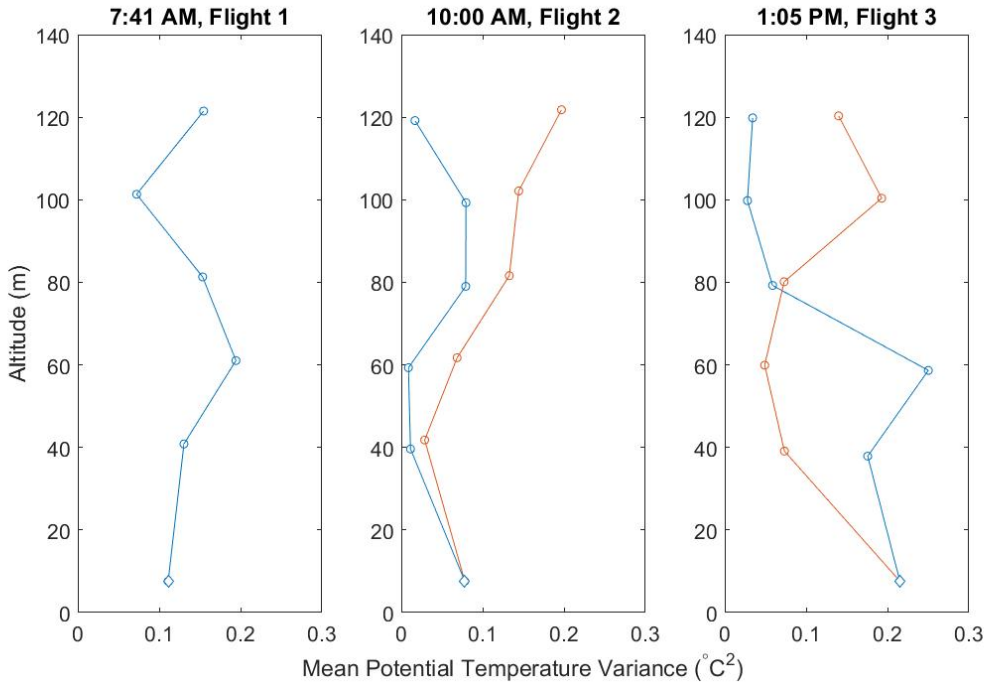

Figure 6.12: Profiles of the variance of potential temperature measured on June 29, 2016. Symbols as in table 6.2

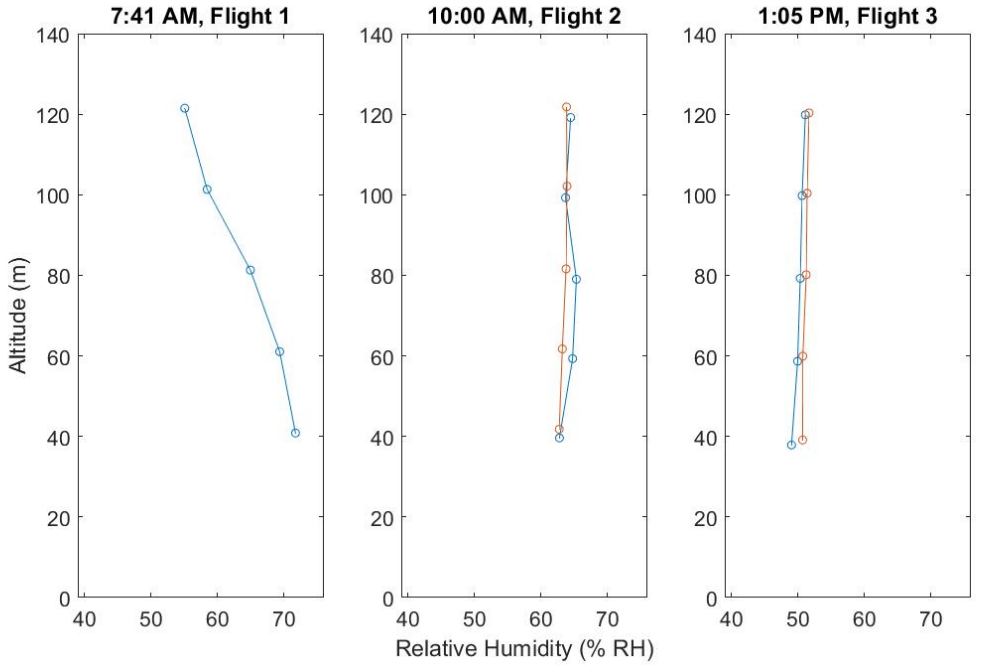

Figure 6.13: Mean relative humidity profiles for June 29, 2016 flights. Symbols as in table 6.2

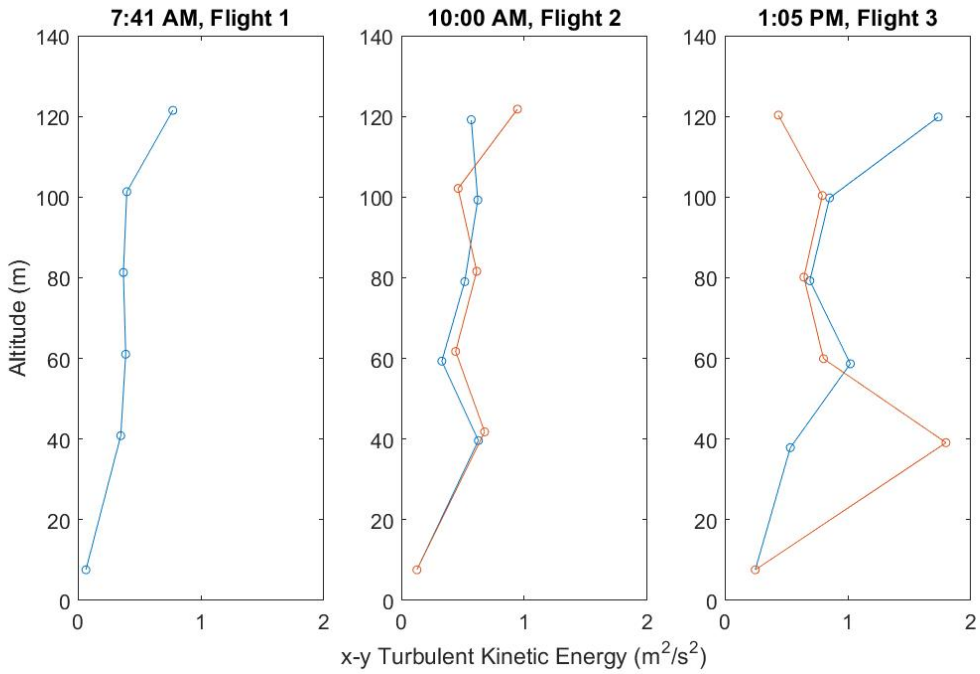

Figure 6.14: Profiles of k^* measured on June 29, 2016. Symbols as in table 6.2

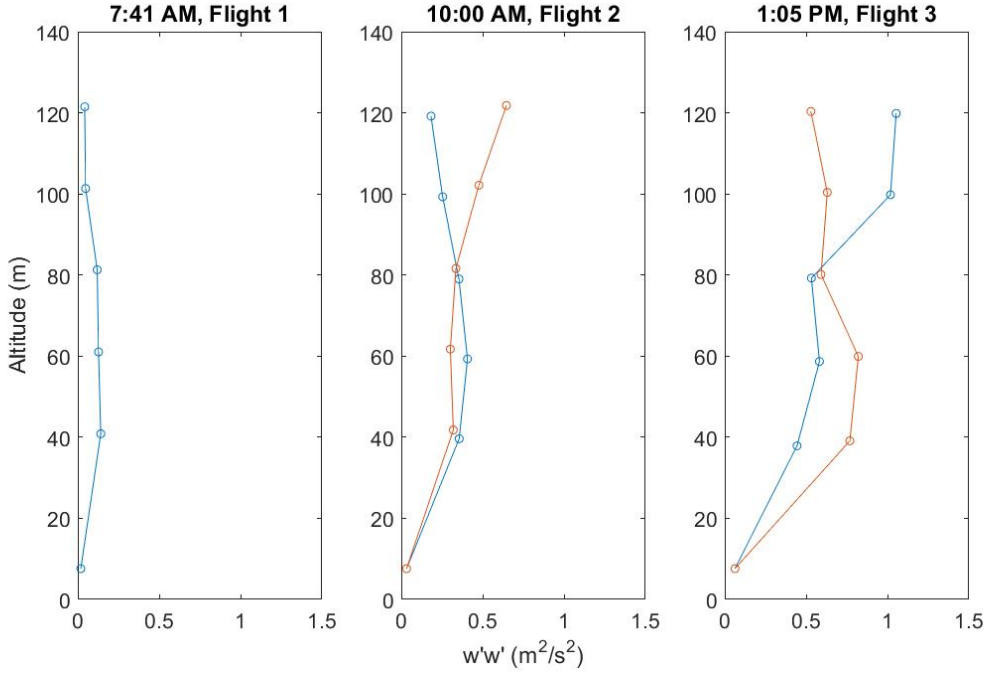

Figure 6.15: Profiles of $\overline{w'^2}$ measured on June 29, 2016. Symbols as in table 6.2

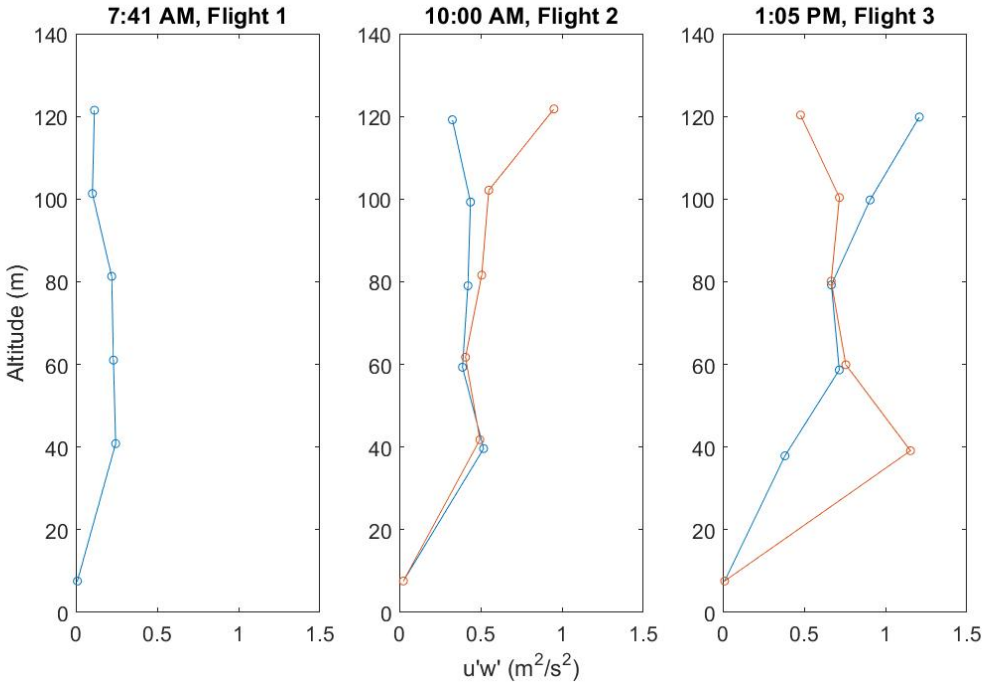

Figure 6.16: Profiles of $\overline{u'w'}$ measured on June 29, 2016. Symbols as in table 6.2

Chapter 7 Conclusions and Future Work

An unmanned aerial vehicle capable of conducting atmospheric boundary layer turbulence research was developed. This tool to conduct atmospheric research can alleviate many shortcomings of existing measurement techniques, such as tower-based point measurements, balloon launches and high flying, manned aircraft. After multiple previous versions of aircraft produced, the aircraft deemed BLUECAT5 was tested and two were flown throughout the days of the 28th and 29th of June, 2016 in Stillwater, Oklahoma. The experiments were conducted with a five-hole multi-hole pressure probe turbulence instrumentation package capable of capturing the majority of energy-containing wavelengths within the atmospheric boundary layer. The complex instrumentation package developed for these experiments includes the five-hole probe, Pitot-static tube, Pixhawk autopilot, VectorNav VN-300 INS, and iMet-XQ sensor. To be able to investigate data recorded by a highly dynamic airborne platform, a data reduction scheme was developed.

The data sets provided from the experiments conducted at Oklahoma demonstrate the ability to use fixed-winged unmanned aerial vehicles to profile the atmospheric boundary layer. The profiles for mean wind speed and direction, temperature, and humidity all follow expected boundary layer behavior throughout a typical diurnal cycle for both days. A sonic anemometer provided a low altitude data point, as well as a reference point for verification of the aircraft-produced measurements. The data from the sonic anemometer was consistent with the measurements from the unmanned aerial vehicles. The turbulence properties measured by the unmanned aerial vehicles

also show reasonable results, although the effects of the measurement path, particularly the relatively short acquisition time of 2.5 minutes per altitude level needs to be investigated further. The ability to fly two unmanned aerial vehicles simultaneously to obtain multi-point measurement was also demonstrated. The agreement between the measurements made by the two aircraft proved to be acceptable for both days of flights. The straight line paths flown by one aircraft on day one agreed well with the profile data measured by the other aircraft throughout the day. On day two, simultaneous flights of profile patterns were conducted in order to provide simultaneous measurements at multiple altitudes. The data from these flights again showed excellent agreement between the two aircraft, particularly when measuring at similar altitudes.

With the successful tests of BLUECAT5, further developments and studies can be taken to improve the abilities of the system and the results measured by the aircraft. The calibration used for the five-hole probes in these experiments required removing the probe from the aircraft to mount inside the wind tunnel, which consequently removes any disturbances that may be caused by the airframe and picked up during flight experiments. Ideally this calibration would include the aircraft being mounted inside of the wind tunnel, but the facilities and the University of Kentucky did not allow for this approach. In addition, the mounting of the sensors through the nose of the aircraft leave much room for variability and introducing direction alignment as they can vary each time the instrument is re-mounted. This can be alleviated by standardizing the mounting procedure as well as developing a secondary calibration method that utilizes a test flight to calculate the offsets in both angle of attack and sideslip angle.

There is endless potential in the types of experiments that can be conducted with unmanned aerial vehicles but some investigation is still required to determine the optimal flight path to obtain the best statistics. It is desired to increase the length of

the straight line paths flown to allow for the measurement of even larger scales of turbulent motions that are currently being seen. Also, the profile-measuring flight paths need to be developed further in order to optimize statistical convergence and altitude density. Additionally, with the groundwork completed for BLUECAT3 and BLUECAT4, and the feasibility of using hot-wire anemometers for atmospheric boundary layer turbulence research, these systems can be combined with the knowledge gained by the work of BLUECAT5. This would allow for a much greater response time in the turbulence sensors leading to the capture of the smallest scales of turbulence experienced in the atmospheric boundary layer allowing the measurement of turbulence dissipation properties.

Appendices

A Five-hole Probe Calibration

The five-hole probe calibration rig was designed to be implemented into the University of Kentucky's 0.3 $\times$0.3 meter wind tunnel. As mentioned in this thesis a series of α and β angles are applied and five pressures are measured. The calibration rig executes the necessary pitching and yawing of the probe and consists of two stepping motors, an 90° bent aluminum bracket, a bent steel rod and a 3D printed clamp for housing the probe. The photos in figures 1, 2, and 3 demonstrate the wind tunnel set up with the Vexta stepping motors, the five-hole probe, and the fixed pitot-static probe. Figure 1 shows the entire calibration rig installed into the wind tunnel during a calibration run. It can be seen that two pieces of extruded aluminum and a long piece ABS plastic were mounted to the top of the wind tunnel in order to secure the stepping motors in place. The cylindrical steel rod was extended through the middle of the second stepper motor inside the wind tunnel and fixed to the 3-D printed clamp that housed the probe. The top section of the rig can be viewed more closely in figure 2. Inside the wind tunnel the five-hole probe was installed. It should be noted that the steel rod was bent so that the tip of the probe could be placed along the axis of yaw rotation to allow the probe to remain along the central axis of the wind tunnel. The stationary pitot-static tube was also mounted inside the wind tunnel to provide a constant reference measurement as well as provide a static pressure line for the five-hole probe transducers. each port of the five-hole and pitot-static probe were routed to mpxv7002 differential pressure transducers via 1.75 mm Tygon tubing

through the top of the wind tunnel. The internal of the wind tunnel can be seen in figure 3.

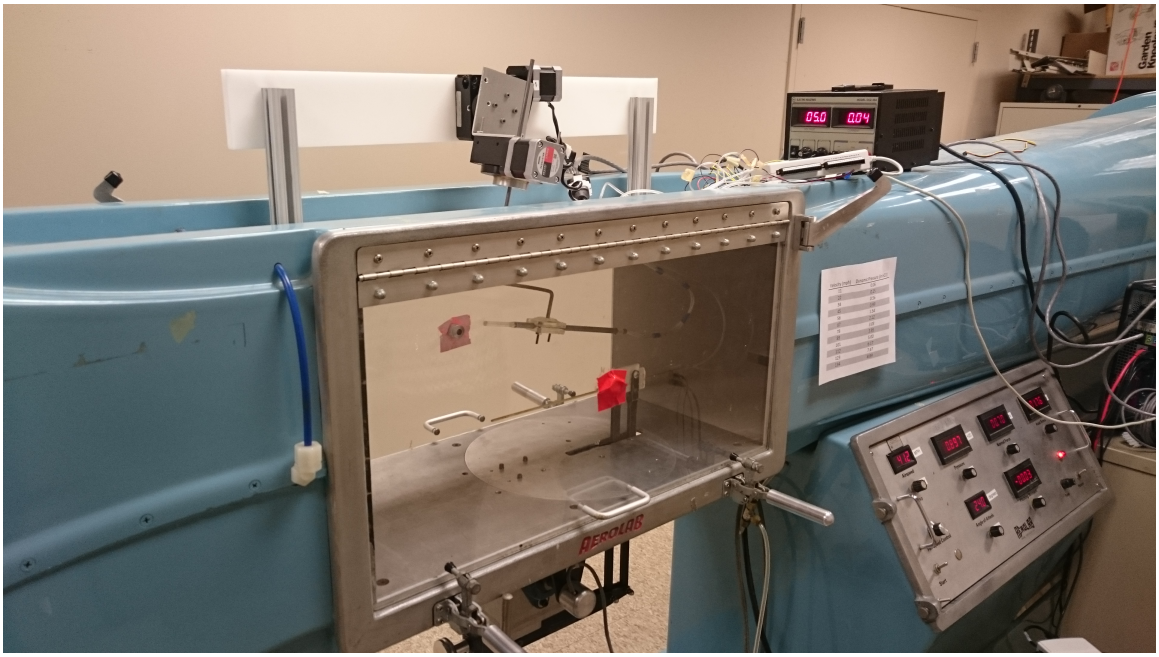

Figure 1: Overview of calibration rig setup

The calibration procedure is performed using a preexisting LABVIEW program. The program controls the motion of the stepping motors and acquires the current voltage measured by the sensors. Before beginning the calibration a zero velocity reference needs to be acquired by running the program at a single (0,0) point as the wind tunnel is off. The program will run through a series of angles determined by a .txt file created by the user and save the mean voltages as a .txt file for each input being required over the time designated in the program.

After the calibration is complete the coefficients are calculated using a Matlab code as explained in Chapter 5. Attention is given to removing any offset imposed by user error in alignment when installing the probe. This is completed by fitting a surface on the pressure values from the central hole and calculating the maximum of that surface as demonstrated in figure 4. An example of the results from a calibration are displayed in Chapter 5.

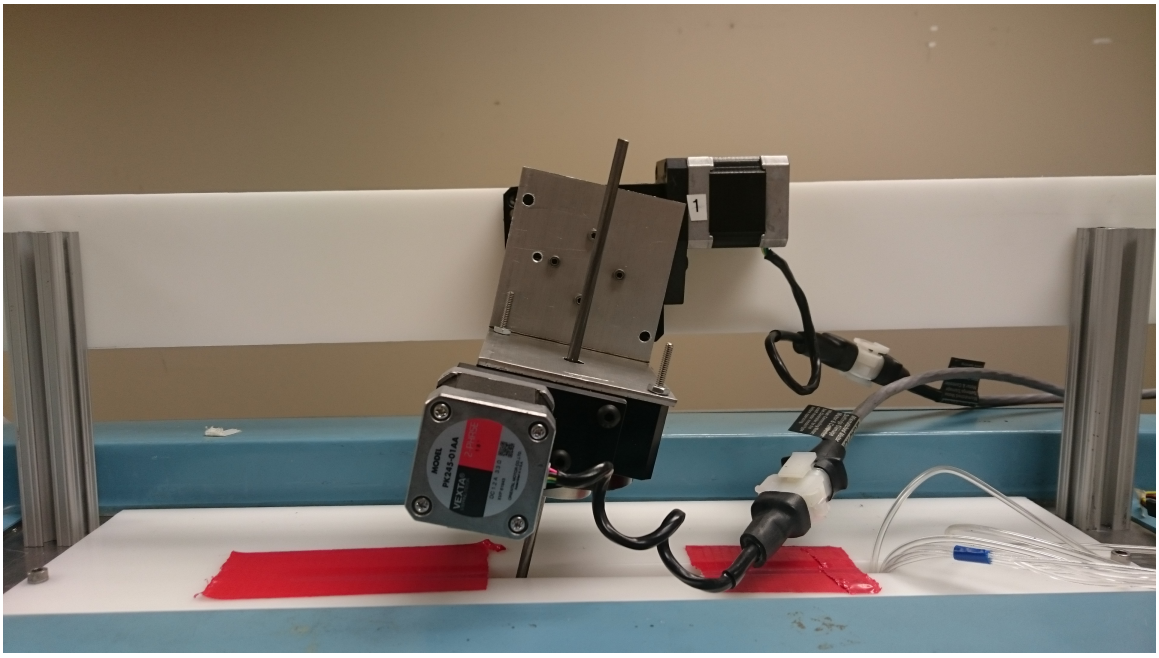

Figure 2: Top of wind tunnel mounting and setup.

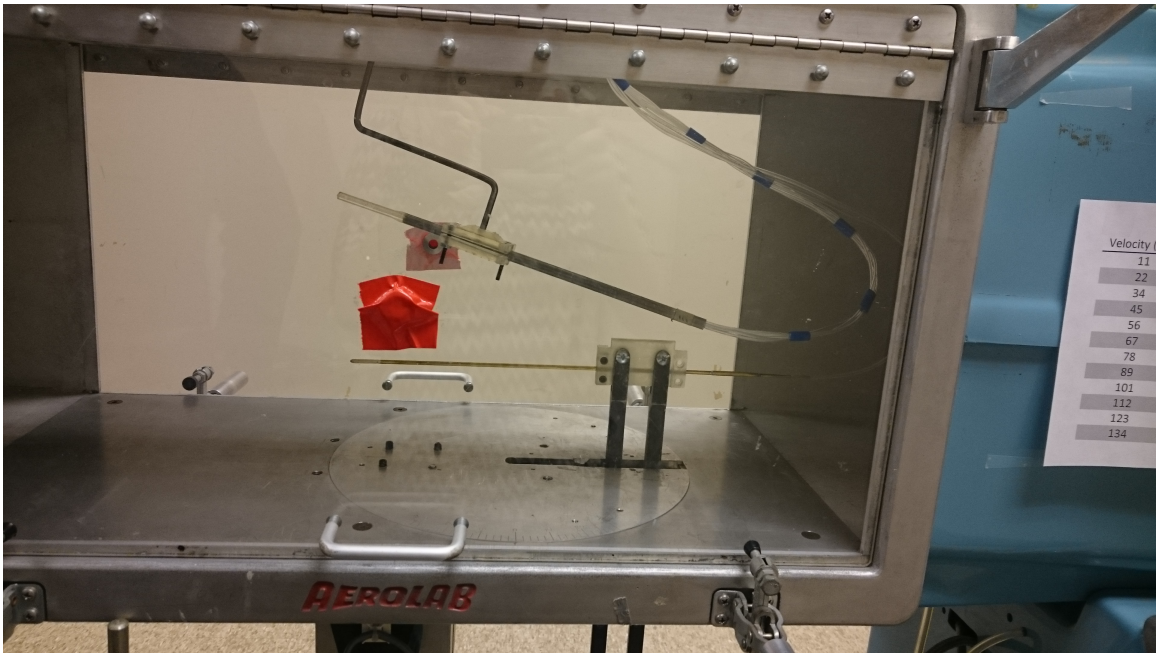

Figure 3: Internal wind tunnel setup.

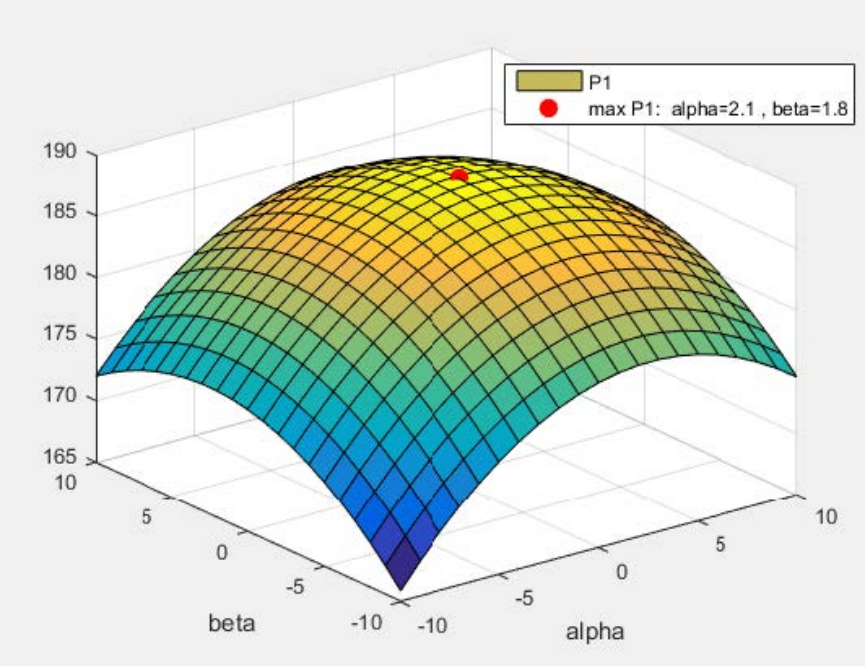

Figure 4: Angular offset calculation. In this case, the offset for α is 2.1° and the offset for β is 1.8°

B Instrumentation Measurement Procedure Checklist

☐ PREFLIGHT

- ☐ Power on Kangaroo (Username: ukyuav Password: ukyuav11)
- ☐ Connect HDMI, bluetooth keyboard, and bluetooth mouse to Kangaroo
- ☐ Connect DAQ to Kangaroo via USB
- ☐ Connect 5V power supply from DAQ to transducer board
- ☐ Start DAQami to ensure each transducer is reading 2.5 volts
- ☐ Connect VectorNav VN-300 to Kangaroo via USB
  Note: BC5A receives external power from servo rail on Pixhawk
- ☐ Start VectorNav software and connect to the VN-300
- ☐ Verify/set DAQ parameters in GetData txt file
- ☐ Initiate GetData program to begin acquisition of five-hole probe transducers
  Note: Ensure red tags on probes for first 20 seconds for zero readings
- ☐ Once the green light on the DAQ begins flashing (∼45 seconds)
  begin VectorNav acquisition via software
- ☐ Disconnect HDMI and charger from Kangaroo
- ☐ Begin iMet acquistion via button on sensor

☐ POSTFLIGHT

- ☐ Connect HDMI and charger to Kangaroo
- ☐ Stop VectorNav recording via software
- ☐ Disconnect VN-300 in software and unplug USB from Kangaroo
- ☐ If GetData program is still running, kill process in task manager
- ☐ Disconnect DAQ USB from Kangaroo
- ☐ Remove/Replace Kangaroo with fully charged unit for data transfer and cooling
- ☐ Transfer DAQ data from GetData folder (data.daq) to external storage
- ☐ Convert data of VN-300 within VectorNav software (right click - export data)
- ☐ Transfer VN-300 data to external storage
- ☐ Stop acquistion of iMet and transfer sensor data
- ☐ Remove micro-SD from Pixhawk and transfer data log to external storage
  Note: this file is converted to matlab file via mission planner
- ☐ Ensure all data is stored in same folder and named correctly
- ☐ Execute post processing to check that data is good

C Reynolds Stress Tensor

The remaining components of the Reynold's stress tensor not presented in Chapter 6 are provided.

C.1 Tuesday, June 28, 2016

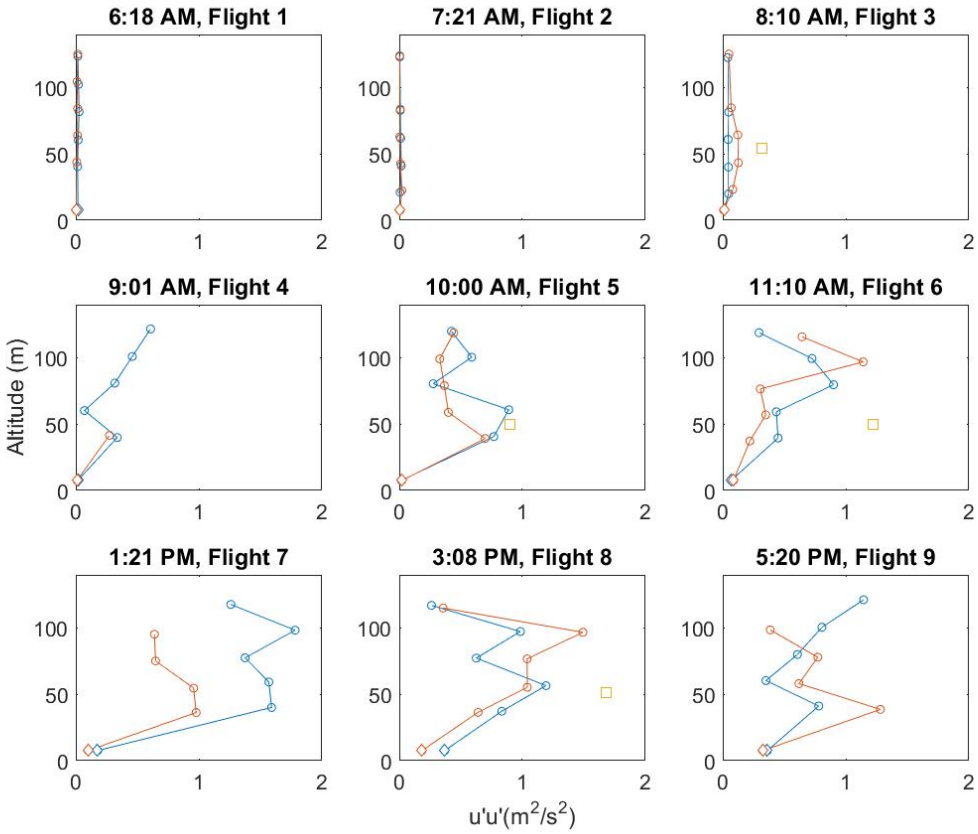

Figure 5: Profiles of $\overline{u'^2}$ measured on June 28, 2016. Symbols as in table 6.1

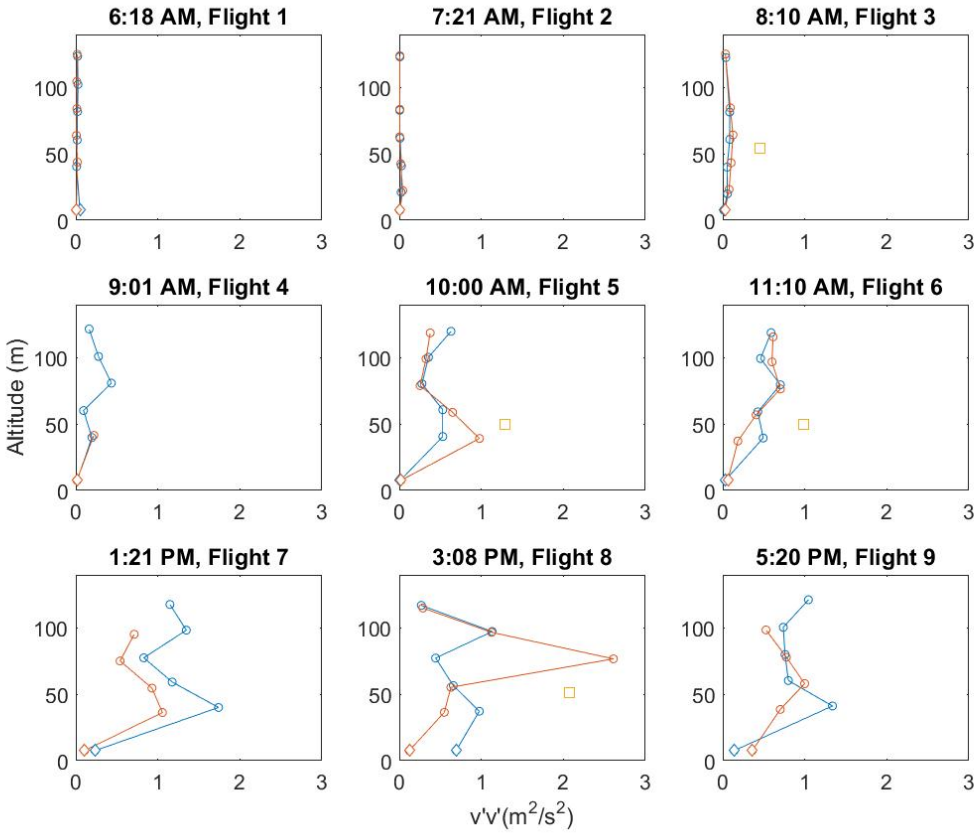

Figure 6: Profiles of $\overline{v'^2}$ measured on June 28, 2016. Symbols as in table 6.1

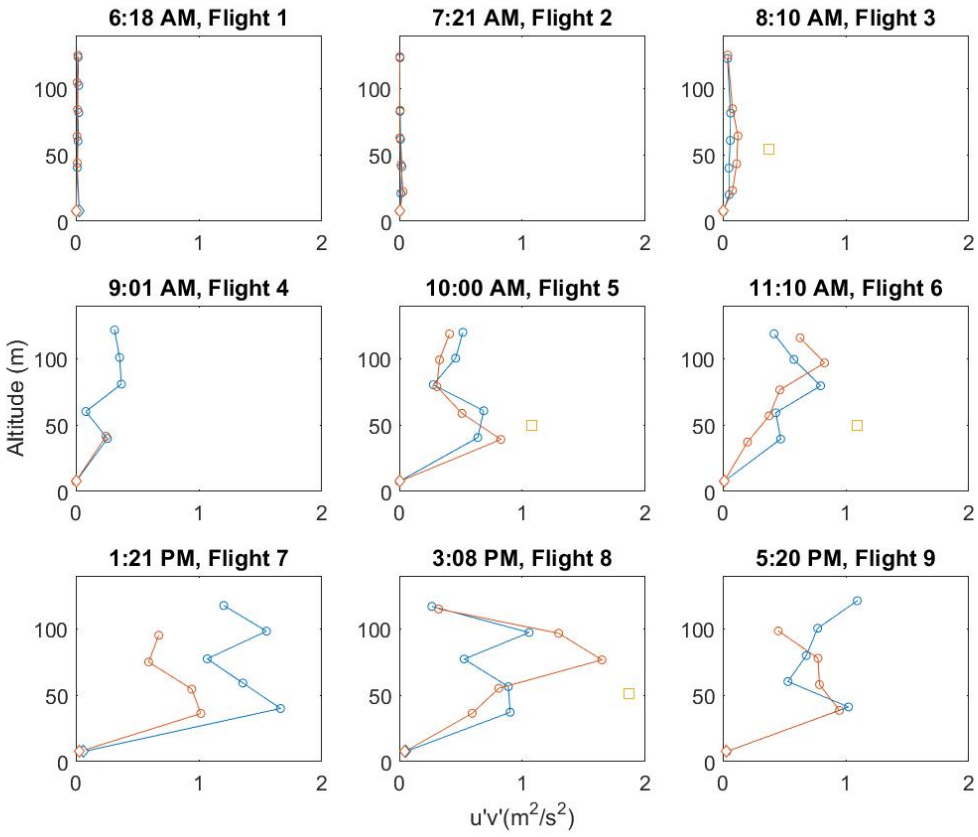

Figure 7: Profiles of $\overline{u'v'}$ measured on June 28, 2016. Symbols as in table 6.1

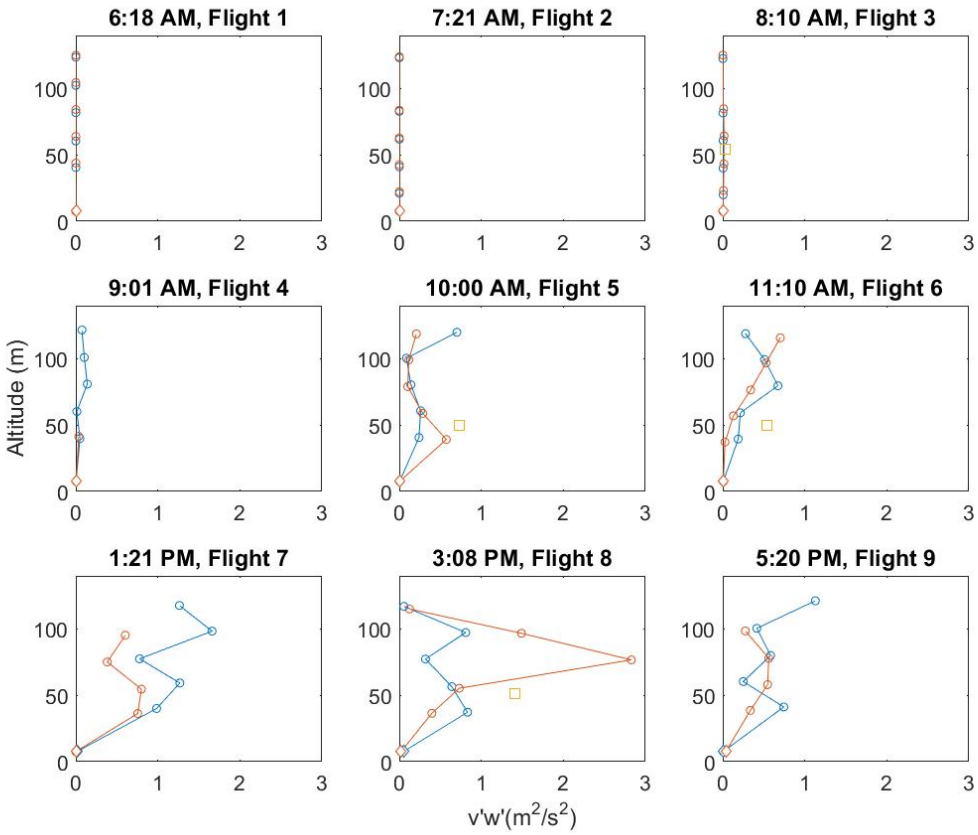

Figure 8: Profiles of $\overline{v'w'}$ measured on June 28, 2016. Symbols as in table 6.1

C.2 Wednesday, June 29, 2016

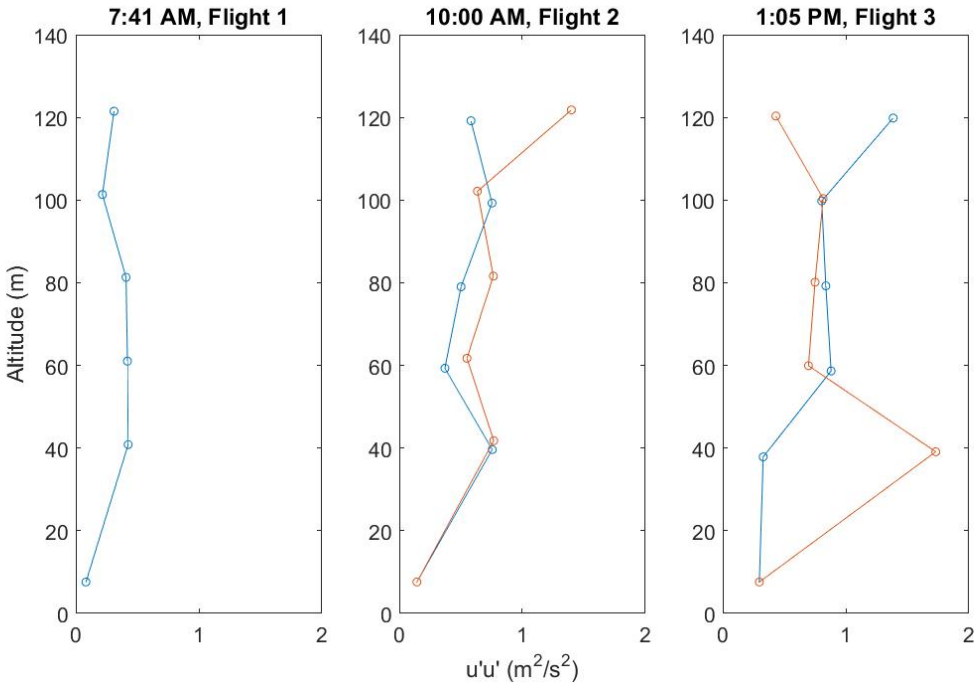

Figure 9: Profiles of $\overline{u'^2}$ measured on June 29, 2016. Symbols as in table 6.2

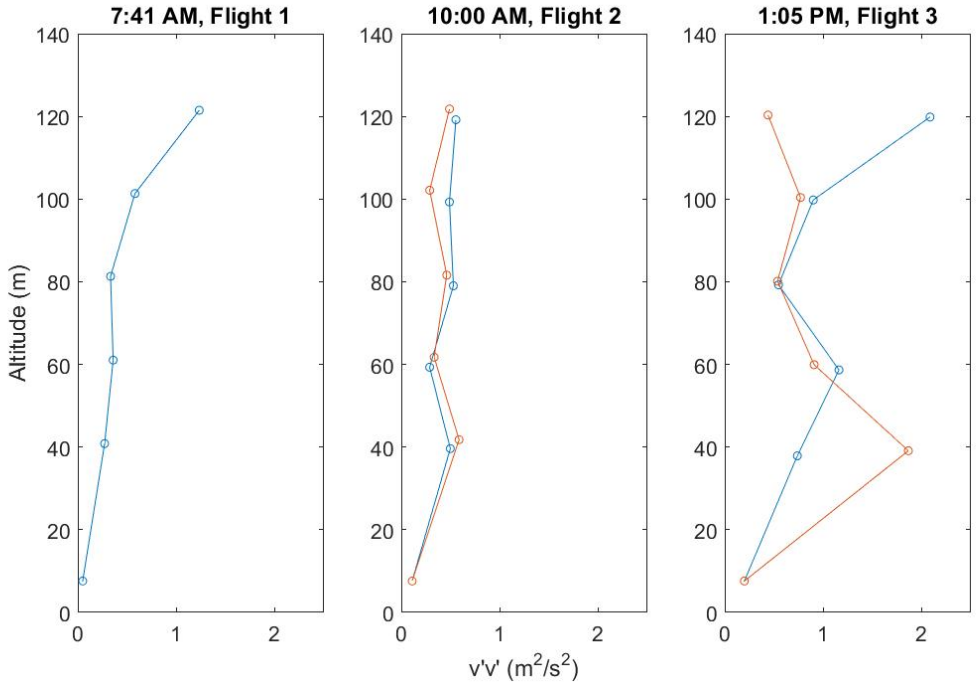

Figure 10: Profiles of $\overline{v'^2}$ measured on June 29, 2016. Symbols as in table 6.2

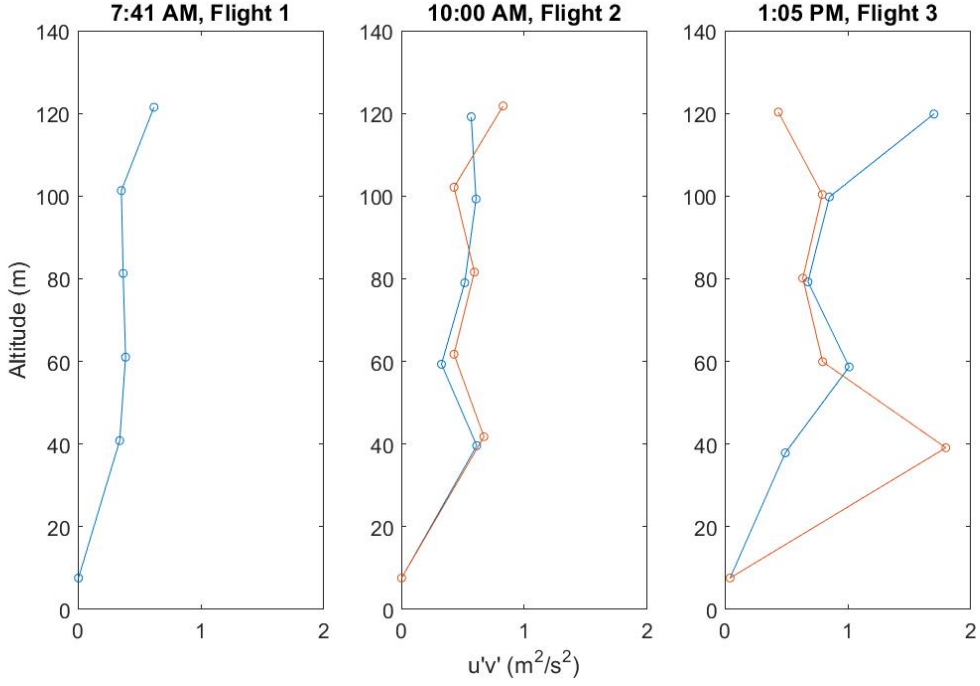

Figure 11: Profiles of $\overline{u'v'}$ measured on June 29, 2016. Symbols as in table 6.2

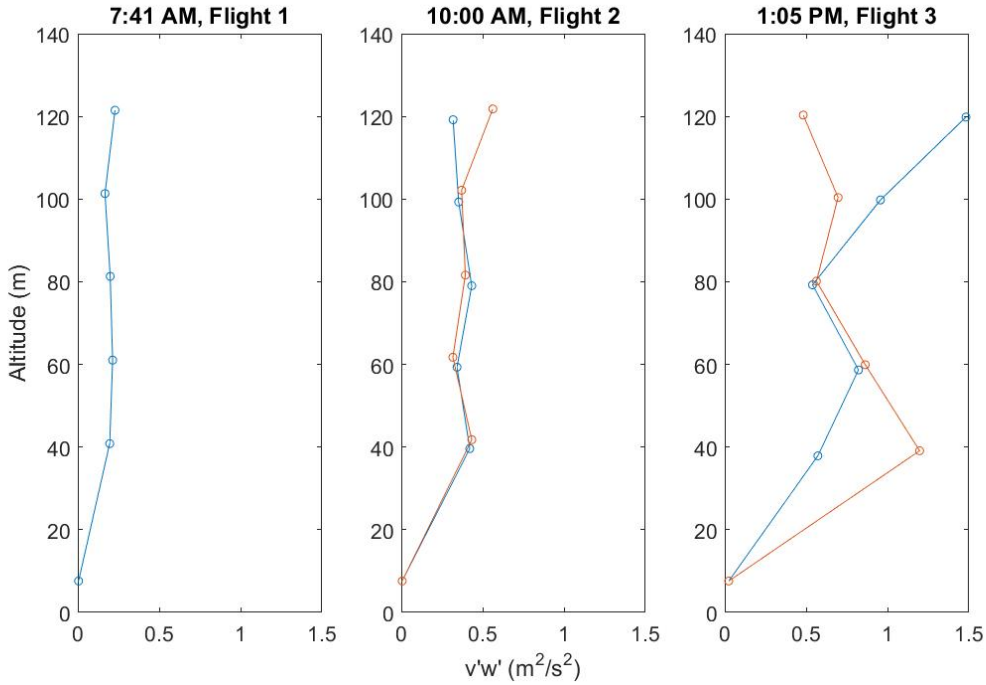

Figure 12: Profiles of $\overline{v'w'}$ measured on June 29, 2016. Symbols as in table 6.2

Bibliography

[1] S. B. Pope. *Turbulent Flows*. Cambridge University Press, 2000.

[2] R.B. Stull. *An Introduction to Boundary Layer Meteorology*. Springer, 1988.

[3] Jamal Saleh. *Fluid Flow Handbook*. McGraw-Hill, 2002.

[4] Alexander J. Smits and Ivan Marusic. Wall-bounded turbulence. *Physics Today*, 66(9):25–30, 2013.

[5] Alan Folz and James M. Wallace. Near-surface turbulence in the atmospheric boundary layer. *Physica D: Nonlinear Phenomena*, 239(14):1305 – 1317, 2010.

[6] P. K. Kundu, I. M. Cohen, and D. R. Dowling. *Fluid Mechanics, Fifth Edition*. Elsevier, 2011.

[7] P. Bradshaw and G. P. Huang. The law of the wall in turbulent flow. *Proc. R. Soc. Lond. A*, 451:165–188, 1995.

[8] G. I. Taylor. The spectrum of turbulence. *Proc. R. Soc. Lond.*, 164(919):476–490, 1938.

[9] C.W. Higgins, M. Froidevaux, V. Simeonov, N. Vercauteren, C. Barry, and M.B. Parlange. The effect of scale on the applicability of taylor's frozen turbulence hypothesis in the atmospheric boundary layer. *Boundary-Layer Meteorol.*, 143:379–391, 2012.

[10] John Anderson Jr. Ludwig prandtl's boundary layer. *Physics Today*, 58(12):42–48, 2005.

[11] Bruce R. Munson, Donald F. Young, Theodore H. Okiishi, and Wade W. Huebsch. *Fundamentals of Fluid Mechanics, 6th Edition*. Wiley, 2009.

[12] Cameron Tropea, Alexander L Yarin, and John F Foss. *Springer handbook of experimental fluid mechanics*, volume 1. Springer Science & Business Media, 2007.

[13] Mitsuaki Horiguchi, Taiichi Hayashi, Hiroyuki Hashiguchi, Yoshiki Ito, and Hiromasa Ueda. Observations of coherent turbulence structures in the near-neutral atmospheric boundary layer. *Boundary-Layer Meteorology*, 136(1):25–44, 2010.

[14] R. M. Williams and C. A. Paulson. Microscale temperature and velocity spectra in the atmospheric boundary layer. *Journal of Fluid Mechanics*, 83:547–567, 12 1977.

[15] GARY J. KUNKEL and IVAN MARUSIC. Study of the near-wall-turbulent region of the high-reynolds-number boundary layer using an atmospheric flow. *Journal of Fluid Mechanics*, 548:375–402, 2 2006.

[16] A. B. Folz. *An experimental study of the near-surface turbulence in the atmospheric boundary layer*. PhD thesis, UNIVERSITY OF MARYLAND COLLEGE PARK, December 1997.

[17] C. M. Sheih, H. Tennekes, and J. L. Lumley. Airborne hot-wire measurements of the small-scale structure of atmospheric turbulence. *Physics of Fluids*, 14(2):201–215, 1971.

[18] Donald H. Lenschow and Warren B. Johnson Jr. Concurrent airplane and balloon measurements of atmospheric boundary-layer structure over a forest. *Journal of Applied Meteorology*, 7(1):79–89, 1968.

[19] E. N. Brown, C. A. Friehe, and D. H. Lenschow. The use of pressure fluctuations on the nose of an aircraft for measuring air motion. *Journal of Climate and Applied Meteorology*, 22(1):171–180, 1983.

[20] Wayne M. Angevine, S. K. Avery, and G. L. Kok. Virtual heat flux measurements from a boundary-layer profiler-rass compared to aircraft measurements. *Journal of Applied Meteorology*, 32(12):1901–1907, 1993.

[21] C Russell Philbrick. Raman lidar descriptions of lower atmosphere processes. *Lidar Remote Sensing in Atmospheric and Earth Sciences, Proc. 21st ILRC, Valcartier, Quebec Canada*, pages 535–545, 2002.

[22] David Casbeer. Real-time estimation of atmospheric turbulence severity from in-situ aircraft measurements. *Journal of Aircraft*, 37(6):351–360, 1995.

[23] Valeri Matvev, Uri Dayan, Iran Tass, and Mordechai Peleg. Atmospheric sulfur flux rates to and from israel. *Science of The Total Environment*, 291(13):143 – 154, 2002.

[24] P. P. Neumann, S. Asadi, A. J. Lilienthal, M. Bartholmai, and J. H. Schiller. Autonomous gas-sensitive microdrone: Wind vector estimation and gas distribution mapping. *IEEE Robotics Automation Magazine*, 19(1):50–61, March 2012.

[25] Timothy Bonin, Phillip Chilson, Brett Zielke, and Evgeni Fedorovich. Observations of the early evening boundary-layer transition using a small unmanned aerial system. *Boundary-Layer Meteorology*, 146(1):119–132, 2013.

[26] A. C. van den Kroonenberg, S. Martin, F. Beyrich, and J. Bange. Spatially-averaged temperature structure parameter over a heterogeneous surface measured by an unmanned aerial vehicle. *Boundary-Layer Meteorology*, 142(1):55–77, 2012.

[27] A.C. van den Kroonenberg, T. Spieß, M. Buschmann, T. Martin, P.S. Anderson, F. Beyrich, and J. Bange. Boundary layer measurements with the autonomous mini-UAV M^2AV. In *Proceedings of DACH2007*, Hamburg, Germany, 2007.

[28] Jack W. Langelaan, Nicholas Alley, and James Neidhoefer. Wind field estimation for small unmanned aerial vehicles. *Journal of Guidance, Control, and Dynamics*, 34(4):1016–1030, 2011.

[29] S. Metzger, W. Junkermann, K. Butterbach-Bahl, H. P. Schmid, and T. Foken. Measuring the 3-d wind vector with a weight-shift microlight aircraft. *Atmospheric Measurement Techniques*, 4(7):1421–1444, 2011.

[30] A. van den Kroonenberg, T. Martin, M. Buschmann, J. Bange, and P. Vörsmann. Measuring the wind vector using the autonomous mini aerial vehicle M^2AV. *J. Atmos. Oceanic Technol.*, 25:1969–1982, 2008.

[31] Stephanie Mayer, Gautier Hattenberger, Pascal Brisset, Marius O. Jonassen, and Joachim Reuder. A no-flow-sensor wind estimation algorithm for unmanned aerial systems. *International Journal of Micro Air Vehicles*, 4(1):15–29, 2012.

[32] R. M. Thomas, K. Lehmann, H. Nguyen, D. L. Jackson, D. Wolfe, and V. Ramanathan. Measurement of turbulent water vapor fluxes using a lightweight unmanned aerial vehicle system. *Atmospheric Measurement Techniques*, 5(1):243–257, 2012.

[33] D. N. Axford. On the accuracy of wind measurements using an inertial platform in an aircraft, and an example of a measurement of the vertical mesostructure of the atmosphere. *Journal of Applied Meteorology*, 7(4):645–666, 1968.

[34] DH Lenschow. *The measurement of air velocity and temperature using the NCAR Buffalo aircraft measuring system*. National Center for Atmospheric Research, 1972.

[35] C. Broxmeyer and C. I. Leondes. Inertial Navigation Systems. *Journal of Applied Mechanics*, 31:735, 1964.

[36] K.S. Wittmer, W.J. Devenport, and J.S. Zsoldos. A four-sensor hot-wire probe system for three-component velocity measurement. *Exp. Fluids*, 24:416–423, 1998.

[37] K. Döbbeling, B. Lenze, and W. Leuckel. Computer-aided calibration and measurements with quadruple hotwire probes. *Exp. Fluids*, 8:257–262, 1990.

[38] Bernard Etkin. *Dynamics of atmospheric flight*. Courier Corporation, 2000.

[39] James A Leis, Jeffery M Masters, and Aircraft Operations Center. Wind measurement from aircraft. 1993.

[40] Warren F Phillips. *Mechanics of flight*. John Wiley & Sons, 2004.

[41] Allen L Treaster and Adam M Yocum. The calibration and application of five-hole probes. Technical report, DTIC Document, 1978.

[42] N. Wildmann, S. Ravi, and J. Bange. Towards higher accuracy and better frequency response with standard multi-hole probes in turbulence measurement with remotely piloted aircraft (rpa). *Atmospheric Measurement Techniques*, 7(4):1027–1041, 2014.

[43] D Bohn and H Simon. Mehrparametrige approximation der eichräume und eichflächen von unterschall-bzw. überschall-5-loch-sonden. *tm-Technisches Messen*, 468(JG):81–89, 1975.

Vita

Brandon Michael Witte was born in Villa Hills, Kentucky, the son of Richard and Carolyn Witte. After graduating from Covington Catholic High School in Park Hills, Kentucky, he entered the University of Kentucky in Lexington, Kentucky, to study mechanical engineering. He received a bachelor's of science degree in mechanical engineering with summa cum laude honors in May of 2013. During the following years, he pursued a master's of science degree in mechanical engineering at the University of Kentucky with a focus in fluid dynamics.